Investigating Cellular Mechanisms in the Pathogenesis of the Renal Fanconi Syndrome

Dissertation

zur

Erlangung der naturwissenschaftlichen Doktorwürde
(Dr. sc. nat.)

vorgelegt der

Mathematisch-naturwissenschaftlichen Fakultät
der
Universität Zürich

von
Esther Maria Gottwald

aus
Deutschland

Promotionskommission

Prof. Dr. Andrew Hall (Vorsitz)

Prof. Dr. Johannes Loffing

Dr. Sophie De Seigneux

Zürich, 2018

Für Papa

INDEX

ABBREVIATIONS

AKI	Acute kidney injury
Asc	Ascorbate
ATP	Adenosine triphosphate
CL	Cardiolipin
CyC	Cytochrome c
$\Delta\Psi_m$	Mitochondrial membrane potential
DFA	Deferoxamine
DFX	Deferasirox
DFP	Deferiprone
DNA	Deoxyribonucleic acid
DTPP	Dodecyltriphenylphosphonium
FAD	Flavin adenine dinucleotide
FBS	Fetal bovine serum
FDA	Food and Drug Administration
GFP	Green fluorescent protein
ICU	Intensive care unit
ISMP	Institute for safe medical practices
µM	µmol/l
mPTP	Mitochondrial permeability transition pore
NADH	Nicotinamide adenine dinucleotide
nm	Nanometer
NSAID	Non-steroidal anti-inflammatory drug
OK	Opossum kidney
PBS	Phosphate buffered solution
PT	Proximal tubule
RIFLE	Risk, Injury, Loss, Failure, End-stage
ROS	Reactive oxygen species
STED	Stimulated emission depletion
STORM	Stochastic optical resolution microscopy
TMRM	Tetramethylrhodamine methyl ester
TMPD	Tetramethylphenylenediamine

1 INTRODUCTION

1.1 The kidney as a critical target organ of drug toxicity

The kidney plays a central role in ensuring homeostasis in the body. Besides ensuring excretion of toxins together with the liver and the gastrointestinal tract, the kidney regulates blood pressure, acid-base balance, electrolyte concentrations and the volume of extracellular fluids. These tasks are achieved by glomerular filtration, tubular reabsorption and tubular secretion[1].

Impairment of renal function can therefore lead to an increased patient morbidity and mortality[2, 3]. Acute kidney injury (AKI, formerly defined as acute renal failure) is a syndrome of abrupt loss in kidney function leading to an accumulation of products of nitrogen metabolism and/or decreased urine output, which is not always present[1]. Large variations of the incidence of AKI from 1 % to 31 % and the associated mortality (19 % - 83 %) have been reported, due to a lack of a consensus in the definition of AKI[4-6]. Therefore, in 2004 the Acute Dialysis Quality Initiative formulated the Risk, Injury, Failure, Loss and End-stage kidney (RIFLE) classification[7] (Table 1). It defines three stages of injury (risk, injury and failure) and two outcomes (loss and end-stage kidney disease).

Table 1: RIFLE (Risk, Injury, Failure, Loss, End-stage) classification for AKI[7, 8]

Class	**Glomerular filtration rate (GFR) criteria**	**Urine output criteria**
Risk	Serum creatinine x 1.5 >25 % GFR decrease	< 0.5 ml/kg/hour x 6 hours
Injury	Serum creatinine x 2 >50 % GFR decrease	< 0.5 ml/kg/hour x 12 hours
Failure	Serum creatinine x 3 or ≥ 4mg/dl with an acute rise < 0.5 mg/dl >75% GFR decrease	< 0.3 ml/kg/hour x 24 hours or anuria x 12 hours
Loss	Loss of kidney function > 4 weeks	
End-stage kidney disease	End-stage kidney disease > 3 months	

Using unified criteria for staging kidney injury led to less variable numbers confirming that AKI is a global public health concern affecting around 13.3 million patients per year[9]. Among all hospitalized patients AKI has an incidence varying between 1-9 % depending on the population[10]. Especially critically ill patients (ICU - intensive care unit - patients) have a high incidence of 67 % in developing kidney injury[8].

Twenty percent of all kidney injuries are induced by drugs while hospital-acquired infections, sepsis, administration of radiocontrast and complex surgery are other factors for developing AKI[11].

The kidney is highly susceptible to injury due to several unique physiological features of this organ. Although only constituting 1 -2 % of the total body mass, the kidney receives 1200 ml/ min of blood (20 -25 % of cardiac output)[12]. Taken together with the filtration of 180 l per day in the glomeruli, the kidney has a higher exposure to toxicants compared to other tissues in the body. Especially cells in the proximal tubule (PT) have a very high exposure due to the large surface area, formed by microvilli, and the enormous capability of reabsorption. Of the 180 l of primary filtrate, approximately 65 % is reabsorbed in the PT[13]. The large number of transporters expressed at the apical and basolateral side in the PT cells and the ability to concentrate solutes enhances the chance of drug accumulation and consequently cytotoxicity[14]. Furthermore, biotransforming enzymes expressed in the kidney, such as P459 monooxygenases, flavin containing monooxygenases and glutathione transferases, can convert drugs into toxic metabolites. The structure and the physiology of the PT will be described in the following chapter, since the PT is primarily the target in drug induced nephrotoxicity.

1.2 The renal proximal tubule

Each of the two human kidneys contains 900000 to 1 million nephrons, the functional unit of the kidney[15]. Each nephron consists of the glomerulus, the PT, loop of Henle, distal tubule and the collecting duct (which is shared with other nephrons)[16]. The PT extends from the urinary pole of the glomerulus to the descending thin loop of Henle (Figure 1).

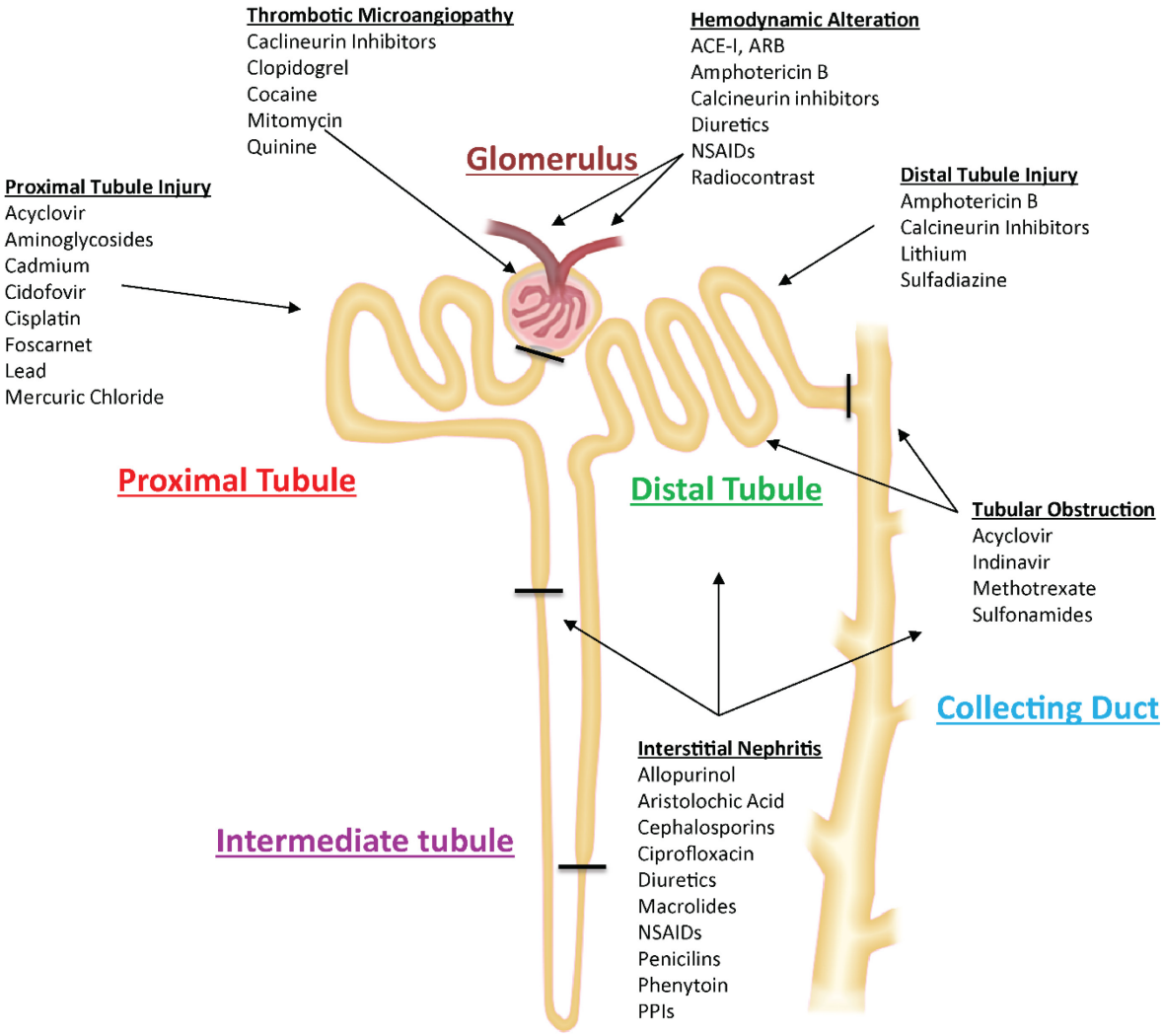

Figure 1: Structure of the nephron and examples for drug induced nephrotoxicity. (modified after Vaidya et al[16])

Anatomically the PT can be divided into pars convoluta, which is located in the cortical labyrinth and pars recta, which descends through the medullary ray into the outer stripe of the outer zone of the medulla[17]. A different classification into three parts can be made when PT segments are characterized by their ultrastructure as first described by Suzuki[18], using light microscopy, and Sjostrand[19], using additionally fluorescence microscopy. The first part (S1) ranges from the glomerulus and transitions slowly into the second (S2) segment, which ranges from the end of the convoluted part until the beginning of pars recta. The change into the third segment (S3) occurs abruptly. Epithelial cells in S1 are slightly taller than cells in S2, due to their extensive apical brush border. Furthermore, S1 cells interdigitate more extensively and have a very high number of mitochondria that are arranged in a palisade-

shaped manner and are closely enwrapped by the basolateral membrane, the location of the sodium potassium ATPase. This is indicative of the high energy demand in these highly active transporting cells. Cells in S3 have a cuboidal shape, interdigitate little and have fewer, more randomly distributed mitochondria[20] (Figure 2).

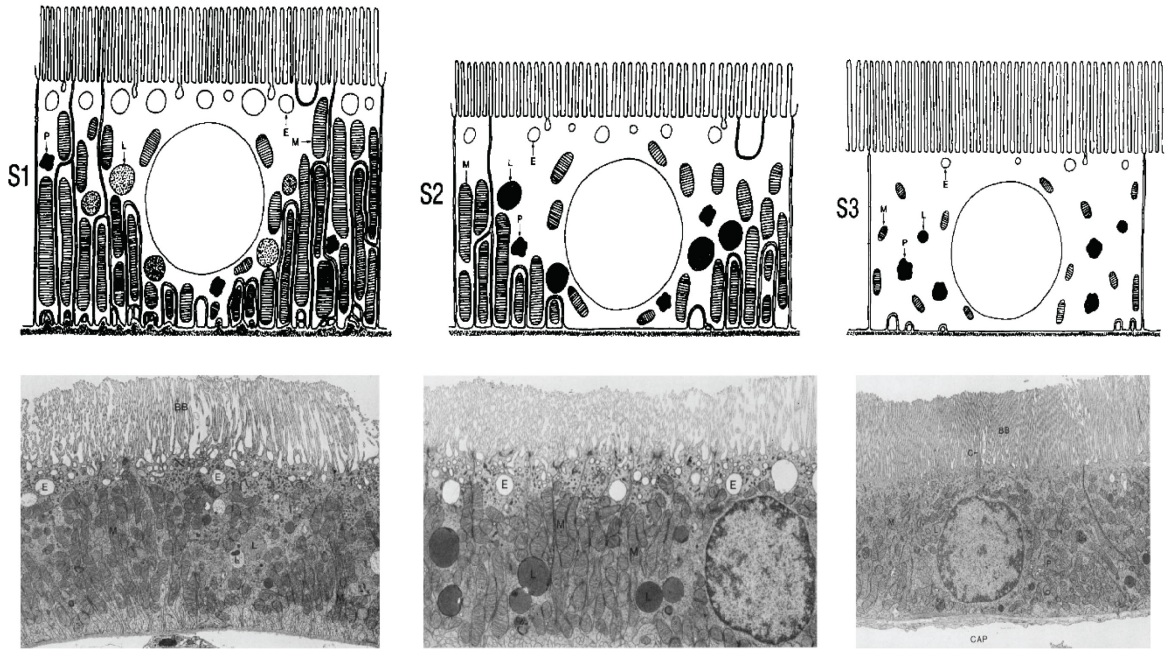

Figure 2: Classification of the PT into three segments using ultrastructure. The diagram illustrates the differences of the three PT segments S1, S2 and S3 in terms of cell shape, distribution and number of mitochondria (M), lysosomes (L), endocytic vacuoles (E) and peroxisomes (P). Below are the according electron micrographs from the rat kidney. Taken from Maunsbach, Christensen chapter 2 in renal physiology [20].

The morphological features of the epithelial cells in the PT – energy demanding cells with a very well-developed transport machinery - already point towards the most important physiological function: reabsorption and secretion. Along the nephron the PT is responsible for reclaiming 65 % of the primary urine, whereas the distal tubule accounts for 30 % and the collecting duct for only 4 %[13]. The driving force in proximal tubular reabsorption is the sodium flux through the cell[21, 22]. In the 1970's, using in vivo micropuncture, Gyory and Kinne showed that blocking of the sodium potassium ATPase, which is located on the basolateral side of the PT cell[23, 24], with ouabain abolished reabsorption of sodium and any fluid in PTs[25]. The sodium potassium ATPase constantly removes sodium from the epithelial cell, which generates a concentration gradient favouring sodium entry from the primary urine into the cell. Along with water that is moving passively through the cell due to the sodium gradient (via water channels called aquaporins), other transporters facilitate the apical uptake of molecules. All of the filtered glucose and amino acids are reabsorbed in the PT by secondary active transport through cotransporters driven by the sodium flux from urinary to interstitial side. Responsible for the uptake of glucose and sodium into the PT cell is the

high-capacity, low affinity sodium and glucose cotransporter SGLT2, which is almost exclusively found in apical membranes of PTs (S1,S2 segments)[26-28].

Similarly, 80 % of filtered phosphate is reabsorbed apically by the PT expressed sodium driven cotransporters NaPi-IIa and NaPi-IIc[29, 30]. The expression of NaPi-IIa gradually decreases over the PT, whereas NaPi-IIc was not identified in S3 segments[29, 31].

The PT also plays an important role in the reuptake of bicarbonate, as 80% of the filtered bicarbonate is reabsorbed by the PT. The apical located sodium proton antiporter leads to a luminal secretion of one proton, which, catalysed by carbonic anhydrase IV, reacts with bicarbonate to CO_2 and water. CO_2 can diffuse into the PT cell where it is metabolized by carbonic anhydrase II to bicarbonate and finally exported on the basolateral side via the sodium bicarbonate cotransporter kNBC1.

65 % of filtered potassium is reabsorbed passively via solvent drag or diffusion. Chloride and calcium are also transported paracellularly. Water can also be reabsorbed paracellularly and transcellularly via water channels (aquaporins, AQP-1).

Upon damage of PT cells (renal Fanconi syndrome, see detailed explanation in chapter 1.4), the important role of the uptake of certain molecules becomes clear, as it is characterized by a urinary loss of glucose, amino acids, phosphate and bicarbonate (Figure 3). No other segment in the nephron can compensate for the uptake of these molecules.

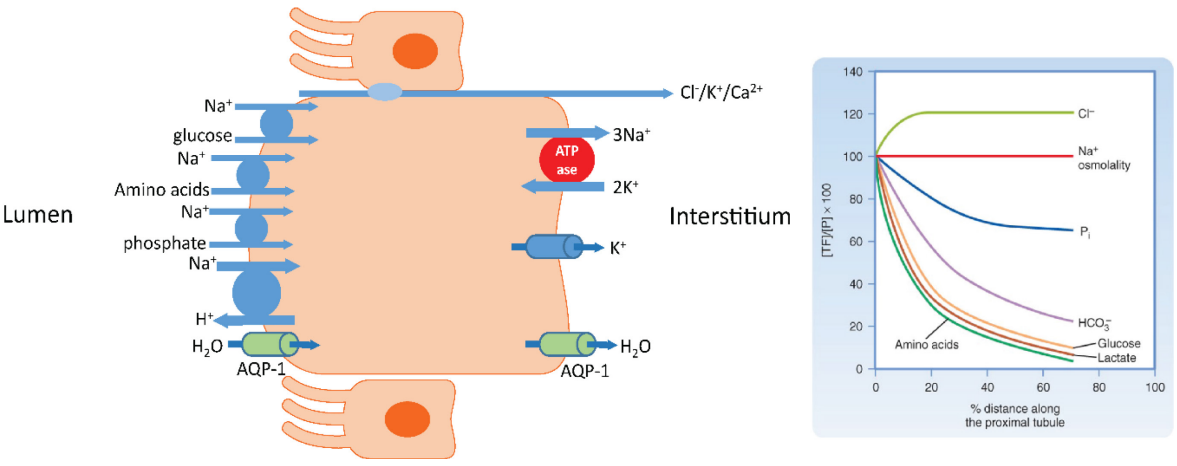

Figure 3: Reuptake of glucose, amino acids, phosphate and bicarbonate is mainly performed by the PT (diagram). The uptake of the solutes is coupled to the sodium gradient across the cell that is maintained by the sodium potassium ATPase (right: schematic display of important transporters)[13].

Another very important process in the PT is the reuptake of filtered low molecular weight proteins (LMWP), like insulin, parathyroid hormone and retinol binding protein[32]. The reuptake ensures that these proteins are not lost in the urine and that distal parts of the nephron are not exposed to bioactive proteins. The uptake of LMWPs is mostly facilitated by the low-affinity, high-capacity uptake system of the two receptors megalin and cubilin[33, 34]. Megalin, identified in 1982, is a large 600 kDa glycosylated receptor[35] and belongs to the low-density lipoprotein receptor family[35, 36]. Megalin is expressed in the apical membrane of the PT and was also found to be present in endocytic vesicles[37]. Extrarenal absorptive epithelia like the choroid plexus, lung alveoli, ciliary body, retinal epithelium of the eye, gall bladder, placenta, parathyroid glands and thyroid gland also express megalin[38]. Cubilin, a 460 kDa glycosylated extracellular protein, is believed to be responsible for ligand binding[39]. Cubilin is thought to interact with membrane proteins for membrane localization and endocytosis[40]. In the PT cubilin supposedly interacts with megalin (both share a number of ligands) forming a multireceptor complex driving the internalization of the bound ligands and the complex itself (receptor mediated endocytosis)[41]. The endosomes formed are then acidified to promote dissociation of the ligand and the receptors can be recycled to the luminal membrane[42, 43].

Along with the liver, the kidney is heavily involved in the elimination of drugs, with around 32 % of drugs currently used in the US showing renal elimination greater than 25 %[44]. Elimination can occur via glomerular filtration or tubular secretion, or a combination of both. For the transcellular transport of drugs from the blood through the PT into the urine, drugs need to enter the PT cell via the basolateral membrane and exit via the apical side. In many cases this process does not happen passively, but involves transporter proteins, that can facilitate a transport against concentration gradients. The transporters being suspected to be involved in drug transport can be separated into cationic transporters (Table 2), anionic transporters (Table 3), transporters with less or unknown specificity in substrate charge (Table 4) and ABC efflux transporters (Table 5)[45]. It is important to consider that the expression site of these transporters is often not limited to a single location in the body[46].

Table 2: List of cationic transporters expressed in the kidney[45]

Transporter	Expression	Substrates
SLC22A1 OCT1	Basolateral (influx)	prostaglandin E2, choline, morphine, tetraethyl ammonium, metformin, acyclovir, lamivudine
SLC22A2 OCT2	Basolateral (influx)	creatinine, dopamine, histamine, prostaglandin E2, tetraethylammonium, pancuronium, MPP, lamivudine
SLC22A3 OCT3	Basolateral (influx)	5-HT, noradrenaline, dopamine, quinidine, tetraethyl ammonium, MPP
SLC47A1 MATE1	Apical (efflux)	Creatinine, thiamine, cimetidine, quinidine, paraquat, cephradine, cephalexin
SLC47A2 MATE2K	Apical (efflux)	Creatinine, thiamine, cimetidine, MPP, metformin, aciclovir

Table 3: List of anionic transporters expressed in the kidney[45]

Transporter	Expression	Substrates
SLC22A6 OAT1	Basolateral (influx)	Aminohippuric acid, estrone sulfate, raltegravir, tenofovir, zidovudine
SLC22A7 OAT2	Basolateral (influx)	Aminohippuric acid, prostaglandine E2, estrone sulfate, paclitaxel, 5-fluorouracil, allopurinol, zidovudine
SLC22A8 OAT3	Basolateral (influx)	Aminohippuric acid, estrone sulfate, raltegravir, tenofovir, zidovudine
SLC22A11 OAT4	Apical (bidirectional)	Dehydroepiandrosterone, estrone sulfate, uric acid, zidovudine
SLC22A12 URAT1	Apical (bidirectional)	Uric acid, orotic acid
SLCO4C1 OATP4C1	Basolateral (influx)	Steroid conjugates, thyroid hormones, digoxin, ouabain, penicillin

Table 4: List of transporters with no specificity for substrate charge expressed in the kidney[45]

Transporter	**Expression**	**Substrates**
SLC15A1 PEPT1	Apical (influx)	Oligopeptides, cyclacillin, valacyclovir, cefadroxil
SLC15A2 PEPT2	Apical (influx)	Oligopeptides, beta-lactam antibiotics, fosinopril
SLC28A1 CNT1	Apical (efflux)	Nucleosides, ribavirin, gemcitabine, zidovudine, zalcitabine
SLC28A2 CNT2	Apical (efflux)	Nucleosides, didanosine, cytidine
SLC28A3 CNT3	Apical (efflux)	Nucleosides, zidovudine, zalcitabine, didanosine
SLC29A1 ENT1	Basolateral (bidirectional)	Nucleosides, ribavirine, 2',3'-Dideoxyinosine
SLC29A2 ENT2	Basolateral (bidirectional)	Nucleosides, 2',3'-Dideoxyinosine

Table 5: List of ABC efflux transporters expressed in the kidney[45]

Transporter	**Expression**	**Substrates**
ABCB1 P-gp	Apical (efflux)	Steroids, lipids, bilirubin, bile acids, digoxin, doxorubicin, maraviroc, HIV protease inhibitors
ABCC1 MRP1	Basolateral (efflux)	Prostaglandins, folic acid, bilirubin, anticancer drugs, HIV protease inhibitors
ABCC2 MRP2	Apical (efflux)	Bilirubin, estradiol, glucuronide, estrone sulfate, methotrexate, etoposide, valsartan, HIV protease inhibitors
ABCC3 MRP3	Basolateral (efflux)	Bile salts, estradiol glucuronide, anticancer drugs
ABCC4 MRP4	Apical (efflux)	Taurocholic acid, cAMP, cGMP, urate, prostaglandins, methotrexate, furosemide
ABCC6 MRP6	Basolateral (efflux)	Anticancer drugs
ABCC10 MRP7	Unknown	Estradiol glucuronide, paclitaxel, tariquidar, tenofovir, nevirapine
ABCG2 BCRP	Apical (efflux)	Estrone sulfate, porphyrins, anticancer drugs, conjugated organic anions

1.3 Mitochondria – the indispensable energy supplier in the proximal tubule

The kidney is second only to the heart in mitochondrial number and oxygen consumption.[47] The main function of the PT, the transport of solutes, is a very energy demanding process, which makes the PT cells highly dependent on mitochondria, the energy factory of the cell. Mitochondria in PT cells are numerous and are enwrapped in basolateral infolds, located in close proximity to the sodium potassium ATPase, the main energy consumer.

Mitochondria are intracellular organs present in every cell of the human body, except erythrocytes, and are of endosymbiotic origin, which is visible by the existence of two membranes, the outer and the inner membrane. The outer membrane is a simple phospholipid bilayer, which has a high permeability due to existing porins, facilitating easy exchange of, for example, nutrients or ADP/ATP. The infolded inner mitochondrial membrane (cristae), which in addition to phosphatidylcholine also contains cardiolipin[48], incorporates complex structures and is the location of the respiratory chain complexes and transport proteins (for example transporter of the inner membrane TIM[49]). The cristae allow an efficient assembly of the different complexes and can help to locally accumulate molecules from the mitochondrial matrix[50].
Traditional theory claims that the primitive obligate aerobe structure - the precursor of the mitochondrion possibly similar in physiology to the modern *Rickettsia* species - was acquired by an anaerobic nucleus-bearing cell via phagocytosis[51]. The mitochondria not only provided energy for the host, but also served as detoxifier as they removed oxygen from the cell. An alternate theory claims that the host was an archaebacterium that engulfed the ancestral mitochondrion, a facultative anaerobe, similar to the still existing Rhodobacterials[52, 53]. Here the benefit for the archaebacterial host originated in the mitochondrion providing electrons and H_2 as a source of energy[54]. How the facultative anaerobe was taken up into the archaebacterium remains unclear.

1.3.1 Generating energy in mitochondria

ATP, the chemical energy equivalent in the cell, is generated from ADP and HPO_4^- by the mitochondrion via oxidative phosphorylation. This reaction is catalyzed by complex V, the ATP synthase, which is fuelled by the proton gradient across the inner mitochondrial membrane. The proton gradient is built up by complex I, III and IV during the electron transport chain, with the final reaction of oxygen to water. For the generation of the redox-equivalents NADH and $FADH_2$, fuel molecules, such as glucose, fatty acids and amino acids, are broken down to acetyl CoA. Acetyl CoA enters the citric acid cycle, where during several steps NAD^+ and FAD^{2+} are reduced to NADH and $FADH_2$ and oxaloacetate is

generated, which serves as an acceptor for acetyl CoA. NADH and $FADH_2$ are oxidized by complex I and II, respectively. The electrons donated by the redox-equivalents are then shuttled from complex I or II by ubiquinone (coenzyme Q10) to complex III. From there electrons are passed on to cytochrome c, which then donates the electrons to complex IV (cytochrome c oxidase). The electrons are then passed onto oxygen reducing it to water (together with protons). During the electron transport complexes I, III and IV pump protons from the matrix into the intermembrane space, generating an electrochemical proton gradient; also called proton motive force. This gradient explains why the mitochondrial matrix is negatively charged in comparison to the cytosol, the so called mitochondrial membrane potential ($\Delta\Psi_m$ approximately 150 mV)[55]. The ATP synthase uses the movement of protons along the electrochemical gradient to generate ATP from ADP and HPO_4^- (Figure 4). The energy that was generated from breaking down bonds of carbon and hydrogen based organic fuels was converted into energy stored in ATP via chemiosmotic coupling. Energy can be released by the reaction of ATP to ADP, as for example performed by the sodium potassium ATPase[56].

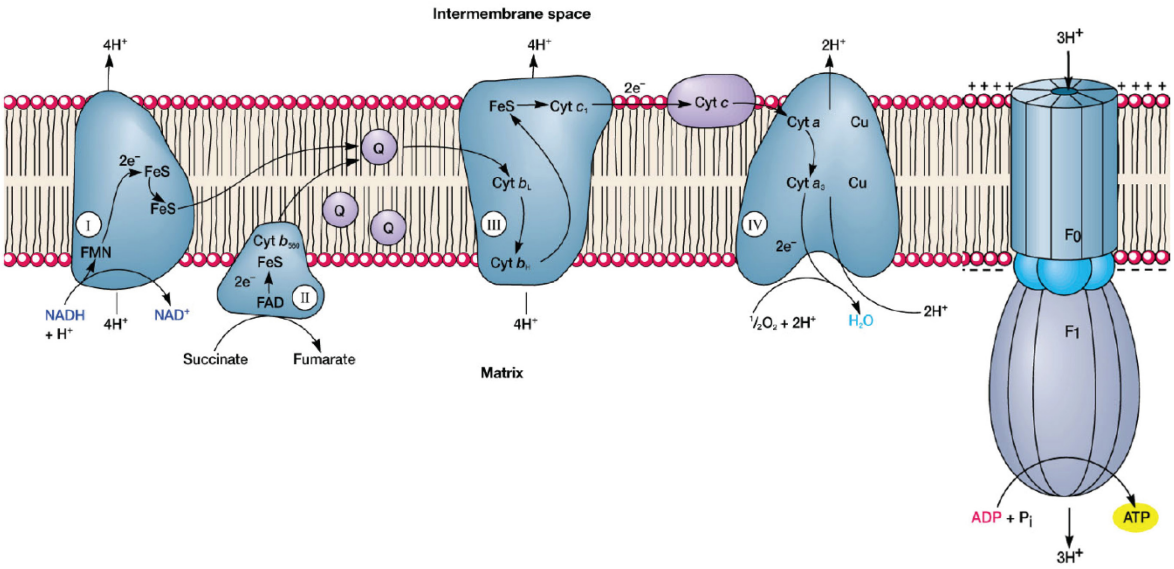

Figure 4: Scheme of oxidative phosphorylation. NADH and $FADH_2$ are oxidized by complex I and II, respectively. The donated electrons are then shuttled by ubiquinone (Q) to complex III. From there electrons are transferred to cytochrome c, where the electrons are passed on to complex IV and finally to oxygen reducing it to water (together with protons). Complexes I, III and IV are pumping protons into the intermembrane space, generating an electrochemical proton gradient, which fuels the generation of ATP by complex V (ATP synthase)[57].

1.3.2 The role of iron in mitochondria

Apart from the function of generating energy in the form of ATP, mitochondria play a central role in the metabolism of trace elements, especially iron. Iron is involved in many cellular processes such as energy metabolism, respiration and DNA synthesis. Iron has unpaired electrons which gives it the ability to donate or accept electrons. Therefore, iron is often incorporated as a prosthetic group in structural proteins and enzymes[58]. Along with the reactivity of iron the danger of enabling reactions that are harmful to the cell arises. As an example the generation of reactive oxygen species (ROS) can induce cell death[59]. Hence, a sophisticated mechanism has been developed in the cell to minimize the risk of toxicity, while maintaining metabolic reactions[60]. The gatekeeper for iron regulation and metabolism is the mitochondrion.

Mitochondria utilize and accumulate iron, leading to a mitochondrial iron concentration twice as high as in the cytosol[61]. Iron as cofactor is part of heme-containing proteins, iron-sulfur-cluster-containing proteins and iron ion containing proteins. Important heme containing proteins include succinate dehydrogenase (complex II), cytochrome bc1 (complex III), cytochrome c and cytochrome c oxidase (complex IV), which are all involved in the electron transport chain. Also involved in the electron transport chain are the iron-sulfur containing proteins NADH:ubiquinone oxidoreductase (complex I), subunits of succinate dehydrogenase (complex II), Rieske iron-sulfur protein (complex III) and electron-transfer flavoproteins[62]. Involved in other processes are the iron-sulfur-cluster-containing proteins aconitase (enzyme in the citric acid cycle), lipoic acid synthase (lipoic acid is a mitochondrial anti-oxidant[63]), biotin synthase (biotin is a coenzyme involved in the synthesis of fatty acids, isoleucine, valine and in gluconeogenesis[64]) and radical S-adenosylmethionine (SAM) enzymes (generation of radicals to functionalize non-activated C-H bonds[65]). Diiron monooxygenases and dioxygenases contain iron-ion cofactors. Members of the AlkB family of Fe(II)-and 2-oxyglutarate dioxygenases ALKBH1 and ALKBH7 are involved in mitochondrial-tRNA modification and regulation of necrosis, respectively[66, 67]. The large number of enzymes requiring iron as a cofactor demonstrates the importance of iron for mitochondria.

Disturbance of the iron balance in mitochondria can negatively affect mitochondrial function and health. Deficiency in iron can decrease the activity of iron containing enzymes in mitochondria leading to an impaired respiration together with decreased levels of cytochrome and gluconeogenesis[68, 69]. Mitochondrial morphology can also be altered, presented by increased mitochondrial size, rounding up of the mitochondria and a loss of cristae[70, 71]. These changes can eventually also induce damage such as fragmentation of mitochondrial DNA[72].

Similar to iron deficiency, iron overload can damage mitochondria. The elevated levels of iron can lead to increased levels of ROS, which can damage for example lipids causing a change of membrane fluidity and permeability[73]. Additionally, iron overload also induces a reduction of respiration, decreased expression of respiratory chain enzymes and damage of mitochondrial DNA[74]. High levels of cytosolic iron can affect the uptake of manganese, resulting in decreased activity of the mitochondrial manganese-dependent superoxide dismutase, an enzyme protecting against radicals generated from respiration[75]. These effects finally induce cell death, including iron-dependent ferroptosis[76].

1.3.3 Responding to stress in mitochondria: the mitochondrial permeability transition pore (mPTP)

In response to stress mitochondria are thought to open the mitochondrial permeability transition pore (mPTP). The mPTP is an inner membrane structure that forms a nonselective channel[77]. This voltage-gated channel, controlled by a number of proteins, typically opens in response to ROS and calcium overloading[78]. The mPTP exhibits different permeabilities due to various opening times ranging from periods of milliseconds to seconds[79]. A full opening of the mPTP induces the release of matrix metabolites, like NAD^+, glutathione and calcium, which results in an immediate loss of mitochondrial membrane potential, inhibition of oxidative phosphorylation, swelling of mitochondria and eventually rupture of the outer membrane and release of intermembrane space proteins[78]. This burst of metabolites into the cytosol damages proteins, nuclear DNA, transporters, ion channels and membrane phospholipids[80], which induces cell death if the mPTP remains open[81-83].
The composition of the mPTP remains unclear, as knockout models of the suggested proteins forming the pore (in any combination) showed that none of cyclophilin D (CypD), the adenine nucleotide translocator (ANT), the outer membrane anion channel (VDAC), or the phosphate translocator (PiC) are essential[78]. Recently, either the subunit c of ATP synthase or a dimer of ATP synthase is believed to form the core of the mPTP. Definite proof of the composition and the existence of the mPTP remains a target of investigation[79, 82]. Therefore, explaining mitochondrial swelling simply by suggesting mPTP opening has to be done cautiously.

1.4 Renal Fanconi Syndrome

First observations of the specific proximal tubular dysfunction were made in 1903 by Abderhalden, who described a deposition of cystine crystals in liver and spleen of a 21-month-old infant and named the disorder familial cysteine diathesis[84]. Similar cases in children with progressive wasting, rickets, dwarfism and renal disease where described 21 years later by Lignac[85]. After describing in 1930 a child not only presenting with rickets and stunted growth, but also glucosuria and albuminuria, Fanconi recognized in 1936 the similarity between his case and the descriptions of deToni in 1933 and Debré in 1934 and suggested the term “nephrotic-glycosuric dwarfism with hypophosphatemic rickets” for the syndrome[86-89]. The name which is referred to as Lignac-de Toni-Debre-Fanconi syndrome, was reduced to Fanconi syndrome in 1943 by McCune[90].

Renal Fanconi syndrome is the result of a dysfunction of the PT resulting in an increased urinary excretion of substances that are exclusively or predominantly reabsorbed in the PT, namely glucose, amino acids, phosphate and bicarbonate[91]. Alongside with water a variety of solutes including sodium, potassium, calcium, magnesium, carnitine, lysozyme, enzymes, peptide hormones and immunoglobulin light chains, can also be lost during the occurrence of Fanconi syndrome. Due to the loss of phosphate a metabolic bone disease (bone demineralization) can develop as a secondary complication. Children with Fanconi syndrome fail to grow and present with a clinical picture of rickets, such as bowing deformities of the legs, frontal bossing, beading of the ribs and metaphyseal widening at the wrists, knees or ankles. Adults with acquired Fanconi syndrome suffer from osteomalacia, which is characterized by bone pain and spontaneous fractures[92].
The different onset times for Fanconi syndrome already make it clear that the origin of the syndrome is variable. The early onset is a sign of a hereditary source, whereas a late onset hints to an acquired Fanconi syndrome induced by nephrotoxic drugs or chemicals.
Genetic forms of Fanconi syndrome can be categorized as (i) accumulation of a toxic metabolite, (ii) disruption of cellular energy supply or (iii) disruption of intracellular transport[93]. The deposition of cystine as described by Abderhalden in 1903 and Fanconi in 1936 is one example for the accumulation of a toxic metabolite; in these cases patients suffered from cystinosis where a mutation of the CTNS gene coding for the lysosomal cysteine transporter cystinosin causes the accumulation of cystine in the lysosomes[94]. Other examples of genetic diseases that involve accumulation of toxic metabolites are tyrosinaemia (disturbed breakdown of tyrosine), galactosaemia (disturbed breakdown of galactose 1-phosphate), Fanconi-Bickel (mutation of the glucose transporter 2 leading to accumulation of glycogen in liver and kidney), hereditary fructose intolerance (deficiency in fructose 1-phosphate aldolase causes increased amounts of fructose 1-phosphate after

fructose ingestion) and Wilson's disease (copper accumulation)[92]. Mitochondrial cytopathies such as the Pearson and MELAS (mitochondrial encephalomyopathy with lactic acidosis and stroke-like episodes) syndromes, induce the Fanconi phenotype by disrupting energy supply. Another genetic form of Fanconi syndrome causing mitochondrial dysfunction, was described recently. A missense mutation in the third codon of the peroxisomal protein EHHADH targets the EHHADH to mitochondria, where the protein is incorporated into mitochondrial trifunctional protein causing disturbance of β-oxidation of long chain fatty acids. Additionally, mutated EHHADH limits the activity of respiratory complex I, resulting in decreased oxidative phosphorylation, mitochondrial membrane potential maintenance and ATP generation. This leads to a diminished function of the sodium potassium ATPase restricting the cellular uptake and extrusion[95].

Interference with the uptake machinery in the PT occurs, for example, with the oculocerebrorenal (Lowe) syndrome (mutation in the OCRL1 gene leads to disturbed interaction of the protein with clathrin and therefore to dysregulated protein trafficking between endosomes and the Golgi network)[96], or in Dent's disease 1 where a mutation in the gene encoding for the chloride transporter ClC5 leads to an insufficient acidification of endosomes, and therefore impaired receptor recycling for endocytosis[97]. In addition to these systemic disorders isolated forms of Fanconi syndrome (Fanconi renotubular syndrome 1-3) have been reported and are still under investigation[93].

In contrast to hereditary forms of Fanconi syndrome, acquired Fanconi syndrome can occur at any point in life. Apart from the biggest risk factor of drug induced Fanconi syndrome, environmental toxins, abnormal proteins and immunological disorders contribute to the number of acquired Fanconi syndromes. Among environmental toxins heavy metals are one of the main causes of the disease. Contamination of soil and rice with cadmium after the second world war, for example, led to an increased number of cases of itai-itai or "ouch-ouch" disease, which is characterized by a loss of PT function and osteomalacia[98]. Cadmium and uranium are both more toxic than lead and mercury, but heavy metal induced nephrotoxicity is due to an accumulation of the metal that then interferes with the transport processes in the PT. Exposure to platinum usually only occurs during chemotherapeutic treatment of carcinoma with cisplatin, which is a known cause for Fanconi syndrome.

Accumulation of abnormal plasma proteins can occur with multiple myeloma, amyloidosis, light chain nephropathy and benign monoclonal gammopathy[92]. Filtered immunoglobulin light chains are reabsorbed in the PT via endocytosis and, in excess amounts, are toxic to the PT.

By far the most frequent cause for acquired Fanconi syndrome is drug toxicity. This is not only a huge burden for the patients themselves, but also limits the efficacy and usage of

otherwise effective therapies. The list of drugs and chemicals inducing Fanconi syndrome is huge and unfortunately continues to grow (Table 6), with the most common drugs being anti-cancer agents, antivirals and aminoglycoside antibiotics[99]. The PT cell takes up many of the drugs circulating in the bloodstream by various transporters, such as organic anion and cation transporters and p-glycoprotein[100]. This leads to elevated concentrations of the drugs in the PT cells compared to all other cells in the human body – with the exception of hepatocytes. The mechanisms of how the accumulation induces PT dysfunction are not well studied and can differ between drugs although resulting in the same clinical phenotype.

Table 6: List of drugs inducing Fanconi syndrome[91]

Class	Drugs	Indication
Alkylating agents	Ifosfamide	Cancer
Aminogycoside Antibiotics	Gentamicin, Amikacin	Gram-negative bacterial infection
Anti-epileptics	Sodium valporate	Seizures, bipolar disorders
Anti-protozoals	Suramin	Trypanosomiasis
Dicarboxylic acids	Fumaric acid	Psoriasis
Iron chelators	Deferasirox	Iron overload
NRTIs	Didanosine, Stavudine	HIV
NtRTIs	Tenofovir, Adefovir, Cidofovir	HIV, Hepatitis B, CMV
Platinum compounds	Cisplatin/carboplatin	Cancer
Salicylates	Aspirin	Analgesia, anti-inflammatory
Tetracycline antibiotics	Degraded tetracycline	Bacterial infection
Tyrosine kinase inhibitors	Imatinib mesylate	Chronic myeloid leukemia

Platinum containing compounds and alkylating agents are indicated as therapy against cancer and are known to induce PT injury[101]. Within one class of agents different shades of toxicity exist. Cisplatin, for example, is more toxic than the related compound carboplatin, due to its greater uptake into the PT cells. Carboplatin in a concentration 10 times higher than a toxic concentration of cisplatin did not cause injury in a PT cell model[102]. The alkylating agent ifosfamide was shown to be rapidly taken up into the PT via organic cation transporters, where it is metabolized to toxic chloracetaldehyde[103].

An emerging problem in causes of renal Fanconi syndrome are anti-viral drugs. In the treatment of infections with HIV, antiviral drugs need to be taken lifelong. The chronic exposure leads to increased levels of the drug in the kidney, increasing the risk for nephrotoxicity. The nucleotide reverse transcriptase inhibitors adefovir, cidofovir and tenofovir are probably entering the PT cell via organic anion transporters[104, 105]. Due to the high risk of adefovir and cidofovir in inducing renal Fanconi syndrome, tenofovir has been developed as a safer alternative. However, numerous cases reporting renal Fanconi syndrome occurred upon tenofovir treatment, although the majority of patients might develop minor tubular defects that remain undetected at first[106, 107]. A mitochondrial involvement in the mechanism of tenofovir associated nephrotoxicity seems likely, since mitochondrial damage, in the form of grossly enlarged organelles, has been reported in patient biopsies[108].

Treatment of bacterial infections with aminoglycosides is effective but limited to the nephrotoxicity of these drugs. Within the class gentamycin appears to be more toxic than tobramycin and amikacin[109]. Unfortunately, infections with multi-resistant bacteria require the use of reserve antibiotics (for example Polymyxin B, a polypeptide antibiotic and known to cause kidney injury[110, 111]) or combinations of different antibiotics, which increases the risk of toxicity. Due to their uptake by endocytosis via megalin, aminoglycosides and polymyxins not only cause kidney injury, but also affect the inner ear with their ototoxicity (megalin is also expressed there explaining the accumulation in kidney and ear)[112, 113].

Other agents inducing Fanconi syndrome include suramin, tyrosine kinase inhibitors and salicylates[91]. The latter have been reported to interfere with mitochondrial function and the induction of mitochondrial swelling[114-116].

Relatively new in the field of Fanconi syndrome inducing drugs is the iron chelator deferasirox (DFX). In the first year after approval and release on the market, DFX was ranked second on the list of drug associated patient deaths by the Institute for safe medical practices (ISMP)[117], due to the unknown side effect of nephrotoxicity. The mechanism of toxicity is as yet unknown, wherefore this study investigated the effect of DFX on the PT.

1.5 Deferasirox (DFX)

DFX is a relatively new, tridentate iron chelator, that was approved by the FDA in 2005 and one year later by the European Medical Agency[118, 119]. The goal in the development of DFX was to improve the therapy for removing non transferrin bound iron by designing an iron chelator that can be administered orally[120]. The treatment of β-thalassemia (a defect in the β-globin chain of haemoglobin leads to an accumulation and precipitation of α-globin in red blood cell precursors resulting in anaemia) relies on blood transfusion[121]. As a result of the transfusions and the inability of the human body to actively excrete iron, the amount of iron increases to lethal levels, wherefore iron chelation therapy is needed[122]. The introduction of deferoxamine (DFA, Figure 5) in 1963 as the first iron chelator used in thalassemia marked a breakthrough in the therapy of these patients, as the reduced iron burden lead to a reduced iron-related morbidity and mortality[123]. DFA mobilizes the iron storages by binding solubilized iron and shifting the balance between the free and the insoluble hemosiderin, the insoluble deposition form of iron[124]. The chelated, now solubilized iron can then be excreted. Although DFA is efficient in removing iron, there are some drawbacks due to the bioavailability of the drug. The short plasma half-life and the poor oral bioavailability, require slow subcutaneous or intravenous infusions daily, as plasma levels of the drug only remain elevated during the perfusion[120].

In 1980 desferrithiocin (Figure 5) was isolated from Streptomyces antibioticus and was found to be a potent iron chelator with oral bioavailability[125]. Although single doses did not seem to cause toxicity, desferrithiocin did cause nephropathy in a subchronic 10 day study in rats and induced degenerative changes in the PT. Since nephrotoxicity also occurred in dogs, further development of desferrithiocin was stopped in 1986[121].

Parallel to the continuing efforts to create an orally available iron chelator similar to desferrithiocin with less severe side effects by the oral chelator program of Ciba (now Novartis), the iron chelator deferiprone (DFP, Figure 5) was discovered in 1993, before being approved by the European Medical Agency (1999) and the FDA (2011) [120, 126]. DFP appears to be less efficient in chelating iron and is used if an inadequate response to other chelators occurred or in case of severe iron overload in combination with another iron chelator. The main side effects of DFP do not involve nephrotoxicity, but are agranulocytosis and hepatic fibrosis, as DFP seem to redistribute the iron towards the liver[127, 128]. Unfortunately DFP has the disadvantage of achieving therapeutic plasma levels only by administering the drug every 6 hours[120].

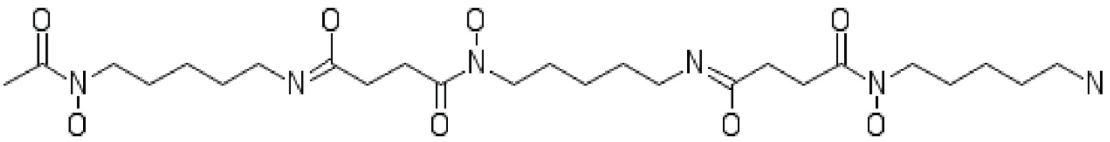

Deferoxamine DFA

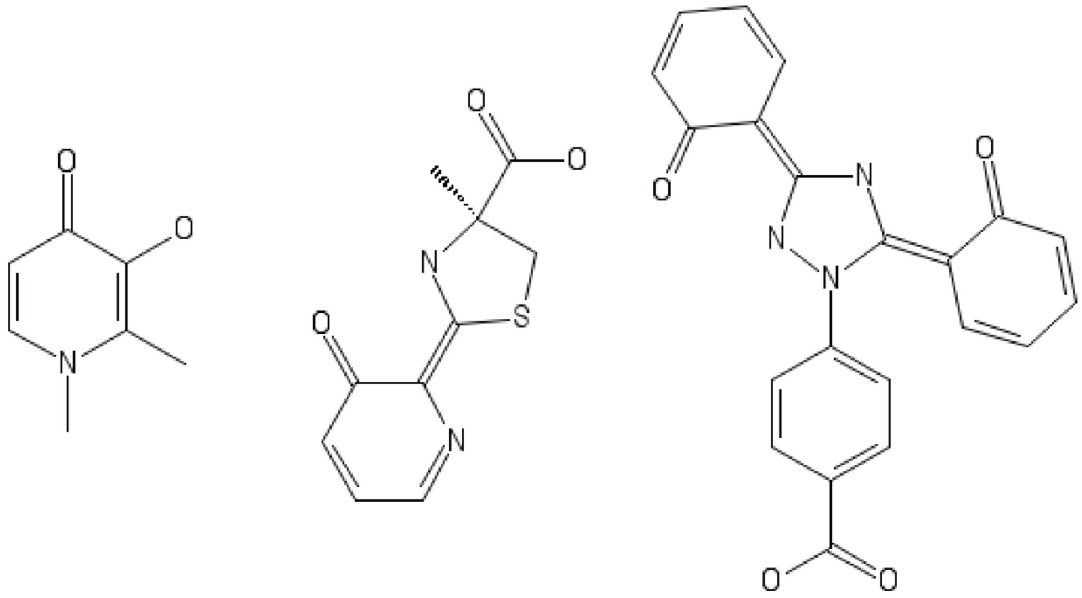

Deferiprone DFP Desferrithiocin Deferasirox DFX

Figure 5: Chemical structure of different iron chelators. DFA has to be administered subcutaneously or intravenously. DFP can be taken orally but has to be taken every 6 hours. DFX was developed based on the chemical structure of desferrithiocin – a natural occurring iron chelator with severe nephrotoxicity – and can be taken orally once a day.

Further work in the oral iron chelator program, lead to the discovery that bis-hydroxy-phenyl triazole is the ideal basic structure for an oral iron chelator, which allows ideal positioning of the hydroxyl-groups and the coordinating nitrogen. The central coordinating nitrogen in the tridentate chelator backbone is the feature that is shared with desferrithiocin. Among the huge number of tested compounds with similar chemical features (many of them barely water soluble), ICL670 (DFX, Figure 5) was found to be generally well tolerated in rat and Marmoset making DFX the most promising candidate[121] and was designated an orphan medicine by the European Medical Agency in 2002. DFX was shown to be more effective in chelating iron – especially rapid chelation occurred in the kidney - than DFA and DFP in iron-overloaded rats[121]. The excretion of DFX appeared to be mainly via the bile (urinary excretion was only observed after a large dose), whereas DFA is known to be excreted mainly via the urine and for iron chelated in hepatocytes via feces. Similar results were also observed in iron-overloaded Marmosets, showing a higher efficiency of DFX in chelating iron than DFA and DFP[129]. In rats DFX accumulates in the kidney cortex (631 nmol/g) compared to blood levels (213 nmol/mg), which is most likely the explanation for the PT specific toxicity[130]. In the first clinical studies no major side effects occurred in healthy and

thalassemic patients, while the excretion occured, as studied before, via feces[131, 132]. DFX in a concentration of 20 mg/kg/day was shown to be as effective as 40 mg/kg/day DFA[133]. A mild increase of urinary protein excretion was observed in a 6-month clinical trial, indicating mild effects on the kidney.

DFX and the DFX-iron complex are 98.2 % – 99.6 % bound to plasma proteins. In humans DFX showed a bioavailability of 70 %. After daily dosing of 20-30 mg/kg therapeutic concentrations ranging from 100-200 µM can be achieved. Amongst all patients investigated during clinical studies 36.3 % showed serum creatinine increases over 33 % at no less than two consecutive visits. A dose reduction could restore normal kidney function. Therefore, it was suggested that the adverse effects were caused by an overchelation[130].

The most relevant findings regarding adverse effects of DFX was nephropathy consisting of tubular degeneration, cytoplasmic vacuolization of cortical tubular epithelial cells and tubular necrosis, which was observed in all investigated species.

The problem of nephrotoxicity induced by DFX is still debated since long-term studies are missing[134]. At least the increase in DFX-associated deaths led regulatory agencies to require a boxed warning on prescription information of DFX in 2010[119]. The nephrotoxicity manifests as renal Fanconi syndrome, a generalized dysfunction of the PT. The onset of Fanconi syndrome after the start of DFX therapy has a mean of 17.8 months (1 – 36 month range) and is reversible within 3 weeks of discontinuation of the drug (3 days to 6 weeks), whereby it is more common to occur in very young (≤ 16 years) and elderly patients (≥ 65 years)[135-140].

In summary, the discrepancy among different studies concerning the incident of kidney toxicity upon DFX treatment is founded in the lack of a generalized system of evaluating kidney function and the definition of different thresholds defining toxicity[119]. Biomarkers used, such as serum creatinine, lack sensitivity and only increase after severe damage has occurred. Therefore, it is still necessary to improve methods for detection of kidney injury. Developing a better understanding of how renal toxicity develops can aid in identifying an early marker[141].

The focus of this study is to identify the mechanism of DFX toxicity. The main issues are why toxicity is localized to the PT, and whether and why the toxicity is an off-target effect or related to the chelation of iron. Comparing DFX toxicity to nephrotoxicity of, for example, tenofovir might be misleading, since both molecules possess different structures. Nevertheless, a general feature of PT specific damage is accumulation of drugs that are excreted by tubular secretion. This grants access to the PT cell and the potential to accumulate. Furthermore, an interference with mitochondria could lead to a transport

dysfunction. Since iron is very important in mitochondria (see 1.3.2), DFX might induce Fanconi syndrome via mitochondrial toxicity. DFX can also enter cells easily due to its high lipophilicity. Contradicting a tubular secretion is the fact that only a small percentage of DFX is eliminated urinarily, although the high affinity for binding plasma proteins makes a case for tubular secretion. Additionally, it has to be ruled out whether a metabolite of DFX is the trigger for toxicity (although most of the circulating drug remains unmetabolized). In preclinical studies an involvement of organic anion and cation transporters was already ruled out, but there is still a possibility of DFX being a substrate for MRP2. Furthermore, an investigation of DFX toxicity should also consider whether residues of the manufacturing process of DFX cause kidney toxicity (Figure 6). The educts of DFX include salicylic acid, which belongs to the group of non-steroidal anti-inflammatory drugs (NSAIDs), that are known to damage the kidney.

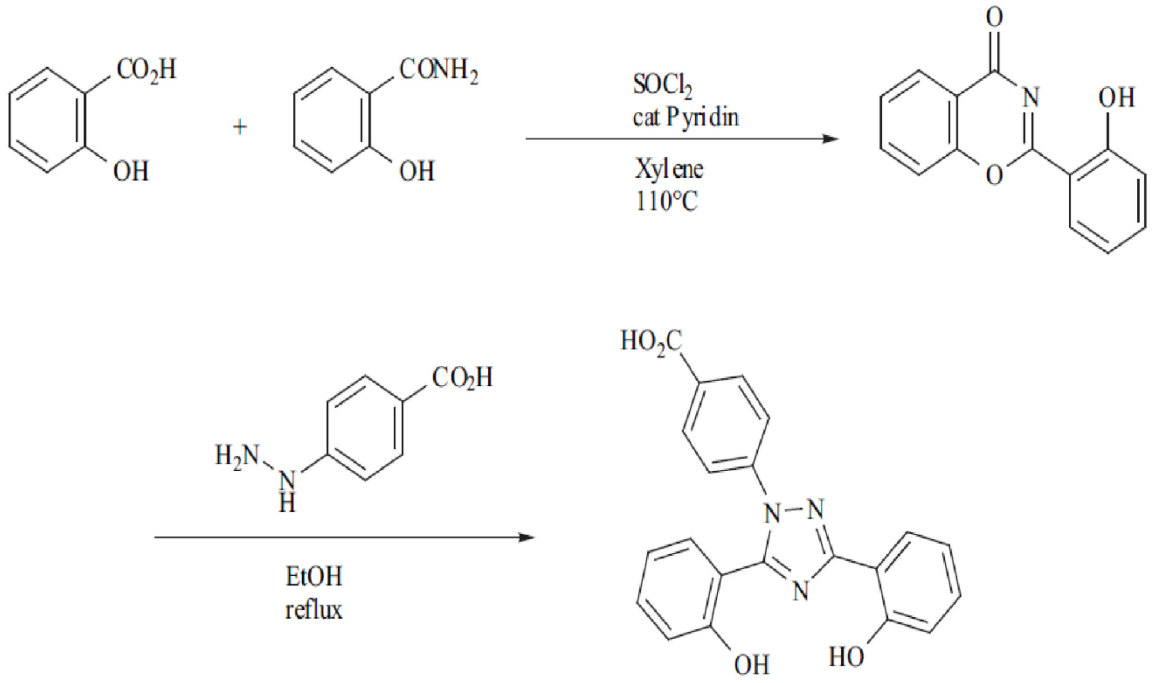

Figure 6: Synthesis of DFX in a twostep process. Salicylic acid and salicylic amide condensate mediated by thionylchloride to hydroxyphenylbenzoxazinone. After activation this intermediate reacts with hydrazines forming DFX (4-[3,5-Bis-82-hydroxyphenyl9-1,2,49triazol-1-yl]-benzoic acid). Taken from Nick et al. 2003[121]

1.6 Live imaging as an investigative tool for determining drug toxicity

Cell and animal models are used for the estimation of toxicity during drug development. The readout for the in vitro assays is often cell viability measured by ATP levels or membrane integrity[142, 143]. Those assays can be applied in a high-throughput manner, allowing screening of a huge number of drug candidates. However, minor changes in cell metabolism are often missed since they do not directly cause cell death. Therefore, once chemicals are developed further and tested in animal studies, the metabolic changes on a cellular level become visible, causing toxicity in the animal. To further reduce the number of animals used for toxicity testing and to lower the costs in drug development, it would be beneficial to already have a better, high-throughput applicable readout predicting toxicity. Advances made in imaging techniques and image processing tools enabled a high content screening, where multiple markers of cell health and metabolism can be read simultaneously[144]. This allows predictions of toxic effect with a high sensitivity and a low false positive rate. In addition, the changes detected already indicate the intracellular location of toxicity. Combining imaging techniques and improvement of cell models can enhance the safety in drug development in an early stage, although the interrelationship between the organs has still to be modelled in animal and in human clinical trials.

The main techniques used in this study for the investigation of the effects of DFX on the kidney were confocal and multiphoton microscopy.

1.6.1 Confocal microscopy

Confocal microscopy is a form of fluorescence microscopy that can be used to study fixed or living cells. Fluorescence microscopy is based on the phenomenon that electrons of certain molecules (so called fluorophores) can get excited to a higher state by absorbing a photon of a certain wavelength. To return to ground state the excess energy is emitted by light in a longer wavelength than the excitation wavelength (Stoke's shift), and by vibration or heat[145, 146] (Figure 8 A). In widefield microscopy the whole sample is illuminated and fluorescence signals from all positions in the sample are collected limiting the resolution. In confocal microscopy the excitation light is focused into a single spot in x,y direction by the use of a pinhole (the whole z direction remains illuminated). Emitted light is passed through further lenses and filters removing possible contaminations of different fluorophores. After passing through a pinhole, which removes out of focus fluorescence, the collected photons hit the detector where the signal is converted into an electrical signal, enhanced and with the aid of imaging software displayed as a digital image[147] (Figure 7). Detectors convert the energy of the incoming photons into electrical energy by a photocathode and enhances the signal via a series of other electrodes. The specimen is scanned point by point to recreate

a 2D or 3D image of the sample. The second pinhole removes a lot of the emitted light lowering the signal intensity. Enhancement of the signal by increasing the intensity of the excitation wavelength has to be done cautiously, due to possible bleaching. Signal enhancement can also be achieved by adjusting the voltage of the detector or can be performed during image processing, for example by deconvolution of the image. A further enhancement of the resolution can be achieved through stochastical methods (STORM stochastic optical reconstruction microscopy) or by STED (stimulated emission depletion) imaging, where excitation of fluorophores surrounding the point of interest is depleted by the use of a second laser[148, 149].

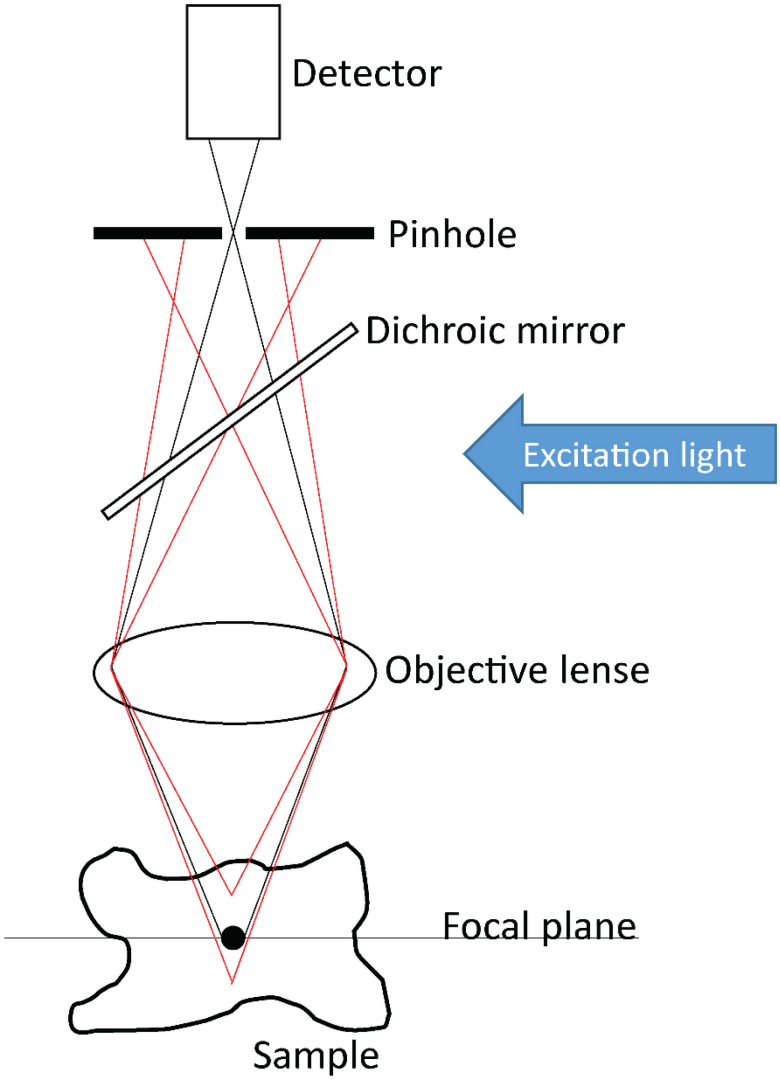

Figure 7: Principle of confocal microscopy. Excitation light is reflected toward the sample by the dichroic mirror and is focused by the objective. Emitted light passes through the dichroic mirror and is collected by the detector. Out of focus light is not collected due to the presence of the pinhole.

For live cell imaging it is important to have reporters (fluorophores) for different readouts. Properties of fluorophores can be altered in response to changes in calcium, oxidative stress or pH enabling the study of changes of these molecules. Other fluorophores specifically label certain organelles or structures within the cell by an accumulation at the target structure.

Live cell imaging is especially beneficial for studies on mitochondria in their native environment. Labelling of mitochondria with GFP allows the tracking of morphology and dynamics independent of the energization state of the mitochondria. $\Delta\Psi_m$ is central to mitochondrial function, affecting processes such as ATP and ROS production, and Ca^{2+} and protein import. The positively charged, lipophilic, fluorescent dye tetramethyl rhodamine methyl ester (TMRM) accumulates in the matrix of mitochondria, which is negatively charged compared to the cytosol[55]. The degree of the accumulation is proportional to $\Delta\Psi_m$, when the dye is used in the linear range (for example 50 nM). Using TMRM in higher concentrations leads to self-quenching of the fluorophore, hence to a decrease in signal. The application of an uncoupler, such as FCCP, causes the mitochondria to depolarize and TMRM to leak into the cytosol; if TMRM is used in a linear range the mitochondrial signal will decrease, if the dye was used in a self-quenching concentration the signal in the mitochondria will increase. A change in $\Delta\Psi_m$ can be caused by alterations of respiratory chain activity, the rate of ATP and the degree of proton leak.

Mitochondrial targeted toxins often induce ROS[150]. Upon oxidative stress intracellular levels of hydrogen peroxide increase. Hydrogen peroxide can for example be measured with the transfectable sensor Premo Cellular Hydrogen Peroxide Sensor Orp1-roGFP. Orp1 forms disulfides upon reaction with hydrogen peroxide and can transduce the signal to the coupled roGFP, which leads to protonation of GFP and increases the 400 nm excitation spectra at the expense of the 488 nm excitation spectra, allowing a ratiometric readout of hydrogen peroxide levels[151].
Bodipy 581/591 undecanoic acid can be used to detect lipid peroxidation. The oxidation of the polyunsaturated butadienyl portion of the dye results in a shift of the fluorescence emission peak from 590 nm to 510 nm[152]. The shift can be determined by measuring the ratio between the emission at both wavelength before and after the treatment.

A variety of Ca^{2+}-sensitive probes are available that can be loaded into cells and respond to Ca^{2+} by increasing their fluorescence[153]. Some of the sensors are known to accumulate in mitochondria (Rhod-2 and XRhod) and can be used to track Ca^{2+} levels inside the organelles[154, 155]. To ensure loading into the cells, most Ca^{2+} probes are prepared as an AM-

ester, which masks charged groups and enhances the lipid solubility. Intracellular esterases will release the hydrophilic fluorescent indicator to bind Ca^{2+} for the detection.

The fluorescent properties of NADH in ultraviolet light and of FAD^{2+} upon excitation with 450 nm can be used to determine the redox state of the cell[156]. The oxidized form of NADH and the reduced form of FAD^{2+} are not fluorescent. Measuring the relative intensity of the fluorescent signal arising from NADH and FAD^{2+} has been suggested to allow the deduction of the relative redox states of the two substrate pools[55]. Inhibition of respiratory chain, for example, would push the substrate pools into a reduced state, since they would no longer be oxidized by the respiratory chain complexes. The autofluorescence signal from NADH would be maximal, whilst the FAD^{2+} signal being minimal. On the other hand uncoupling of respiratory chain with FCCP has the opposite effect since the substrates would be in the oxidized state. One caveat to the above is that this is not purely a readout of respiratory chain function, since the oxidized forms NAD^{+} and FAD^{2+} are continuously reduced in the citric acid cycle[56].

1.6.2 Multiphoton microscopy

Although confocal microscopy is a powerful tool to study the physiological process in cells, the technique reaches its limit in more complex structures such as slices of an organ or the whole organ. For single photon excitation of fluorophores, the wavelength used lies in the ultra violet to visible range. The short wavelength light does not penetrate tissue well and undergoes more scattering compared to longer wavelength (infrared) light. Additionally, the illumination along the z-axis causes even more problems, namely bleaching than in thin cell sections as described in 1.6.1.

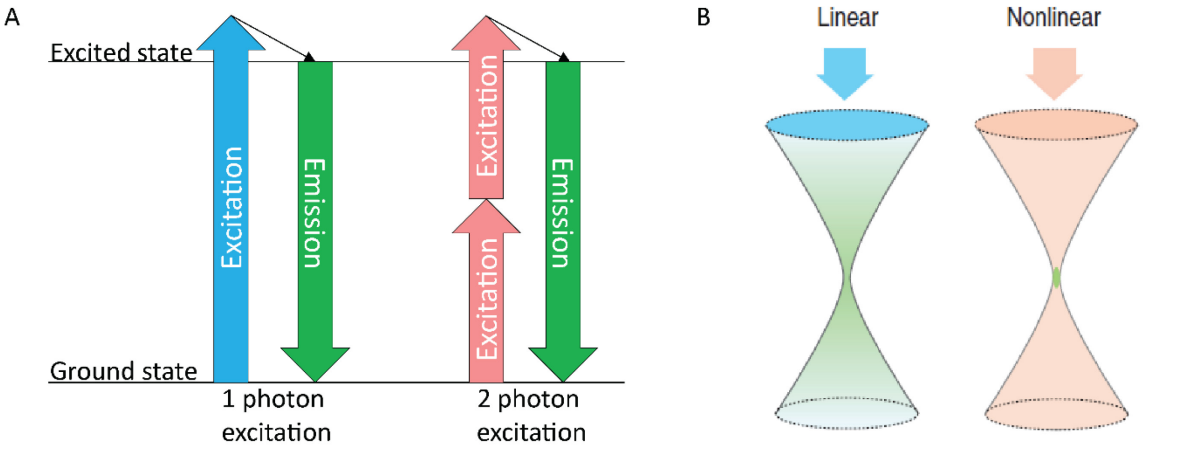

Figure 8: Differences between confocal and multiphoton microscopy. (A) One photon of a certain wavelength excites the fluorophore before light with a longer wavelength is emitted to return to the ground state with one photon excitation. Alternatively, fluorophores can get excited by 2 or more photons of longer wavelength arriving at the same time. (B) Linear illumination in confocal microscopy results in a cone of light around the focal point, whereas nonlinear illumination as performed in multiphoton microscopy does not induce excitation of the fluorophores in other planes[157]. (Green represents excited fluorophores in this scheme)

These disadvantages led to the development of multiphoton microscopy. The phenomenon of two photon absorption was first described in 1931 by Göppert-Mayer[158]. Two photons that arrive almost simultaneously (within 0.5 fs) at a molecule, can combine their energy to bring a fluorophore into an excited state, which then proceeds along the normal fluorescence to return to ground state[157, 159] (Figure 8 A). Similar multiple photons can combine to cause excitation. Since the arriving photon combine their energy, the wavelength of each photon is half the wavelength that is needed for a single photon excitation. In order for two photons to arrive at the fluorophore at the same time, the excitation light has to be concentrated in space and time. Focusing on one spot (space) can be achieved by using objectives with high numerical aperture; concentrating the signal in time requires a laser emitting ultrashort (less than a picosecond long) pulses with high intensity. The probability of two photons concurrently appearing outside of the focal point is very low. Therefore, excitation occurs in a single spot unlike the double cone illumination in

confocal imaging (Figure 8 B). This reduces the risk of phototoxicity. Additionally, the signal strength is increased compared to confocal imaging since no pinhole is needed. Furthermore, the use of higher wavelength light increases penetration depth by reducing scattering from the tissue[160].

Multiphoton microscopy is therefore an ideal tool to investigate cellular physiology in complex tissues and even enables intravital imaging in a subcellular resolution. This technique enables the visualization of mitochondrial morphology and function in the living animal, as shown recently by our group[160], and was therefore, in combination with live cell imaging and multiphoton microscopy of kidney slices[161], the ideal tool for investigating the mechanism of DFX induced kidney toxicity.

1.7 Aims of this work

1. To investigate whether the nephrotoxicity of DFX is due to a toxic effect on mitochondria, by describing the effect of DFX on mitochondrial morphology and function in PT cells.
2. To determine whether DFX toxicity is due to iron chelation or an off-target effect.
3. To establish whether DFX toxicity is specifically localized to the PT in an experimental mouse model, and if so, whether uptake of the drug by endocytosis might explain this.

2 MATERIALS AND METHODS

2.1 Materials

2.1.1 Technical equipment

Table 7. List of equipment and providers/manufacturers.

Equipment	Provider/Manufacturer
Seahorse XFp Analyzer	Agilent
Synergy 2, Multidetection reader	Biotek
EM HPM 100, high pressure freezer	Leica
Ultracut E, Ultramicrotome	Reichert
SP8 inverse STED 3X, microscope	Leica
SR GSD 3D microscope	Leica
Microm HM 650 F, Vibratome	Thermo Scientific
Fluoview 1000 multiphoton microscope	Olympus
Libra S70 double beam spectrophotometer	Biochrom
Mini-Extruder, 0.1 µm pore size nucleopore polycarbonate membrane	Avanti

2.1.2 Chemicals and reagents

Table 8. List of chemicals and reagents including supplier.

Chemical/Reagent	Provider
Acutase	Thermo Fisher Scientific
Amplex Red Hydrogen Peroxide/Peroxidase Assay Kit	Thermo Fisher Scientific
Antimycin A	Sigma Aldrich
Ascorbate	Sigma Aldrich
Bovine Serum Albumin	Sigma Aldrich
Cadmium	Sigma Aldrich
Cardiolipin	Sigma Aldrich
Catalase	Sigma Aldrich
Cisplatin	Sigma Aldrich
Colchicine	Sigma Aldrich
Cyanide	Sigma Aldrich
Cyclosporine A	Sigma Aldrich
Cytochalasin D	Sigma Aldrich
Cytochrome C	Sigma Aldrich
Deferasirox	Selleckchem and Biochempartner
Deferiprone	Sigma Aldrich
Deferoxamine	Sigma Aldrich

Chemical/Reagent	Provider
Diclofenac	Tocris Biosciences
Dimethylsulfoxide	Sigma Aldrich
DMEM/F-12	Thermo Fisher Scientific
Dodecyltriphenylphosphoniumbromide	Sigma Aldrich
Fetal bovine serum (FBS)	Thermo Fisher Scientific
FCCP (Carbonyl cyanide-*4*-(trifluoromethoxy)phenylhydrazone)	Sigma Aldrich
Glacial Acid	Sigma Aldrich
Hydrazinobenzoic Acid	Sigma Aldrich
Hydrogen Peroxide	Sigma Aldrich
Iron (III) Ammonium Citrate	Sigma Aldrich
Loctite 406	Distrelec
MitoQ	MedKoo
Neutral Red	Sigma Aldrich
Oligomycin	Sigma Aldrich
Paraformaldehyde	Sigma Aldrich
Pluronic	Sigma Aldrich
RAP	Molecular Innovations
Salicylic Acid	Sigma Aldrich
Simvastatin	Sigma Aldrich
SS-31	China Peptides
TMPD	Sigma Aldrich
Triton-X 100	Thermo Fisher Scientific
Trypan blue	Sigma Aldrich, 0.4 % diluted to 0.05 % in PBS
Tween	Thermo Fisher Scientific
Valinomycin	Sigma Aldrich
Verapamil	Sigma Aldrich

2.1.3 Dyes

Table 9: Dyes for live cell imaging

Dye	Excitation/Emission	Concentration	Provider
Albumin-AF488	488/525	600 µg/120 µl	Thermo Fisher Scientific
Bacmam Mito GFP	488/508	5 particles per cell + enhancer	Thermo Fisher Scientific
Bodipy 581/591 C11	510+580/581+591	2 µM	Thermo Fisher Scientific
Calcein	495/515	50 mM	Sigma Aldrich
Calcein AM	495/515	250 nM with 2.5 mM Probenecid	Thermo Fisher Scientific
ER tracker blue white	405/555	1 µM	Thermo Fisher Scientific
Mitotracker deep red	644/660	200 nM	Thermo Fisher Scientific
Mitotracker green	488/510	200 nM	Thermo Fisher Scientific
Premo Cellular Hydrogen Peroxide Sensor	400/488+515	80 particles per cell + enhancer	Thermo Fisher Scientific
Rhodamine 123	505/530	50 nM	Thermo Fisher Scientific
SiR tubulin	650/675	2 µM with 10 µM verapamil	Spirochrome
Tetramethylrhodamine (TMRM)	555/580	50 nM	Thermo Fisher Scientific
XRhod	580/600	2 µM	Thermo Fisher Scientific

2.1.4 Buffers and solutions

Table 10. Compositions of buffers and solutions

	Composition
PBS	136.89 mM NaCl, 2.68 mM KCl, 10.14 mM Na_2HPO_4, 1.76 mM KH_2PO_4, adjusted to pH 7.4
Cell buffer	138 mM NaCL, 5.6 mM KCl, 1.2 mM NaH_2PO_4, 2.6 mM $CaCl_2$, 1.2 mM $MgCl_2$, 10 mM glucose, 4.2 mM $NaHCO_3$, 10 mM HEPES, adjusted to pH 7.4
Kidney slice buffer	118 mM NaCl, 4.7 mM KCl, 1.2 mM KH_2PO_4, 1.8 mM $CaCl_2$, 1.44 $MgSO_4$, 5 mM glucose, 10 mM $NaHCO_3$, 10 mM HEPES, 5 mM pyruvate, 2.5 mM sodium butyrate, 2.5 mM sodium lactate, adjusted to pH 7.4 and gassed with carbogen (95 % O_2/ 5 % CO_2)
Liposome buffer	100 mM KCl, 10 mM Tris, 10 mM MES
PHEMO buffer	68 mM PIPES, 25 mM HEPES, 15 mM EGTA disodium, 3 mM $MgCl_2$,adjusted to pH 6.8
0.1 M phosphate buffer	19 mM NaH_2PO_4, 81 mM Na_2HPO_4, 230 µM $CaCl_2$, adjusted to 300 mOsm and pH 7.4

2.1.5 Antibodies

Table 11. List of monoclonal (m) or polyclonal (p) primary and secondary antibodies used for immunofluorescence (IF)

Antibody (against)	Fluorophore	Host	m/p	Dilution	Provider
TOM-20	--	rabbit	p	1:150, 1:125 for STED	Santa-Cruz, sc11415
Cytochome C	--	mouse	m	1:50	Biolegend, 6H2.B4
rabbit	Alexa 488	donkey	p	1:500	Jackson Immuno Research
rabbit	Abberior Star 635	goat	p	1:200	Abberior GmbH
rabbit	Alexa 555	goat	p	1:200	Thermo Fisher Scientific
mouse	Atto 594	goat	p	1:200	Sigma Aldrich

2.1.6 Software

Table 12. List of software used for analysis, visualization and interpretation of data.

Software	Provider
Adobe Illustrator	Adobe Systems
Fiji	Open Source
Graph Pad Prism	GraphPad Software, Inc.
Huygens Professional deconvolution	Scientific Volume Imaging

Software	Provider
Ilastik	Open Source
Leica LAS AF Lite	Leica
Mahematica	Wolfram Research

2.1.7 Statistical analysis

All statistical analysis was performed using Graph Pad Prism. Significance of differences between control and treatment was tested with a 1-way ANOVA, posthoc Dunnett's multiple comparison test. All experiments were at least performed in triplicates.

2.2 *In vitro* studies

2.2.1 Cell lines

OK cells, a proximal tubular cell line from opossum kidney, were a kind gift from the group of Prof. Olivier Devuyst (Institute of Physiology, University of Zurich). Currently, OK cells remain the preferred model for the S1 segment, as it mostly resembles ion transport functions from the PT, expresses megalin, has a robust apical endocytosis and is well differentiated[162]. The OK cells were grown in DMEM/F-12 medium supplemented with 10 % FBS under standard tissue culture conditions (37°C, 5 % CO_2). Splitting took place once per week and was performed as follows: after removal of medium cells were washed once with PBS (37°C), before 1 ml of accutase was added and cells were allowed to detach for 10 min at 37°C. The enzymatic reaction of acutase was stopped by the addition of 10 ml of warm culture medium with 10 % FBS, before the cell suspension was centrifuged at 200g for 5 min. The medium was removed, and the cell-pellet was resuspended in 6 ml warm culture medium. For cell counting 20 µl of cell suspension were mixed with 60 µl 0.05 % trypan blue and added in a hemocytometer. Only viable cells did not take up trypan blue due to an intact cell membrane were counted. The cell number was calculated using the following formula: viable cells per ml suspension = number of viable cells in one big square x 4 (dilution factor) x 10^4. Appropriate cell concentrations for seeding into different culture formats (Table 13) were gained by dilution with culture medium. Cells were used from P 20 to P35.

Table 13: Cell densities of OK cells

Format	**Cell density per well**	**Volume per well**
75 cm^2 flask	3.5 x 10^5	10 ml
25 cm^2 flask	1 x 10^5	5 ml
12 well plate	1.8 x 10^5	1 ml
4 well imaging chamber	1.4 x 10^5	500 µl
96 well plate	1 x 10^4	100 µl
Seahorse plate	5 x 10^3	70 µl

To label mitochondria with GFP, cells were incubated for 2 hours with CellLight Mitochondria-GFP BacMam 2.0 (5 particles per cell) and BacMam enhancer (both Thermo Fisher Scientific) one day prior to experiment. For the detection of intracellular H_2O_2, cells

were exposed to Premo Cellular Hydrogen Peroxide Sensor Orp1-roGFP (80 particles per cell) and BacMam enhancer 24 hours before microscopic analysis.
For the analysis of cytochrome c release by immunostaining, a different cell line, COS-7, had to be used due to incompatibility of the antibody with OK cells. COS-7 cells were kindly provided and grown by the Centre for Microscopy and Image Analysis of the University of Zurich. They were cultivated under standard conditions in DMEM medium containing 4.5 g/l D-glucose, 10% FBS and 1% L-glutamine.

2.2.2 Cell viability assay (Neutral Red Assay)

Cell viability in response to DFX treatment was assessed using the Neutral Red Assay[142]. The assay is based on the ability of the weakly cationic dye neutral red to penetrate cell membranes by passive non-ionic diffusion. The dye accumulates in lysosomes, where it binds to anionic and/or phosphate groups by electrostatic hydrophobic bonds. Due to the acidic pH in lysosomes neutral red changes its net charge and can no longer leave the lysosome. The pH in lysosomes is maintained by the proton gradient, which is generated by the proton pumping V-type ATPase. The enrichment of neutral red in the lysosomes therefore reflects cellular ATP levels and cell viability.
For the assay OK cells were seeded in 96 well plates one day prior to treatment with DFX for 24 h. Upon the start of the assay, cells were incubated for 2 h with neutral red medium at 37°C to allow the dye to be enriched in lysosomes. Excess dye, that did not change its net charge, was removed by washing with PBS. To measure the dye that was bound in the lysosomes, cells were lysed with 50 % ethanol, 49 % water and 1 % glacial acid, before optical density was measured at 540 nm using a multi detection reader. Measured values were normalized to control cells after the blank was subtracted.

2.2.3 Confocal live cell imaging

For confocal live cell imaging OK cells were seeded one day prior to the experiment on poly-L-lysine coated coverglasses (ø 18 mm, thickness 1) or in a CELLview dish with 4 wells and grown to a confluence of 70-90 %. For the coating coverglasses were placed into a 12 well plate (one per well), sterilized by incubation in 70 % ethanol for at least 5 min before 0.01 % poly-L-lysine was added and incubated at RT for at least 1 h. Excess poly-L-lysine was removed by washing 3 times with water before cells were plated.
For staining, cells were incubated at 37°C for at least 1 h in cell buffer (Table 10) containing the appropriate dye concentration (Table 9), before being mounted in a ludin chamber (mounting not necessary if cells were grown in CELLview imaging dish) and placed onto the stage of the microscope with controlled environmental conditions (37°C). Confocal

imaging was performed on a Leica SP8 inverse STED 3X equipped with a white light laser (470-670 nm), a diode laser 405 nm and a HC PL APLO STED WHITE 100x/1.4 objective. When new dyes or dye combinations were used for the first time, staining was monitored on stage to evaluate how long it takes to reach a stable baseline of signal. Laser intensities were tested on control cells to determine the intensity that does not induce damage but ensures sufficient signal to noise ratio.
Acute treatment with drugs was performed by addition of 2x concentrated drug solution into the live cell imaging chamber using a glass pipette, so as not to disturb the recording of the image series.

2.2.4 Immunofluorescence for confocal, STED and STORM imaging

Immunofluorescence staining was performed for confocal, STED and STORM, both super resolution microscopy methods.
Immunofluorescence is based on the detection of the protein of interest by its interaction with a specific antibody, the so called primary antibody. Binding of the polyclonal, fluorescently labelled secondary antibody to the primary antibody multiplies the signal and allows the localization of the protein of interest using fluorescence microscopy (all antibodies and their dilutions are listed in Table 11). STED and STORM microscopy both allow imaging in a resolution beyond the defraction limit[148, 149]. This is achieved in STED microscopy by depleting out of focus fluorescence that occurs by excitation of the fluorophores. The so-called depletion laser is donut shaped surrounding the excitation laser and allows an increased resolution. In STORM a strong laser pushes the fluorophores into a dark state from which single molecules may return into an emissive state. This allows the localization of single fluorophores. During long measurements (almost) every molecule will once return into the emissive state, allowing a reconstruction of the actual localization of all fluorophores in one image.

OK cells or - for STED imaging of cytochrome c - COS-7 cells, were grown as described in chapter 2.2.3 on coated coverglasses. After treatment with the control medium and DFX, the remaining medium was removed by washing it with warm PBS. For confocal and STED imaging cells were fixed at RT for 10 min with 3 % paraformaldehyde in PBS (30 g/l, depolymerized to formalin after heating), which crosslinks proteins, primarily lysine residues. Permeabilization with 0.1 % TritonX-100 for 5 min ensured that the primary antibody can reach the target protein. After washing three times with PBS, nonspecific binding of the primary antibody was prevented by blocking for 30 min at RT with 1 % BSA. For confocal imaging, samples were additionally blocked with donkey serum diluted 1:10 in the BSA solution. Afterwards, cells were incubated with the primary antibody TOM-20

(rabbit, polyclonal) diluted 1:150 in the 1 % BSA solution overnight. Excess antibody was removed in three washing cycles using PBS, before cells were incubated with the secondary antibody (donkey anti rabbit conjugated with Alexa 488) diluted 1:500 in 1 % BSA solution for 2 h at RT. After washing 3 times with PBS, coverglasses were mounted on glass slides using DAKO glycergel mounting medium as embedding medium. Once the mounting medium dried the edges of the coverglass were sealed with clear nail polish.
Differences of the staining for confocal imaging and STED microscopy were the dilution of antibodies – primary: 1:125 for TOM-20 and 1:50 for cytochrome C (mouse, monoclonal); secondary: 1:200 goat anti rabbit coupled to Abberior Star 635 and 1:200 goat anti mouse coupled to Atto 594 – and the mounting medium ProLong Diamond antifade mountant.
For STORM imaging it was important to use secondary antibodies conjugated with dyes that demonstrate a better “blinking” behavior (switch from dark to emitting state) and that the generation of radicals due to the long imaging duration is restrained. After the treatment OK cells were fixed using 37°C PHEMO buffer supplemented with 3.7% formaldehyde and 0.05 % glutaraldehyde for 10 min at RT. After washing with PBS, cells were permeabilized with 0.1 % TritonX-100 for 1 min, washed again with PBS and blocked with 1 % BSA for 30 min at RT. Primary (1:150 TOM-20) and secondary antibody (1:200, goat anti rabbit conjugated with Alexa 555) were both incubated for 1 h at RT, with three washes using PBS in between. To minimize radical generation during imaging, cells were mounted in vectashield/50mM Tris in 87 % glycerol (1/2.15) and sealed with 2 component Twinsil 22.
Confocal and gated STED imaging of the fixed samples was performed on a Leica SP8 inverse STED 3X using the HC PL APO STED WHITE 100x/1.4 objective and white light laser as described in section 2.2.3. For STED imaging, in addition to the excitation of the fluorophores at 585 nm (Atto 594) and 635 nm (Abberior Star 635), the depletion laser was used at full power and a wavelength of 775 nm.
3D STORM imaging was performed on a Leica SR GSD 3D microscope using a HCX PL APO (GSD/TIRF) 160x/1.43 objective. Excitation was performed using a 642 nm laser and a 710/100 bandpass was used for the emission.

2.2.5 Image analysis

Data from confocal and STED imaging was deconvolved using Huygens Professional software. Image processing for all microscopy data was done in FIJI and Imaris 8.3. 3-D STORM images were processed using FIJI and the ThunderSTORM plugin[163]. To investigate the effect of DFX on mitochondrial energization, the GFP-mitochondrial channel of the image time series was segmented, and the resulting mitochondrial localization tracked over time using supervised machine learning (Ilastik: Interactive learning and segmentation toolkit, http://doi.org/10.1109/ISBI.2011.5872394). Using the tracking results,

intensities of both the GFP and the TMRM channel were extracted using FIJI. The obtained fluorescence intensity data was combined to trajectories and further analyzed and visualized using Mathematica. The bimodal distribution of the TMRM signal allowed the calculation of a polarization survival probability using fixed thresholds. For the long term dynamic effect the same approach was used, and 36 randomly acquired images containing mitochondrial signals from multiple cells were analyzed per time point.

2.2.6 Respirometry

For the evaluation of the effect of DFX on oxidative phosphorylation, oxygen consumption was measured using a Seahorse XFp analyzer. The measurement is based on a fluorophore sensitive for oxygen that is integrated into a cartridge, which is lowered down to the cells creating a transient chamber (distance fluorophore to cells 200 µm) that allows localized measurements of the decay of oxygen concentration.

One day prior to the experiment, cartridges were hydrated with XF calibrant (200 µl per well, 400 µl per moat, incubation at 37°C without CO_2 until use) and cells were plated in Seahorse XFp 8 well culture plates, whereby one well was not filled with cells to serve as a blank in the assay. One hour before analysis cells were incubated without CO_2 in cell buffer (Table 10, 200 µl per well). In the meantime, cartridges were filled with the stock solutions of drugs dissolved in cell buffer according to Table 14.

Table 14: Scheme for cartridge loading for respirometry

	Port	**Stock**	**Concentration in port**	**Injection volume**	**Concentration on cells**
DFX	A	100 mM	2.2 mM	20 µl	200 µM
Ascorbate/TMPD	B	800/200 mM	34/8.5 mM	13.75 µl	2/0.5 mM
Cyanide	C	500 mM	9 mM	13.75 µl	500 µM
Complex III blocking	**Port**	**Stock**	**Concentration in port**	**Injection volume**	**Concentration on cells**
Antimycin	A	100 mM	52.5 µM	10 µl	2.5 µM
DFX	B	100 mM	2.3 mM	20 µl	200 µM
Cyanide	C	500 mM	12 mM	10 µl	500 µM

After calibration of the cartridge in the Seahorse XFp (automated protocol from manufacturer) the cell plate was inserted into the machine. After the automatic equilibration,

baseline was measured in 3 cycles, each consisting of 2 min mixing and 2 min measuring. The same measurement procedure was performed after each injection of a drug. The values were analyzed using the software Wave and were normalized to the mean measurements of the baseline using Excel and Graph Pad.

2.2.7 Electron microscopy of OK cells

For transmission electron microscopy OK cells were grown in a 12 well plate on carbon coated (5-20 nm, for better attachment of the cells) 6 mm sapphire discs. Before the specimen carrier was assembled, a loading station was created by placing the middle plate "bridge-like" over two spacers (for example tape) on top of a petri dish. The slight elevation of the middle plate prevents capillary forces from drawing out medium from the cells. The 6 mm sapphire disc with the treated cells was placed on the edge of the middle plate hole with the cells facing up and covered with a 6 mm aluminium specimen carrier type A, wetted with hexadecane, leaving a gap of 100 µm between disc and carrier. To fill the remaining gap a 200 µm spacer ring was placed on top of the aluminium carrier (Figure 9). After the assembly in the middle plate cells were immediately high pressure frozen using a stream of liquid nitrogen running through the lower and upper half of the cylinder with a pressure of 2100 bar, ensuring high cooling rates and freezing of the sample within 2.5 s (Figure 9). After freezing the specimen the carrier was disassembled and the sapphire disc was kept in liquid nitrogen until freeze substitution was performed.

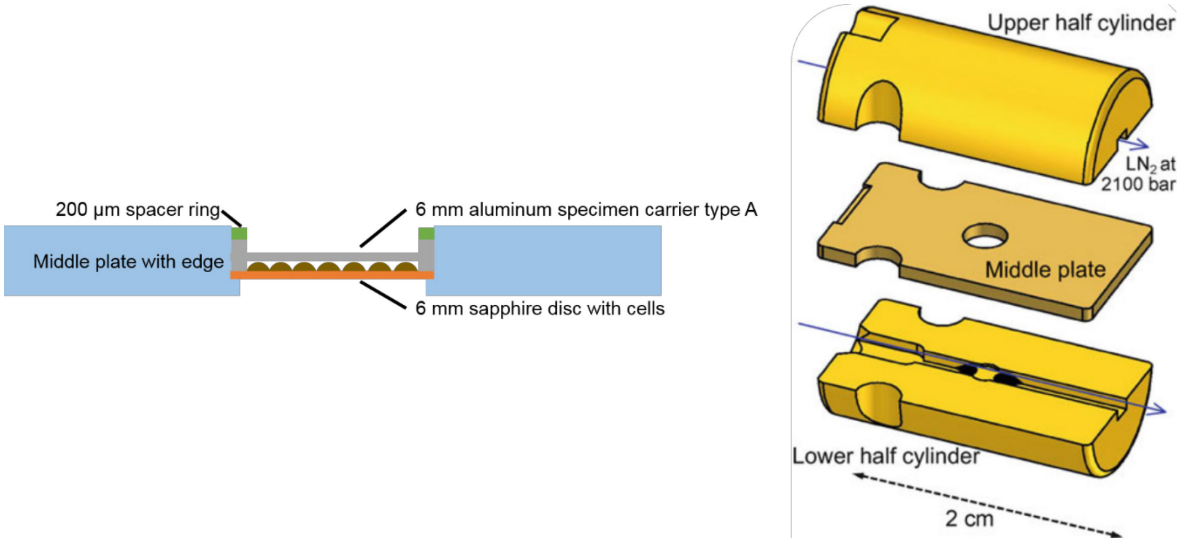

Figure 9: Specimen carrier assembly for high pressure freezing of cells grown on carbon coated 6 mm sapphire discs. During high pressure freezing a stream of liquid nitrogen at 2100 bar ensures high cooling rates on the sample assembled in the middle plate.

For the embedding in resin, water in the sample had to be replaced. Freeze substitution was carried out in water free acetone with 1 % OsO_4 (contrast enhancement) for 8 h at -90°C, 7 h at -60°C, 5h at -30°C and 1 h at 0°C with transition gradients of 30°C per hour.

Afterwards, samples were rinsed twice in water free acetone, before they were stained for 1 h in 1 % uranyl acetate (stock 20 % in methanol) in acetone at 4°C and rinsed again twice with water free acetone. For the embedding in the resin, samples were first incubated overnight in 66 % Epon/Araldite in acetone, then in 100 % Epon/Araldite for 1 h at RT, before the resin was polymerized for 20 h at 60°C.
70 nm thick sections were cut on an Ultramicrotome and images were acquired with an FEI CM 100 equipped with a Gatan Orius 1000 camera.

2.2.8 Calcein leakage in Liposomes

To evaluate if DFX creates pores in the inner mitochondrial membrane, liposomes with a lipid composition resembling the inner mitochondrial membrane were produced. The liposomes contained the dye calcein in a concentration of 50 mM. At this high concentration calcein is self-quenching, meaning less fluorescent. Upon rupture, calcein is released and diluted to a non-quenching concentration resulting in an increase in fluorescence, which is the readout for the assay (Figure 10)[164].

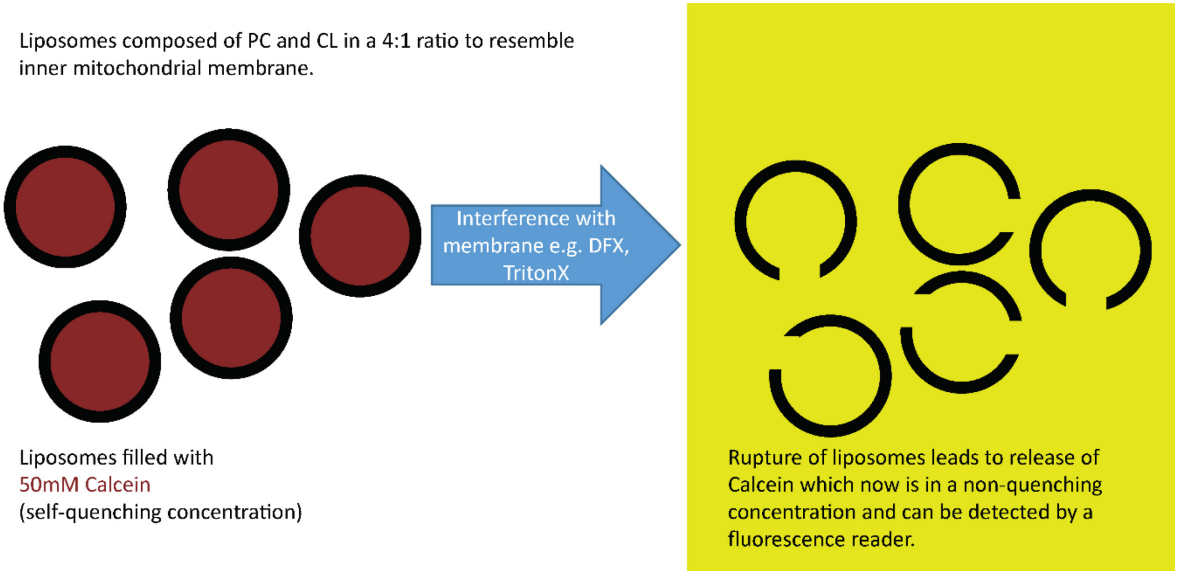

Figure 10: Principle of calcein leakage in liposomes. Liposomes, resembling the inner mitochondrial membrane, are filled with a self-quenching concentration. Upon rupture, calcein is released and diluted to a concentration where no self-quenching occurs inducing a rise in fluorescent signal.

At first the lipid mixture of 4 mg phosphatidylcholine and 1 mg cardiolipin was dissolved in chloroform and evaporated in a stream of nitrogen. The lipid mixture was then hydrated (2 % solution of lipids in buffer) with 1:2 diluted liposome buffer containing 50 mM calcein.
The calcein concentration had been determined prior to use by measuring the absorption at 495 nm compared to buffer without calcein as reference using a spectrophotometer. The concentration was calculated according to the law of Lambert-Beer using the equation c =

A/ε*l with c = concentration of calcein, A = measured absorption at 495 nm, ε = extinction coefficient of calcein 77000 cm^{-1} M^{-1} and l = length of used cuvette (here 1 cm).
After vortexing and several freeze thaw cycles the lipid dye mixture was extruded through a 0.1-µm pore size Nuclepore polycarbonate membrane using a mini extruder, resulting in liposomes filled with calcein. Excess dye was removed by dialyzing against liposomes buffer for 48 h at 4°C with slow stirring using Slide-A-Lyzer MINI 7K. Dialysis buffer was changed 6 times.
For the assay liposomes were diluted in liposome buffer to a concentration of 500 ng/ml. Fluorescence was recorded at 508-548 nm (excitation 465-505 nm) every minute using a Synergy multi detection reader. Before the addition of drugs (experimental conditions: buffer, DFX 200 µM and 1 mM, DTPP 200 µM, the detergent Triton-X 100 served as positive control and DMSO as solvent control) a baseline value (only liposomes in the well) was measured for 5 min.

2.2.9 Amplex Red Assay

Upon oxidative stress cytochrome c can act as a peroxidase inducing lipid peroxidation of cardiolipin, which leads to a disruption of cristae[165]. The mitochondrial targeted antioxidant SS-31 is thought to be protective during ischemia due to the protection of peroxidation of cardiolipin and due to its antioxidant properties[166]. As iron is crucial for the peroxidase activity of cytochrome c, DFX might provoke an increased activity of the peroxidase leading to the disruption of mitochondria.
To measure the activity of cytochrome c peroxidase an Amplex Red assay can be used. In the presence of peroxidase, the Amplex Red reagent reacts with hydrogen peroxide in a 1:1 stoichiometry to produce the red-fluorescent product resorufin[167]. The increase in fluorescence can be detected and is the readout for peroxidase activity. It was taken into account that cardiolipin enhances peroxidase activity, and that a decrease in peroxidase activity could also be due to an interaction with cardiolipin[168].
In 50 µl of 50 µM sodium phosphate (pH 7.4) cytochrome c (800 nM), cardiolipin (60 µM) and DFX (0.8 – 400 µM) or control were mixed and added into a well of a black 96 well plate, similar to previously reported cytochrome c peroxidase activity assays[164, 166, 169]. To start the reaction 50 µl of the mix of Amplex Red (40 µM) and hydrogen peroxide (50 µM) in 50 µM sodium phosphate were added. Immediately after addition of the dye and hydrogen peroxide fluorescence signal was read every 20 s for 10 min using a 540/20 filter for the excitation and 620/40 filter for emission on the Synergy 2 multi detection reader. The final concentrations of the single substrates in one well were 400 nM cytochrome c, 30 µM cardiolipin, 20 µM Amplex Red, 25 µM hydrogen peroxide and 0.4 – 200 µM DFX.

2.3 Animal studies

All experiments were performed on C57BL/6JRj mice from Janvier aged between 8 to 13 weeks. Animals were housed under standard conditions with standard chow. All animal experiments were approved by the Zurich Cantonal Veterinary Office (Licence 021/15).

2.3.1 Cortical kidney slices

After the evaluation of the effects of DFX in OK cells, the effect on kidney tissue was investigated using multiphoton microscopy. Mice were anaesthetized with intraperitoneal injection of Ketamine and Xylazine with a dose of 0.065 and 0.01 g/kg bodyweight, respectively, before kidneys were externalized. After the removal of the capsule one pole of the kidney was mounted onto the sample holder of the vibratome using a drop of glue (Loctite 406). To accelerate hardening of the glue one ml of kidney slice buffer was added, before the sample holder was placed into the vibratome, where it was cut into 250 µm thick sections. Until use the kidney slices were kept at 4°C in kidney slice buffer (Table 10) gassed with carbogen (95 % O_2/5 % CO_2). For staining with TMRM, kidney slices were incubated in 50 nM TMRM for 1 hour at RT prior to imaging. Kidney slices were then carefully mounted into a heated tissue slice chamber with gassed slice buffer for imaging. Imaging was performed with an Olympus Fluoview 1000 MPE equipped with a XPlan N 25x/1.05 objective, coupled to an ultrafast Ti:Sapphire laser system. For the detection of NAD(P)H the laser was tuned to 720 nm and for TMRM to 850 nm. Drugs were added directly into the chamber using a glass pipette.

2.3.2 In vivo treatment of mice with DFX

For the in vivo study of the effect of DFX on the PT, animals received a single intraperitoneal injection of 100 mg/kg bodyweight of DFX daily dissolved in saline and 0.16 % Tween for ten days. Control animals were injected with saline and Tween only. No change in behavior was detectable during the treatment period.

2.3.2.1 In vivo imaging

Intravital imaging was performed as described previously[160]. Mice were anaesthetized with 2.5 % isoflurane in 100 ml/min oxygen. The internal jugular vein was cannulated for the application of dyes and the kidney was externalized. Animals were then placed on a temperature-controlled holder, that was designed to dampen transmission of breathing movement to the kidney during image acquirement, and the kidney was fixed onto the holder using agarose (Figure 11). The temperature of the animal was monitored throughout the experiment.

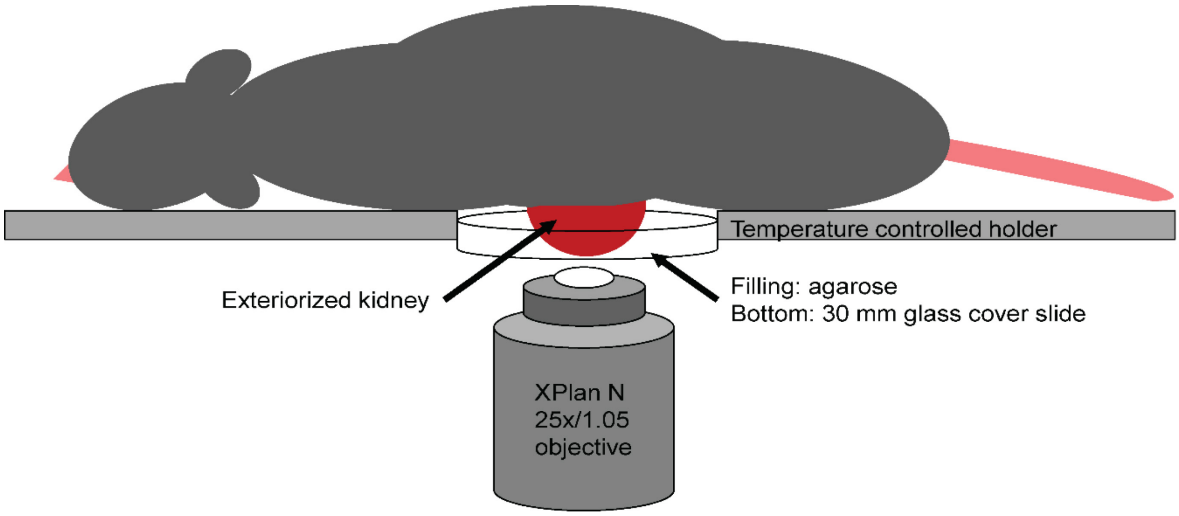

Figure 11: Schematic drawing of mounting the mouse on the multiphoton microscope for in vivo imaging. After cannulation of the jugular vein for dye application and the exteriorizing of the kidney, the mouse is placed onto the temperature-controlled holder. The kidney is stabilized by the addition of agarose and imaging is performed from below through a coverglass.

Imaging was performed on a custom-built multiphoton microscope operating in inverted mode equipped with a broadband (680 – 1300 nm) tunable laser (Insight DS Dual, Spectreaphysics) and a XPlan N 25x/1.05 water immersion objective.

To study mitochondrial morphology 30 µg of TMRM in 120 µl 0.9% saline were injected, while for investigating protein uptake 600 µg of Alexa 488 labelled albumin was injected in 120 µl 0.9% saline. Both dyes were excited at 800 nm and emission was detected using gallium-arsenide-phosphide (GaAsP) detectors with bandpass filters 525/50 and 605/50. For controlling image acquisition, the ScanImage 3.8 software package was used.

2.3.2.2 Electron microscopy of kidney tissue

To further evaluate mitochondrial morphology in mice treated with DFX, control and DFX exposed mice were anesthetized using isoflurane, before they were perfused via the abdominal aorta first with 30-50 ml 0.1 M phosphate buffer (Table 10) to remove blood before kidneys were fixed with 50 ml 3 % paraformaldehyde in 0.1 M phosphate buffer. After 5 min of fixation the animal was perfused with around 30 ml 0.1 M phosphate buffer, before kidneys were externalized. The capsule was removed, before each kidney was divided into 6 pieces by transverse sections. The sections (3 per 2 ml tube) were stored in 2.5 % glutaraldehyde in 0.1 M phosphate buffer at 4°C until further processing.

The cortex was sectioned into 1x1x1 mm pieces in 0.1 M sodium cacodylate buffer and pieces were transferred into a 2 ml tube and washed 3 times with 0.1 M cacodylate buffer. The first step of contrast enhancement was performed by incubating the tissue in 1 % OsO_4 in 0.1 M cacodylate buffer for 1 h on ice. After washing three times with dH_2O, kidney tissue was incubated in 1% uranyl acetate in 0.1 M cacodylate buffer on ice for 1 h in the dark to

further enhance the contrast. Remaining uranyl acetate was removed by washing three times with dH_2O. Dehydration of the samples was performed by progressively increasing the ethanol content of the solution the samples were kept in. Tissue was incubated first in 70%, then in 80% ethanol for 20 min each, before ethanol was increased to 96% for 25 min. Following incubations in 100% water free ethanol (2 x 15 min) and 30 min in propylene oxide, embedding was started in 50% Epon/Araldite in propylene oxide two times for 1 h each. Samples were then incubated two times in 100% Epon/Araldite in propylene oxide for 50 min each, before single tissue pieces were transferred into molds and filled with 100% Epon/Araldite. Samples were polymerized for 24 h at 60°C.
Further processing and imaging was performed as described in chapter 2.2.7.

3 RESULTS

3.1 Phenotyping the effect of DFX on proximal tubular cells

3.1.1 DFX induces acute mitochondrial swelling in proximal tubular cells

At the beginning of the study it was necessary to evaluate whether DFX is effective in inducing damage to our in vitro modelling system of the PT, the OK cells. For the first estimation of an effective concentration of DFX, OK cells were treated with DFX in various concentrations, before cell viability was estimated using neutral red assay. This assay is based on the ability of the cell to maintain pH gradients via the production of ATP, which reflects the cell viability. We found a decrease of cell viability after 24 h of DFX treatment in a concentration dependent manner with a half maximal inhibitory concentration IC50 of 246 µM (Figure 12). To further investigate the effects of DFX on PT cells, we chose a concentration of 200 µM that does not cause major cell death in acute treatment. In humans, therapeutic plasma concentrations of DFX ranged from 100-200 µM after daily dosing of 20-30 mg/kg[130].

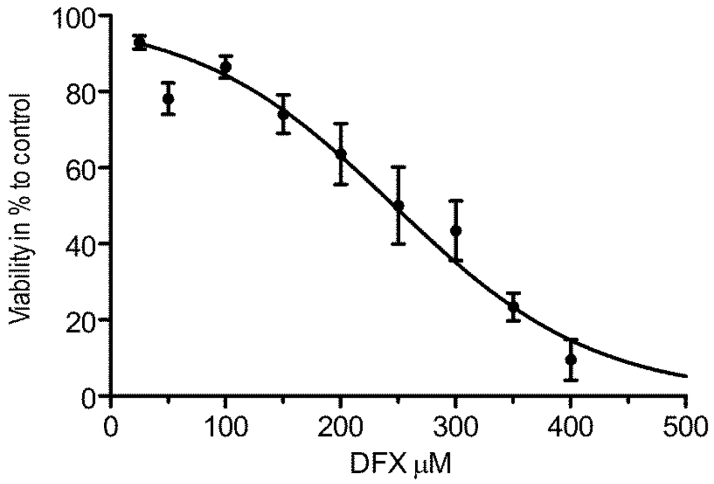

Figure 12: Cell viability measured by Neutral Red Assay in OK cells after 24 h treatment with DFX normalized to control treatment. The IC_{50} was calculated using log (inhibitor) vs. normalized response variable slope analysis at 246 µM.

The next step was to investigate whether DFX induces its nephrotoxicity (Fanconi syndrome) by interfering with mitochondrial structure and function. For this we used live imaging of OK cells stained with the mitochondrial targeted dye Mitotracker deep red. Upon treatment with 200 µM DFX mitochondria rapidly started to swell (5 min), eventually leading to a phenotype of rounded, swollen mitochondria (Figure 13). This was indicative of DFX inducing kidney toxicity via mitochondrial dysfunction.

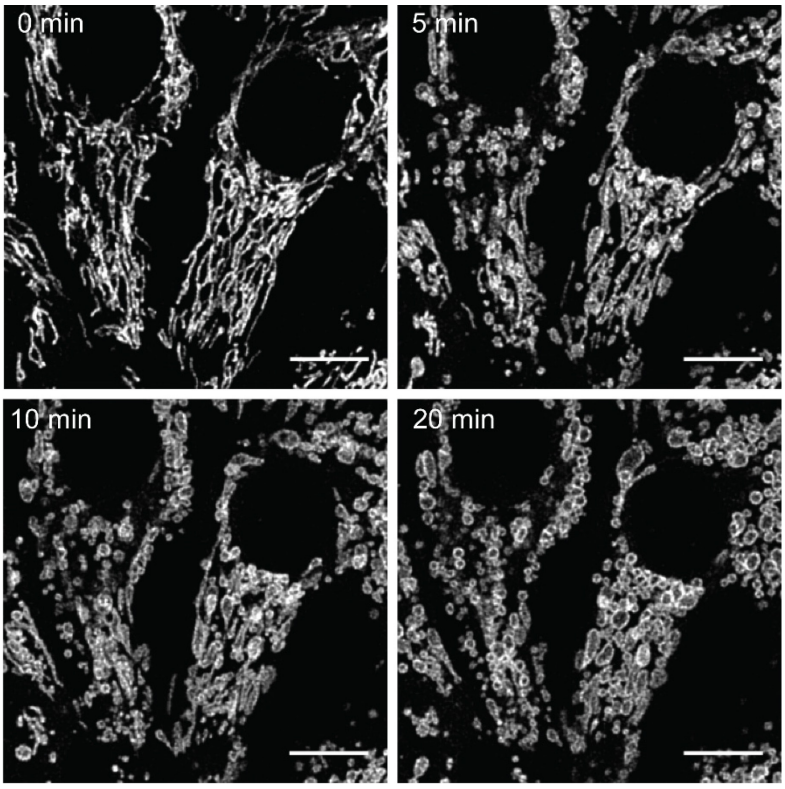

Figure 13: Acute swelling of mitochondria in OK cells upon treatment with 200 µM DFX. Cells had been stained with Mitotracker deep red. Scale = 10 µm.

To investigate mitochondrial energization, OK cells were stained with the mitochondrial membrane potential dependent dye TMRM. This cationic dye accumulates in respiring, and therefore negatively charged, mitochondria. Upon DFX treatment for 30 min, a mitochondrial swelling occurred without a loss of potential (Figure 14). Treatment with solvent control did not induce swelling of mitochondria or a change in potential. In addition, we measured whether changes in density of the mitochondria occur using phase contrast imaging. In control cells mitochondria were hardly distinguishable in the phase contrast, whereas the swollen mitochondria of DFX treated cells appear lighter, signifying a lower matrix density (Figure 14).

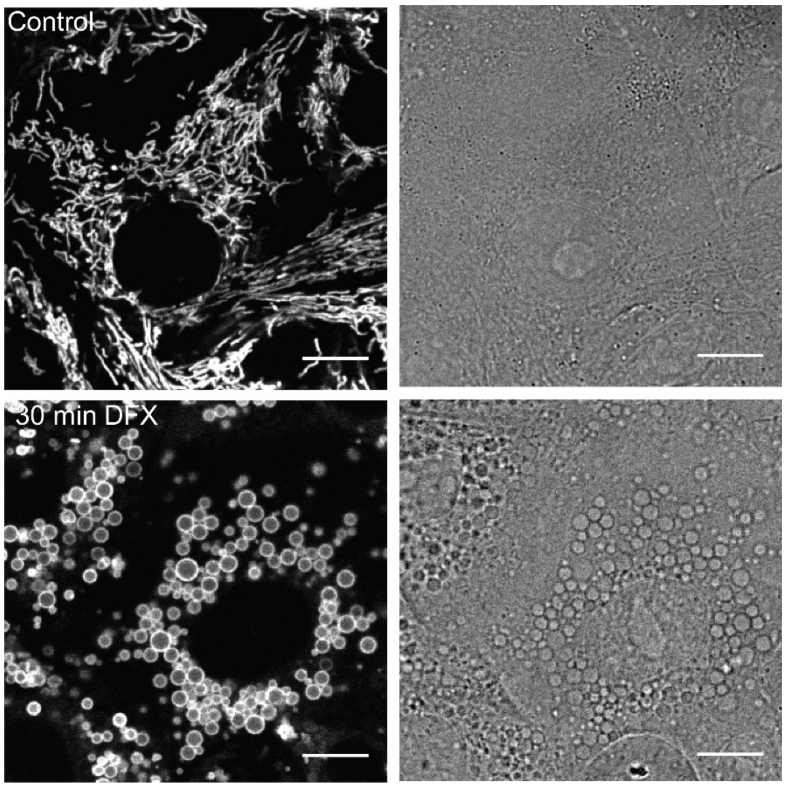

Figure 14: Treatment with 200 µM DFX for 30 min induces mitochondrial swelling without loss of mitochondrial membrane potential detected by staining with TMRM (left). No swelling occurred with control treatment. Only swollen mitochondria were visible due to their lower density in the phase contrast (right). Scale 10 µM.

Further experiments were performed to investigate the effects of DFX-induced mitochondrial swelling on other cellular organelles. Co-imaging of mitochondria with microtubules revealed that swollen mitochondria post DFX displayed less dynamic trafficking than mitochondria in control cells. Microtubuli were observed to be wrapped around swollen mitochondria (Figure 15).

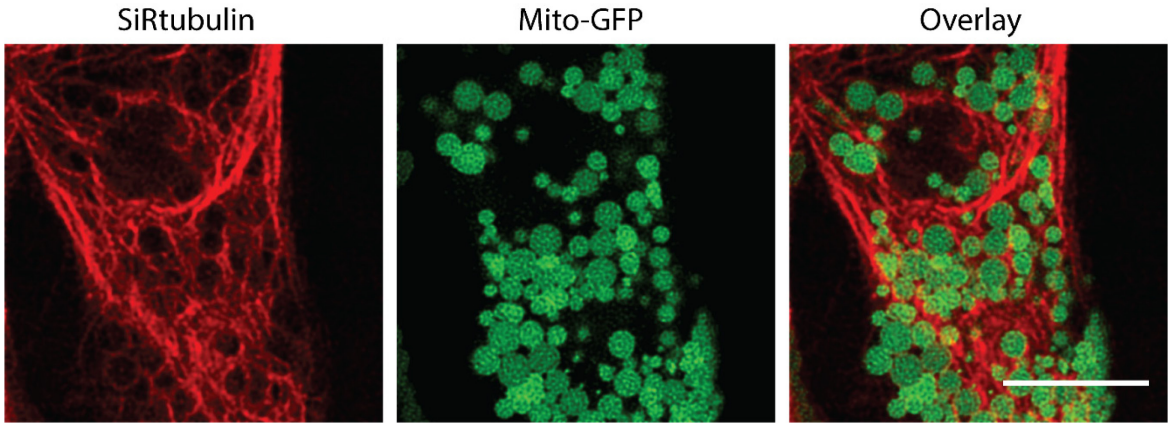

Figure 15: Effect of swollen mitochondria on the microtubular network. OK cells transfected with Bacmam Mito GFP were stained with SiRtubulin (+ Verapamil). Scale = 10 µm.

Similar observations could be made when OK cells were stained for the endoplasmatic reticulum (ER, Figure 16). In DFX treated cells the ER appeared to surround the single, swollen mitochondria.

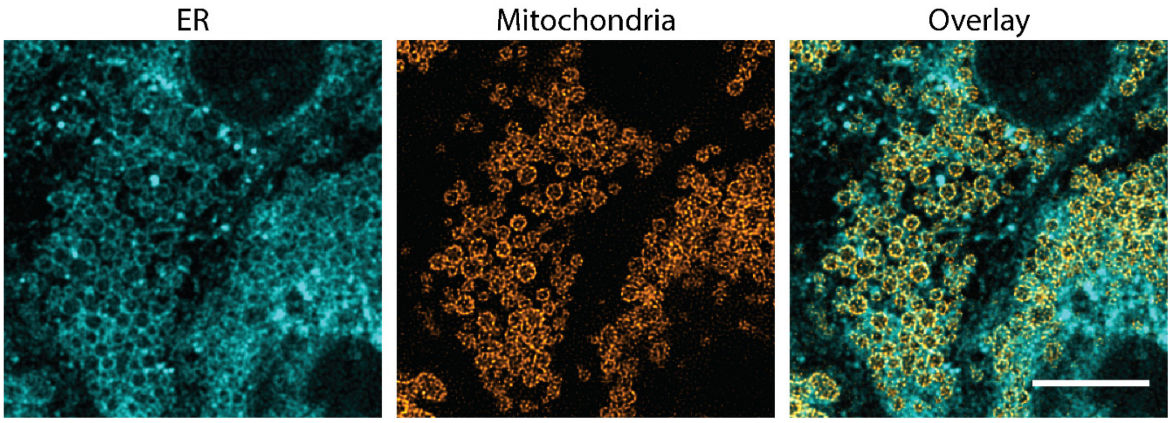

Figure 16: Effect of 200 µM DFX (30 min) on endoplasmic reticulum (ER). OK cells were stained with ER tracker and Mitotracker DR. ER seems to surround single, swollen mitochondria. Scale = 10 µm.

During time series recordings of swollen mitochondria impacted by DFX, we observed that rounded mitochondria formed short-lived (seconds) protrusions (Figure 17). Those protrusions - so called nanotunnels[170] - appear as a response to stress in the cell, caused most likely by the combination of DFX-induced swelling and laser excitation. Their transient existence probably explains why they are rarely observed in fixed specimens. When performing live imaging in control cells we did not observe nanotunnels.

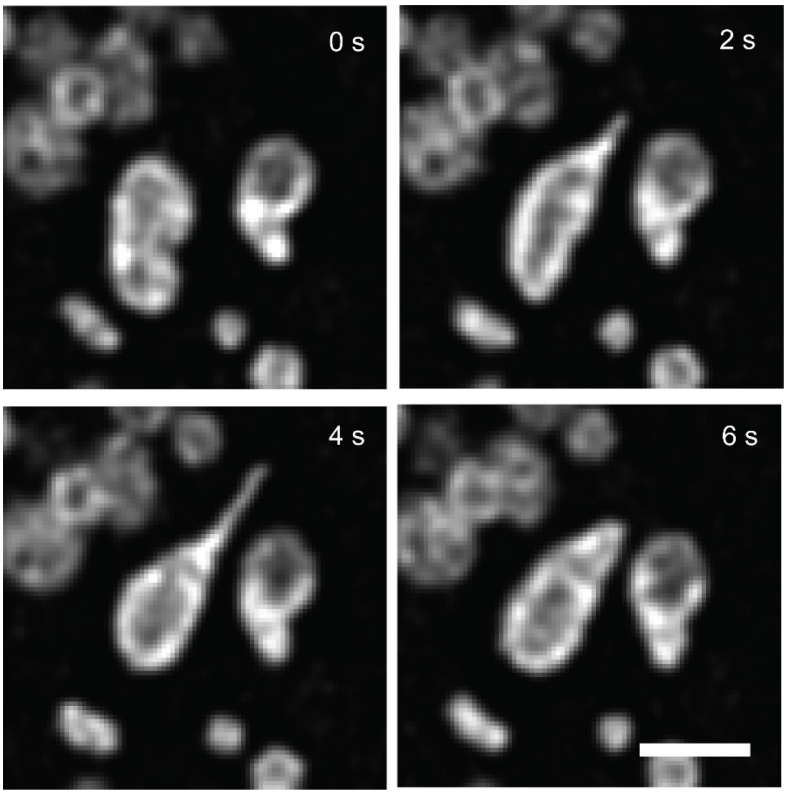

Figure 17: Appearance of transient mitochondrial nanotunnels during fast (1 frame per second) imaging of OK cells stained with TMRM and treated with 200 µM DFX for 25 min. Scale = 2 µm.

After describing the phenotype of DFX by live cell imaging, we wanted to confirm these results in fixed cells to gain an even higher resolution of mitochondrial morphology and to exclude that live imaging interferes with DFX induced toxicity (for example, due to laser toxicity). We utilized an antibody staining for the outer mitochondrial membrane, TOM-20, for the visualization of the mitochondria by STORM. Using this approach, we were able to confirm the swelling of mitochondria, without prior impact of laser damage (Figure 18).

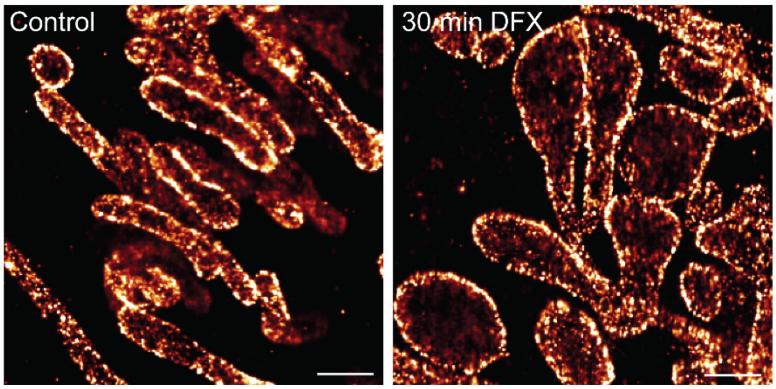

Figure 18: 3D STORM super resolution images of TOM-20 stained mitochondria treated with 200 µM DFX for 30 min and control (left). Mitochondrial swelling is only apparent in DFX-treated sample. Scale = 3 µm. (Imaging and image processing conducted by Dominik Hänni)

To gain insights into the state of the inner mitochondrial membrane, OK cells were fixed by high pressure freezing after treatment with control or DFX. After dehydration and embedding we were able to depict mitochondrial morphology using TEM. In the overview (Figure 19, upper panels) there was already an obvious difference between DFX and control, since DFX mitochondria were visible as light, big, round structures. With greater magnification (Figure 19, lower panels) the difference between the two treatments is even more impressive. In control cells mitochondria had normal cristae and the matrix appeared to be darker than the cytosol, indicative of a high protein density. In DFX treated cells the mitochondria were swollen, cristae were disrupted, and the matrix density was reduced.

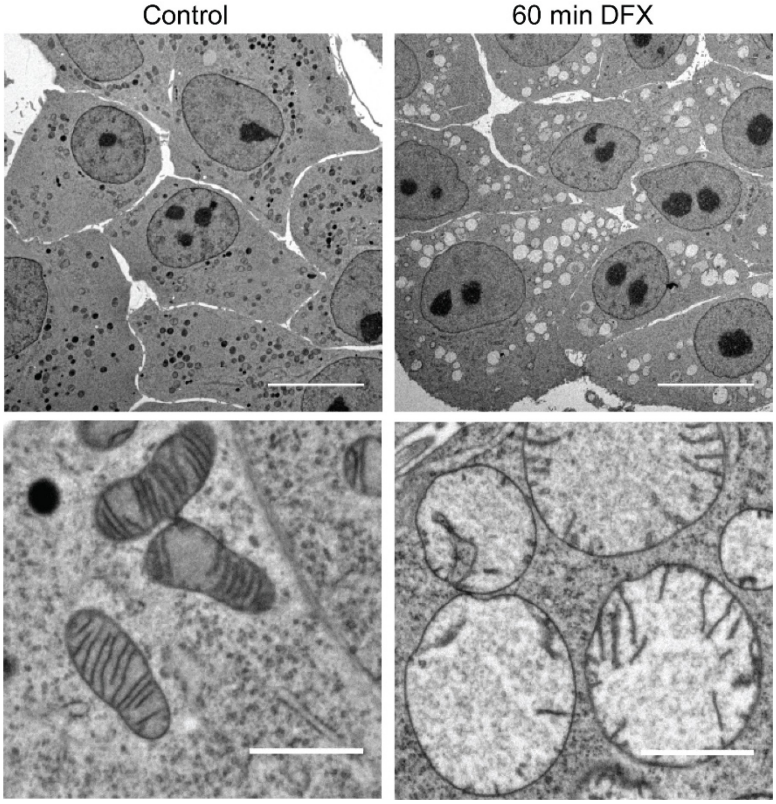

Figure 19: TEM images of high pressure frozen OK cells treated with 200 µM DFX for 60 min and control. Even in low magnification (upper row), swollen mitochondria are detectable as lighter white spots. (Scale 10 µm). With higher magnification it becomes obvious, that upon treatment with DFX the matrix density is decreased, and the inner membrane is pushed towards the outer one. Scale 1 µm.

As a result, we were able to determine - using different methods - that DFX induces toxicity by interfering with mitochondrial morphology, leading to swollen organelles.

3.1.2 Swollen mitochondria are vulnerable to rupture

During recording of fast time series of swollen mitochondria stained with TMRM, the mitochondrial signal seemed to disappear and reappear during the measurement, a phenomenon only rarely occurring in healthy mitochondria.

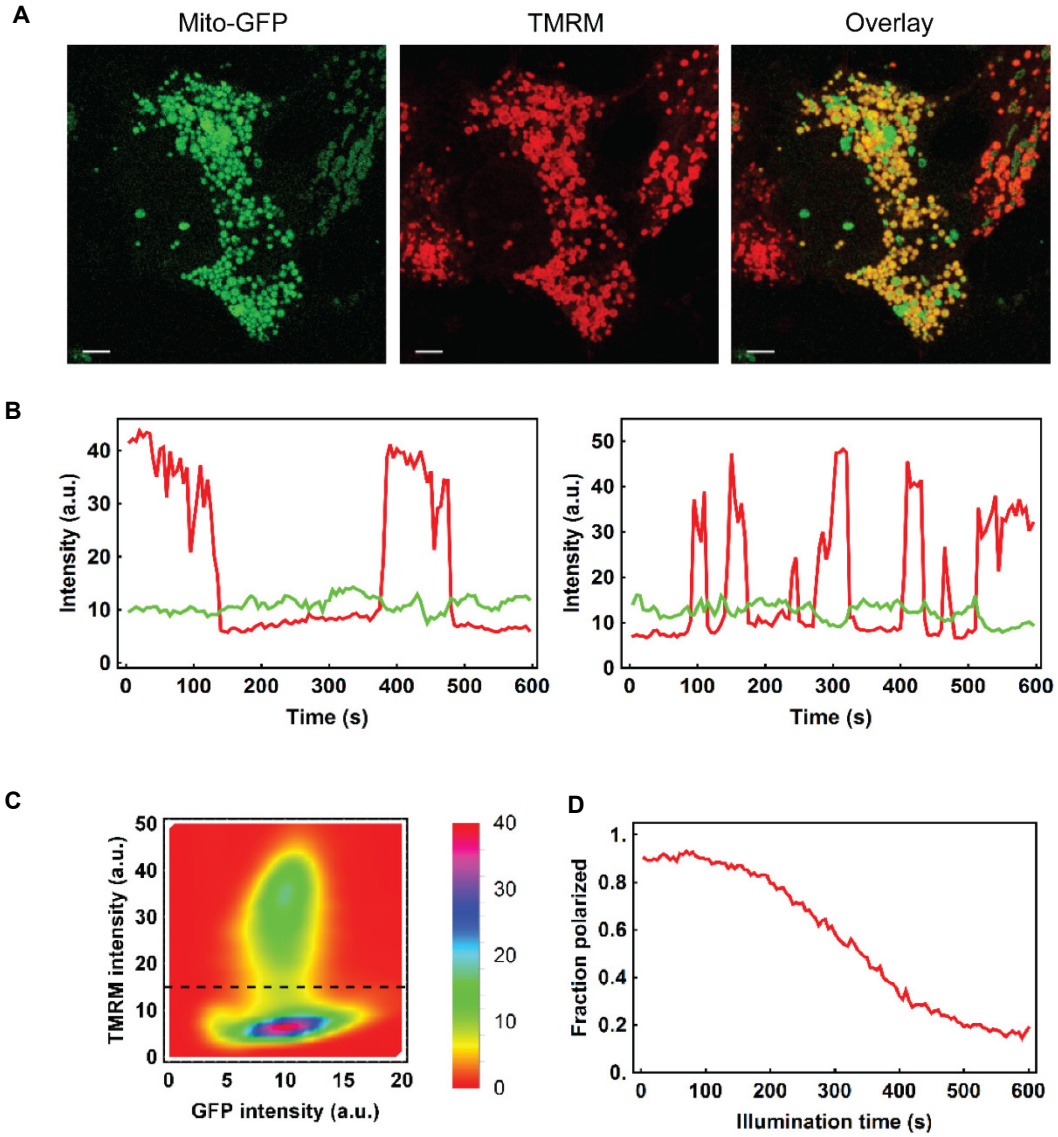

Figure 20: Characterization of mitochondrial flickering post DFX. (A) OK cells expressing CellLight Mitochondria-GFP BacMam 2.0 stained with TMRM for automated tracking of $\Delta\Psi_m$ after a 30 min treatment with 200 µM DFX. Scale = 5 µm. (B) Example of single mitochondria fluorescence trajectories of laser induced blinking post DFX. Mito-GFP intensity (green area) is used for tracking and TMRM intensity (red area) is used as a readout for $\Delta\Psi_m$.(C) Cumulative 2D histogram of Mito-GFP and TMRM signals shows two populations for TMRM but no correlation between Mito-GFP and TMRM indicating that the Mito-GFP signals remain even after the laser induced loss of $\Delta\Psi_m$. The dashed line indicates an intensity threshold of 15 which was used for discriminating between polarized and depolarized mitochondria. (D) Plot of the time evolution of the fraction of polarized mitochondria under a continuous illumination regime.

To investigate this instability, or ”flickering”, of the mitochondrial membrane potential, OK cells were transfected with a mitochondrial targeted GFP (CellLight Mitochondria GFP, BacMam 2.0). This ensured that mitochondria remain detectable with the GFP although the TMRM signal is lost (Figure 20 A) and enabled an automated analysis (performed by Dominik Hänni) of the fluctuations of the TMRM signal. The GFP signal (green trace) was stable during the measurements, whereas the intensity of the TMRM signal (red trace) switched rapidly between two states (Figure 20 B). Summarizing all traces confirmed that mitochondria were either polarized or depolarized (Figure 20 C). During the prolonged observation time it became apparent that mitochondria were more likely to be depolarized during later time points in the measurement (Figure 20 D), suggesting that swollen mitochondria were more vulnerable to laser induced rupture.

Subsequent experiments performed without repetitive laser illumination confirmed that swollen mitochondria post DFX exist in two states – polarized and depolarized (Figure 21) - and eventually lose their potential. The time frame of sustained depolarization, however, was much longer without laser illumination, and the fraction of depolarized mitochondria only started to substantially decline without pre-illumination after 2 hours of DFX treatment (Figure 21). One likely explanation for the loss of potential in swollen mitochondria of DFX treated cells was found during the morphological screening using EM. Some mitochondria were not only swollen, but also showed a ruptured membrane (Figure 21), which most likely occurred due to increased pressure within the mitochondrion, perhaps explaining why it takes some time until loss of potential is detectable without pre-illumination of the mitochondria. The short-term loss of potential probably reflects a higher vulnerability to laser damage due to the swollen state of the mitochondria. Thus, we were able to show that DFX-induced swelling increases the vulnerability of mitochondria to rupture.

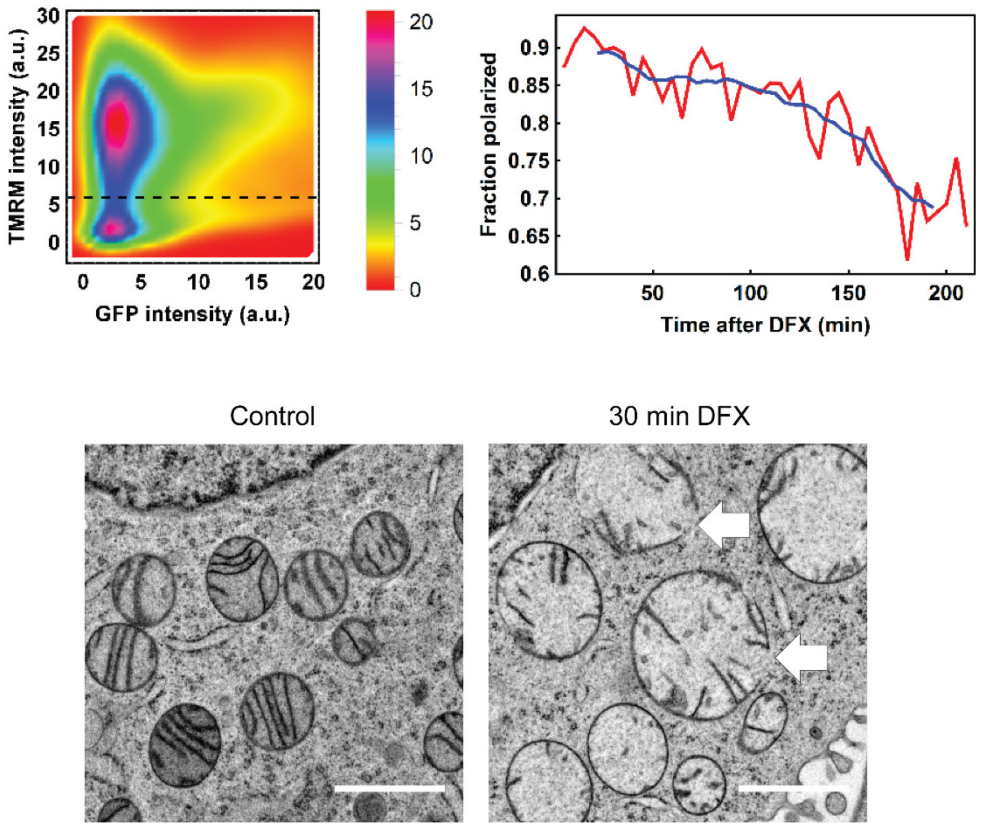

Figure 21: Long term no laser pre-illumination experiments to derive mitochondrial depolarization kinetics in the absence of laser induced effects. The 2D Histogram again shows two populations for the TMRM signal but only one for the Mito-GFP signal. An intensity threshold of 6 (dashed line) was used to derive the time evolution of the fraction of polarized mitochondria. Compared to the continuous illumination experiments, the magnitude of depolarization was significantly lower, and the timescales dramatically extended. A moving average of 40 minutes (blue line) was included to better show the overall trend of spontaneous DFX induced mitochondrial depolarization. TEM of control and DFX (30 min 200 µM) treated cells. Arrows mark ruptures of the outer membrane. Scale = 1 µm.

3.2 Understanding the mechanism of DFX induced toxicity

3.2.1 DFX toxicity is due to an off-target effect

After describing the morphological changes DFX induces, the mechanism of DFX induced toxicity was further investigated.

Since DFX was designed as a drug to bind iron for excretion, the first question to answer was whether DFX induced toxicity is due to the chelation of iron in the cell or due to an off-target effect. As discussed earlier, iron is extremely important for a range of mitochondrial functions. A simple way to investigate this was to compare DFX with other clinically used iron chelators, namely Deferoxamine (DFA) and Deferiprone (DFP). Neither of those iron chelators induced mitochondrial swelling in OK cells, despite the prolongation of the incubation time to 5 h and the addition of pluronic to increase cell permeability and drug uptake (Figure 22).

Therefore, it is more likely that DFX toxicity is rather due to an off-target effect than its ability to chelate iron.

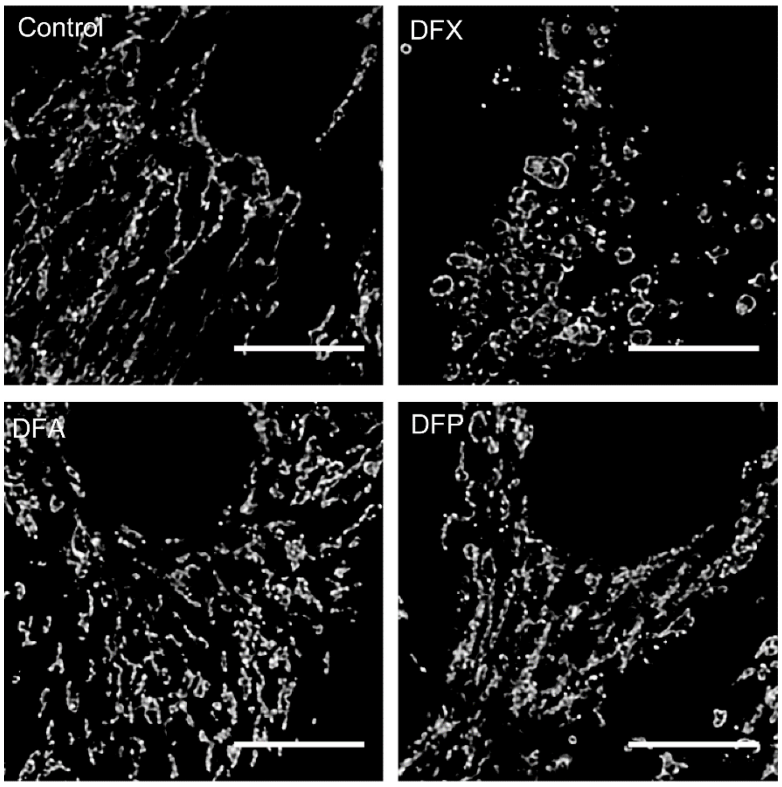

Figure 22: DFX toxicity is due to an off-target effect. Only after treatment with DFX 200 µM 30 min mitochondrial swelling was detectable with TOM-20 staining in OK cells. Other iron chelators (DFA, DFP; 200 µM, 5 h) were not able to recreate the phenotype despite a much longer incubation period. Scale = 10 µm.

3.2.2 DFX does not inhibit respiration or induce oxidative stress

In order to determine the target of DFX induced mitochondrial toxicity, the most commonly suspected pathways of drug induced mitochondrial damage – interference with respiration, induction of oxidative stress and opening of the mPTP - were investigated.

First the effect of DFX on oxidative phosphorylation was investigated using oxygen consumption measurements. After addition of DFX to OK cells, respiration was slightly increased compared to control, but showed no difference when respiration was stimulated with TMPD/Ascorbate, or afterwards blocked by inhibiting complex IV with cyanide (Figure 23, left). Additionally, it was investigated whether DFX could be oxidized by complex IV in a peroxidase mechanism, causing an increase of water inside the mitochondria and explaining the rapid swelling. However, DFX addition to Antimycin A treated cells (to block complex III) did not increase oxygen consumption, disproving the possibility of a functional interaction between DFX and complex IV (Figure 23, right).

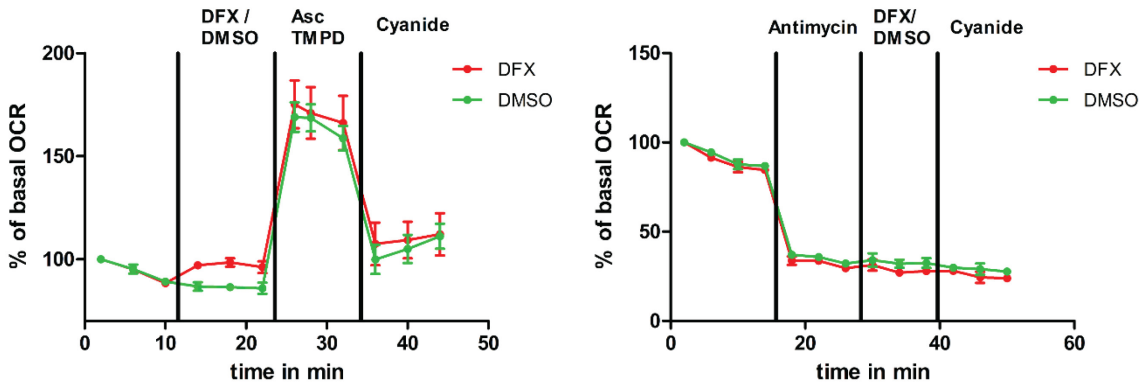

Figure 23: Oxygen consumption in OK cells is not altered in response to DFX. **Left**: After addition of DFX (200 µM), a slight increase in oxygen consumption rate compared to control was observable. After stimulation of respiration by the addition of 500 µM TMPD (2 mM Ascorbate) and blockage of complex IV with 2 mM Cyanide, there was no difference between control and DFX, showing that DFX does not inhibit respiration in OK cells. **Right**: After blocking complex III by adding 2.5 µM Antimycin A, DFX was not able to stimulate respiration and therefore it cannot directly donate electrons to complex IV.

In addition, it was investigated what effect increasing respiratory chain activity has in DFX treated cells by live imaging. In control cells the addition of TMPD/Ascorbate (500 µM, 2 mM), which increases electron supply to cytochrome c, did not alter the energization or morphology of mitochondria (Figure 24). On the other hand, when TMPD/Ascorbate was added to cells that had already been treated with DFX, a rapid, generalized depolarisation occurred. An explanation for this effect is that swollen mitochondria are more vulnerable to

stress that usually would not cause any damage in the cell, similar to the observed increase of laser induced damage in DFX mitochondria.

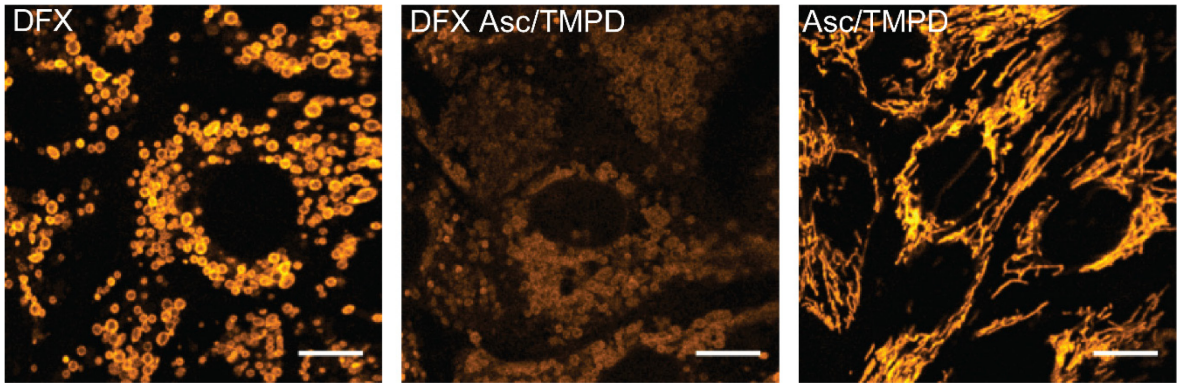

Figure 24: Stimulation of respiration by addition of 500 µM TMPD together with 2 mM Ascorbate after DFX treatment induced a rapid, generalized depolarisation of mitochondria. With DFX alone only mitochondrial swelling was observed, whereas with only TMPD/Ascorbate no changes in morphology or polarisation were detected. Scale = 10 µm.

These observations led to the question whether DFX induced mitochondrial swelling and rupture is mediated via an induction of oxidative stress, leading to lipid peroxidation and degradation of the mitochondrial membranes. At first, it was investigated whether the mitochondrial targeted antioxidant peptide SS-31 could prevent or improve DFX-induced damage. SS-31 was shown previously to reduce ischemic kidney injury and apoptosis[165, 171]. OK cells were pre-incubated with 500 µM SS-31 for 1 h before DFX was added. The antioxidant was neither able to prevent mitochondrial swelling by DFX nor able to reduce the laser induced rupture of mitochondria (observed as flickering of potential) (Figure 25).

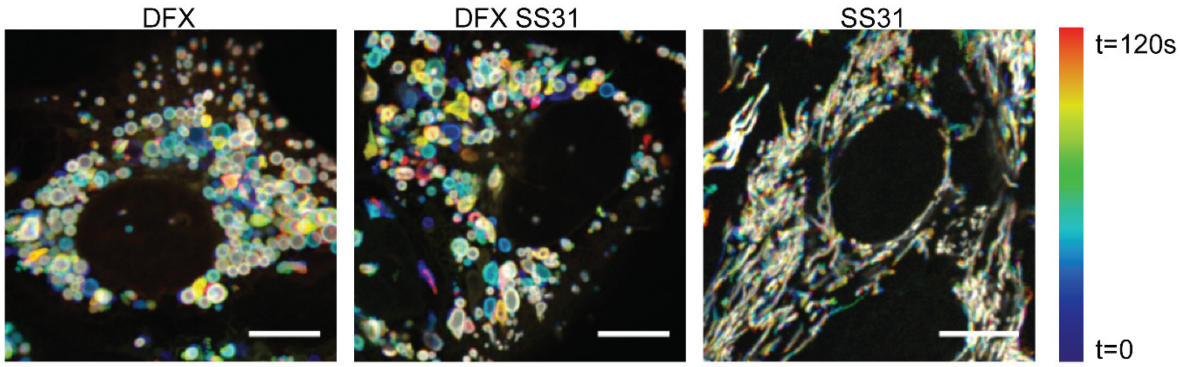

Figure 25: Treatment with the antioxidant SS31 did neither prevent DFX induced swelling nor fluctuations in potential. Shown are color-coded projections of the time series that were recorded with 1 frame per second for 2 min of OK cells stained with TMRM and treated with DFX (200 µM, 34 min), DFX and SS31 (90 min SS-31 500 µM and 31 min DFX) or SS31 only. Each colour represents the time point the mitochondrion had been polarized. If a mitochondrion was polarized during the whole observation time it appears white in this plot. Scale = 10 µm.

Another line of evidence that DFX does not act via the induction of oxidative stress was determined by the measurement of intracellular hydrogen peroxide levels and by the measurement of lipid peroxidation (which could be an explanation for the ruptures in the mitochondrial membrane).

The transfection of OK cells with the hydrogen peroxide sensor Premo enabled the estimation of intracellular peroxide levels by a ratiometric measurement. After a 60 min treatment with DFX the ratio was no different to that of control cells, but the sensor per se did work as an incubation with the positive control (hydrogen peroxide) resulting in a doubling of the measured ratio (Figure 26 A).

Similar observations were made with the lipid peroxidation detecting ratiometric dye Bodipy 581/591 C11. Only in the peroxide treated sample did the ratio increase after a 1 h treatment, whereas no difference to control was visible with DFX (Figure 26 B). Taken together, these findings refute oxidative stress as the reason for DFX induced mitochondrial swelling and rupture.

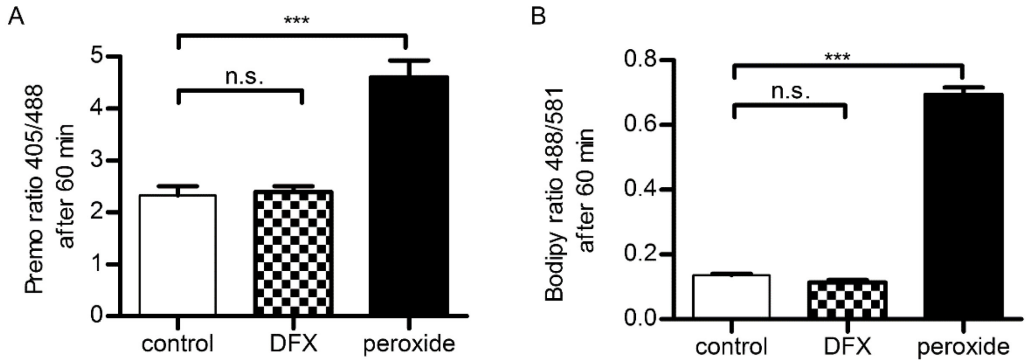

Figure 26: DFX does not induce oxidative stress. (A) Cellular levels of hydrogen peroxide measured using the ratiometric Premo Cellular Hydrogen Peroxide Sensor, Orp1-roGFP after 1 h treatment. For each condition 32 images were analyzed. 1-way ANOVA, posthoc Dunnett's multiple comparison test, *** = $p < 0.0001$ (B) Lipid peroxidation after 1h treatment measured using Bodipy 581/591 C11. For each condition 16 images were analyzed. 1-way ANOVA, posthoc Dunnett's multiple comparison test, *** = $p < 0.0001$.

Cytochrome c has the ability to act as a peroxidase in response to cellular stress, which damages cardiolipin and hence the inner mitochondrial membrane[172, 173]. The antioxidant peptide SS-31 is thought to be protective upon ischemic injury due to an inhibition of peroxidase activity of cytochrome c[166]. DFX might interact with the iron core of cytochrome c, leading to an increase in peroxidase activity and peroxidation of cardiolipin.

The activity of the peroxidase was measured using an Amplex Red assay. Upon addition of cardiolipin the peroxidase activity was increased, as described previously[168]. Treatment with DFX did unexpectedly inhibit the peroxidase activity in a concentration dependent manner (Figure 27).

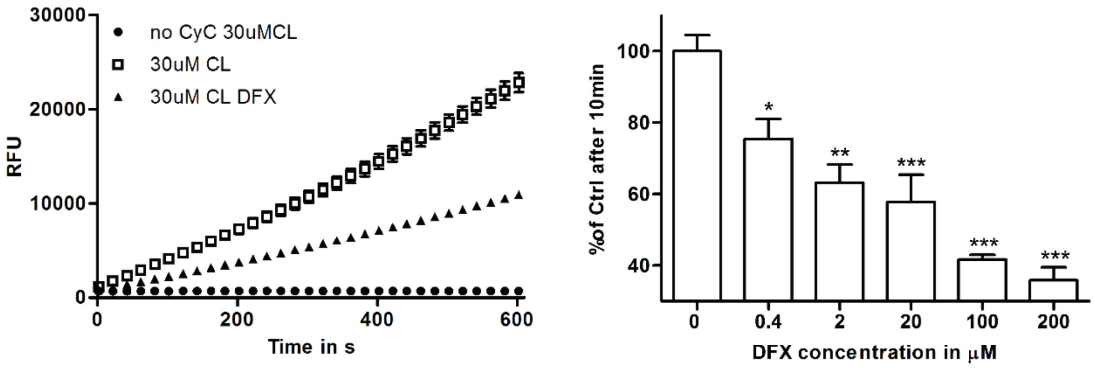

Figure 27: Effects of DFX on cytochrome c (400 nM) peroxidase activity measured by Amplex Red assay. The addition of 30 µM cardiolipin (CL) enhanced peroxidase activity of cytochrome c, which was reduced upon addition of 200 µM DFX. Right: The inhibition of peroxidase activity by DFX was concentration dependent. 1-way ANOVA, posthoc Dunnett's multiple comparison test, *** = $p < 0.0001$; ** = $p < 0.001$; * = $p < 0.05$

3.2.3 DFX induced swelling is independent of the mitochondrial permeability transition pore (mPTP)

Another commonly proclaimed and hotly debated mechanism for mitochondrial toxicity is the opening of the mPTP (see 1.3.3). If DFX was to induce an opening of the pore, a fluctuation in mitochondrial calcium signal would be expected. Mitochondrial membrane potential (Rhodamine 123) and calcium (XRhod) were imaged simultaneously in OK cells that had been treated with DFX. Whilst flickering of the mitochondrial membrane potential was observed as expected, no changes in mitochondrial calcium occurred, indicating that the flickering is not due to the opening of the mPTP (Figure 28).

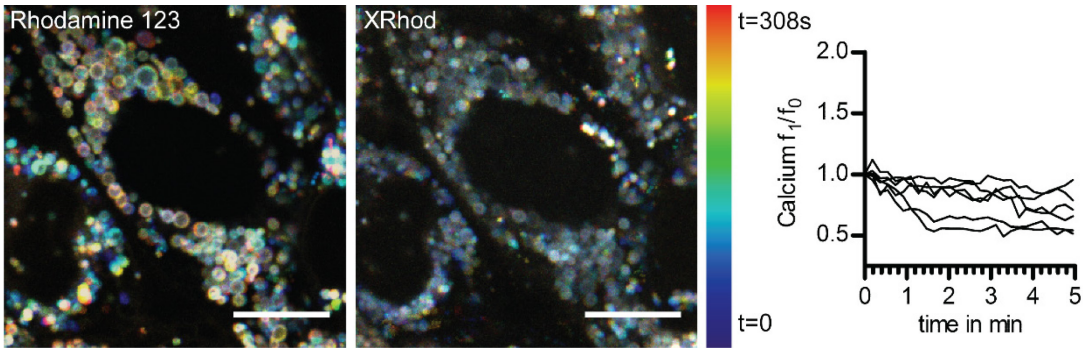

Figure 28: Flickering of mitochondrial membrane potential post DFX is not associated with changes in mitochondrial calcium. Shown are ttemporal color coded images of time series (1 frame per 11 s, 308 s recording) of DFX treated cells stained with Rhodamine 123 (potential) and XRhod (calcium). Scale = 10 µm. **Right**: Plotted traces of different ROIs of XRhod intensity. No flickering was detectable.

Additionally, to the tracking of the calcium signal, pre-treatment of OK cells with an inhibitor of the mPTP, Cyclosporine A, did not prevent mitochondrial swelling or flickering in response to DFX (Figure 29).

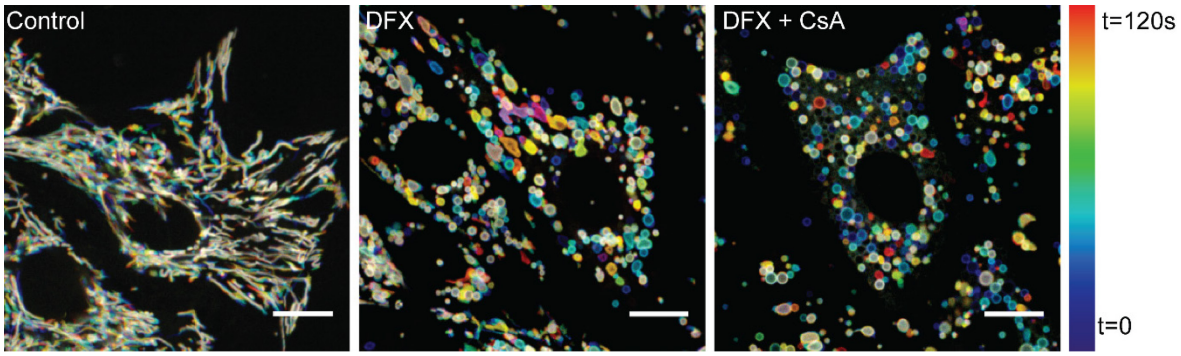

Figure 29 Temporal color coded images of time series (120 frames, 1 frame per s) of cells treated with control, DFX (24 min), or DFX and mPTP inhibitor Cyclosporine A (47 min CsA 1 µm and 32 min DFX 200 µm). Blocking of mPTP did not influence DFX induced swelling and blinking. Scale = 10 µm.

Another method frequently used to observe opening of the mPTP is staining with Calcein-AM[174, 175]. In case of a pore opening, the mitochondrial signal would decrease, since the dye can leave the mitochondrion through the pore. On the contrary, we observed a slight increase in mitochondrial calcein signal together with a decrease of the cytosolic signal, further indicating that the opening of the mPTP is not involved in DFX induced toxicity.

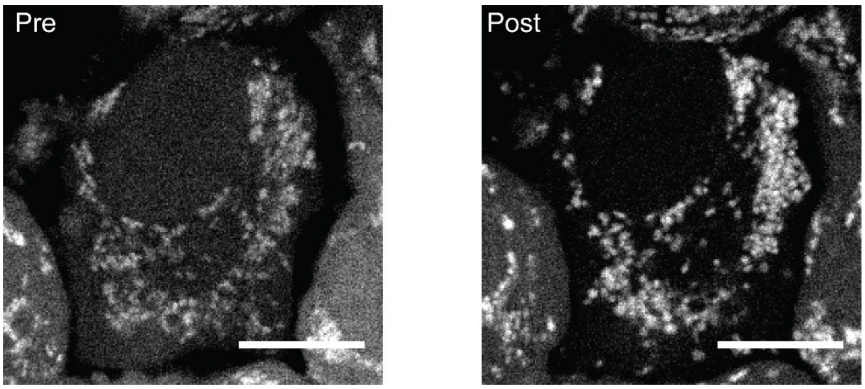

Figure 30: Calcein signal in mitochondria was not decreased post DFX indicating that mPTP is not opening. Scale = 10 µm.

Finally, it was investigated whether DFX induces a release of cytochrome c, a known mechanism of induction of mitochondrial induced apoptosis[176]. Since the available antibodies did not work in OK cells, most likely due to species differences, cytochrome c staining was performed in COS-7 cells (fibroblast kidney cell line). Also, in these cells mitochondria swelled rapidly (10 min) in response to 200 µM DFX, as seen with TOM-20 staining (Figure 31). Cytochrome c was localized within the borders of the outer membrane marked by TOM-20 in both control and DFX treated cells. So DFX did not induce a release of cytochrome c from the mitochondria.

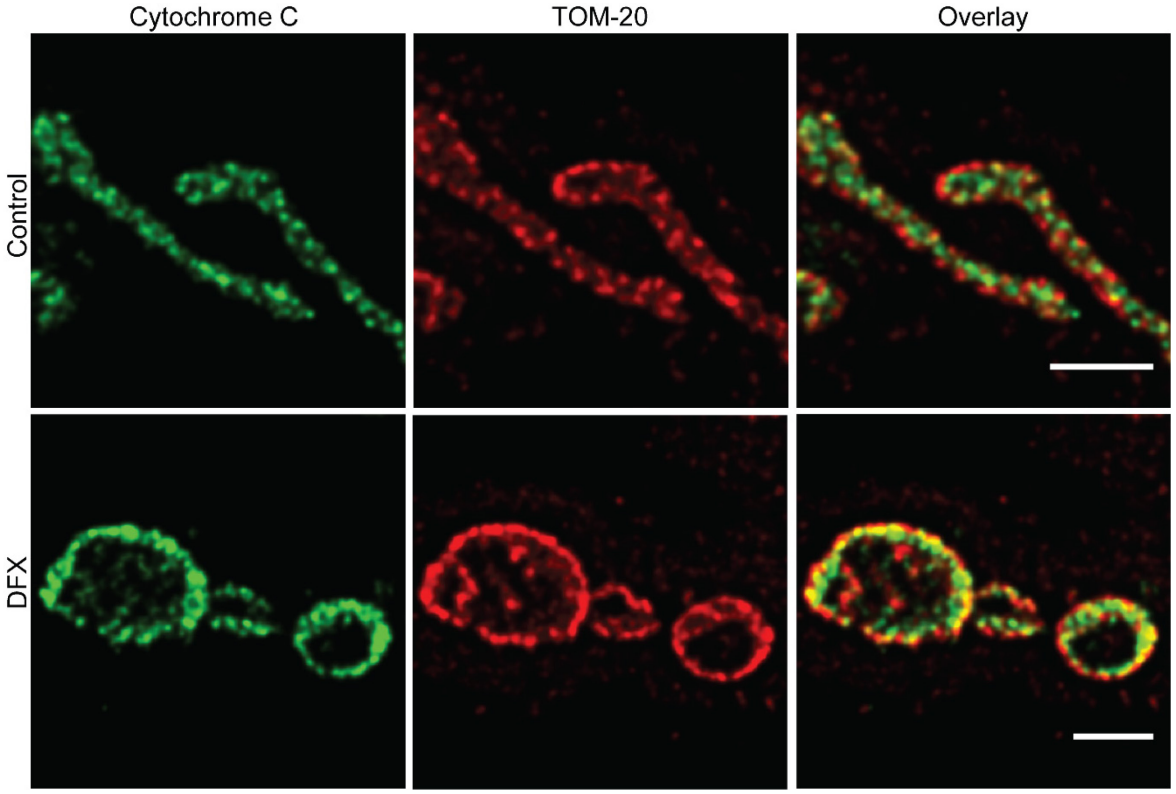

Figure 31: STED images of COS7 cells stained for cytochrome C and TOM-20 after control and 200 µM DFX treatment for 10 min. DFX induced swelling of the mitochondria but no release of cytochrome C. Scale = 1 µm. Staining and imaging performed by Claus Schuh.

Taken together, and using four different experimental strategies – calcium imaging, pharmacological inhibition, dye leakage and cytochrome C release – it was shown that DFX does not induce the opening of the mPTP. Therefore, DFX induced mitochondrial swelling must occur due to a different mechanism.

3.2.4 DFX toxicity is independent of respiratory chain function

Since the classical pathways of mitochondrial toxicity – respiration inhibition, induction of oxidative stress and opening of the mPTP - were not affected by DFX, the next step in understanding the mechanism of DFX toxicity was to further investigate how the rapid swelling might occur mechanistically. Previous studies in isolated mitochondria have suggested that mitochondrial swelling under certain circumstances can occur due to excess water production by the respiration chain[177]. Since the water production is an active process, swelling was inhibited by blockage of respiration in these studies.

To investigate the role of the respiratory chain in DFX induced mitochondrial swelling, OK cells were pre-treated with different respiratory chain inhibitors, before DFX was added, and cells were fixed and stained for TOM-20. Inhibition at different points of respiratory chain (complex III by 2.5 µM antimycin A, complex IV by 2 mM cyanide or complex V/ATP synthase by 10 µg/ml Oligomycin) 10 min prior to DFX treatment did not prevent subsequent

mitochondrial swelling (Figure 32). Additionally, swelling was also independent of mitochondrial polarization, since pre-treatment with the protonophore FCCP (10 µM, 1min) was also not able to prevent the morphological changes in mitochondria.

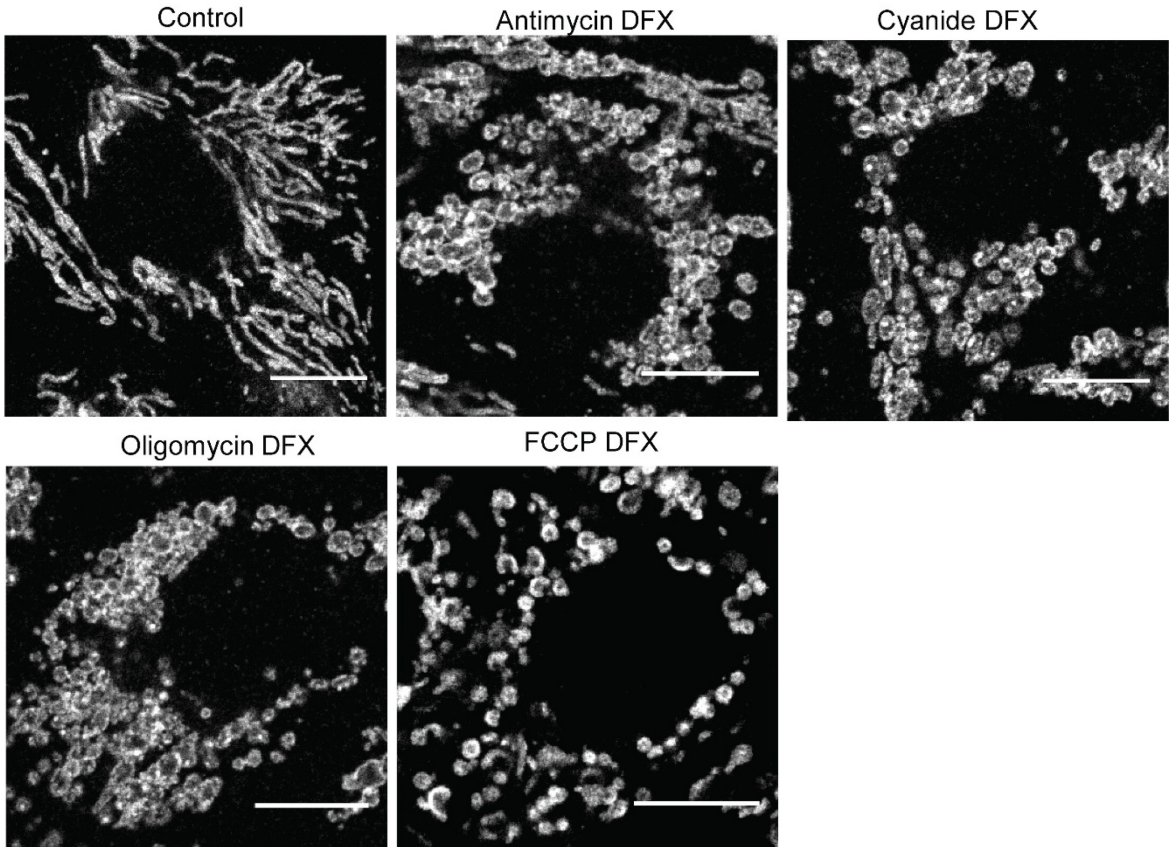

Figure 32: TOM-20 staining in OK cells pre-treated for 10 min with the complex III inhibitor antimycin A (2.5 µM), the complex IV inhibitor cyanide (2 mM), or the ATP synthase inhibitor oligomycin (10 µg/ml), or for 1 minute with the uncoupler FCCP (10 µM) before addition of 200 µM DFX. No interventions with the respiratory chain were sufficient in inhibiting DFX-induced mitochondrial swelling.

3.2.5 DFX induced swelling is not explained by an increased inner membrane permeability

Another way of introducing mitochondrial swelling experimentally is to change the permeability of the inner mitochondrial membrane. The mitochondrial detergent dodecyltriphenylphosphonium (DTPP, used for targeting drugs to mitochondria by its amphiphilic structure, for example, the mitochondrial targeted antioxidant MitoQ[178]), which intercalates into the inner mitochondrial membrane[179] and therefore changes the membrane's properties, caused acute mitochondrial swelling in OK cells, as expected. However, in contrast to DFX, 500 nM DTPP also led to an abrupt depolarization of the mitochondrial membrane potential (Figure 33).

The potassium ionophore Valinomycin renders the inner mitochondrial membrane permeable to K^+, which enables diffusion of K^+ across the concentration gradient into the

mitochondria, and also leads to mitochondrial swelling[180]. Similar to DTPP we could observe mitochondrial swelling and depolarization in OK cells with 10 nM Valinomycin, as expected (Figure 33). Thus, two experimental agents that are known to increase mitochondrial inner membrane permeability could recreate acute mitochondrial swelling similar to DFX, but in both cases, this was associated with rapid dissipation of potential, which was not observed in DFX treated cells.

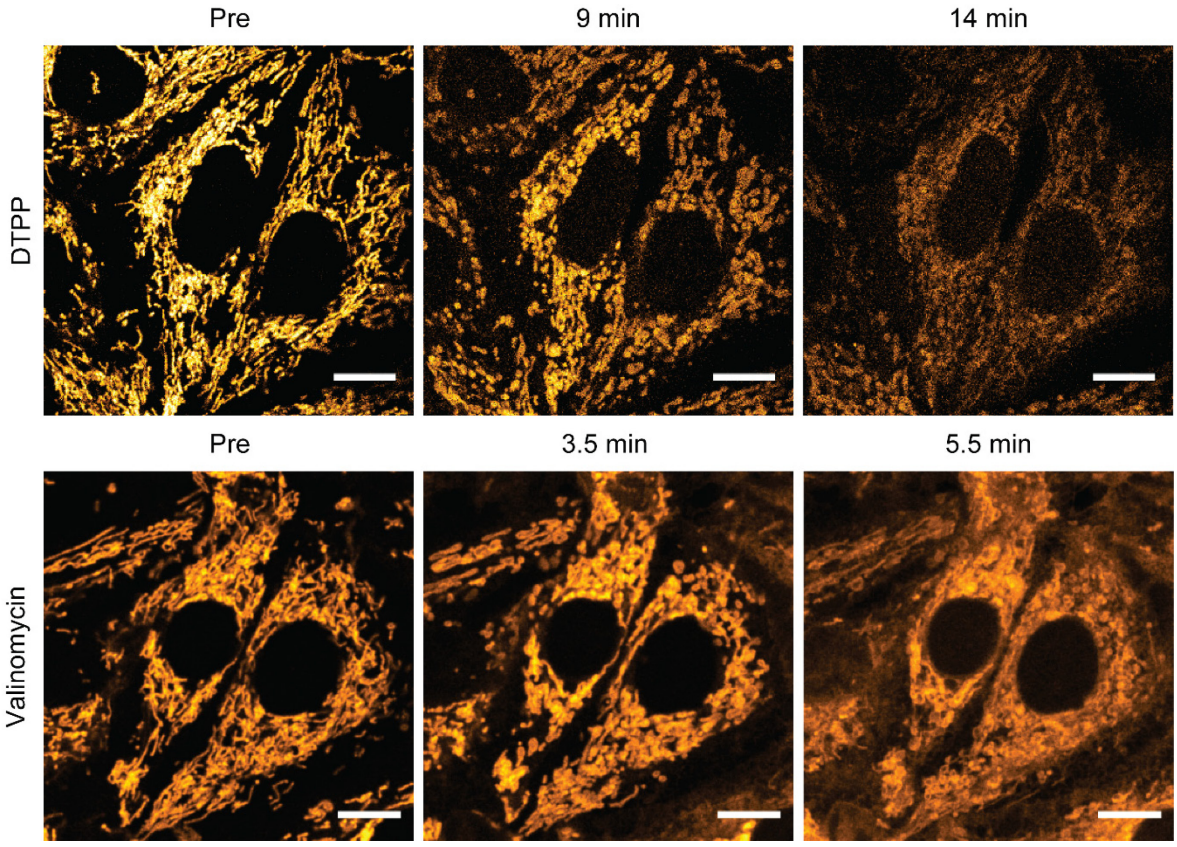

Figure 33: Live confocal imaging of OK cells stained with TMRM revealed that interference with the integrity of the inner mitochondrial membrane by the detergent DTPP (Dodecyltriphenylphosphoniumbromide) or the potassium ionophore Valinomycin induces mitochondrial swelling and depolarization. Scale = 10 µm.

To further investigate whether DFX has an effect on the permeability of the inner mitochondrial membrane, an established artificial liposome model resembling the inner mitochondrial membrane was used[164]. Liposomes containing 20 % cardiolipin were loaded with the fluorescent dye calcein at a sufficiently high concentration (50 mM) to cause self-quenching. When the liposomes rupture they release the dye, leading to a dequenching of calcein signal, and therefore an increase in fluorescence. Additionally, to DFX liposomes were treated with the detergent Triton-X and DTPP (which is known to change the properties of the inner mitochondrial membrane) as positive controls. As expected, both controls did induce the release of calcein, whereas DFX did not, even with a high concentration of 1 mM

(Figure 34). These results provide further evidence that DFX induced mitochondrial swelling is not explained by a direct effect on the permeability of the inner membrane.

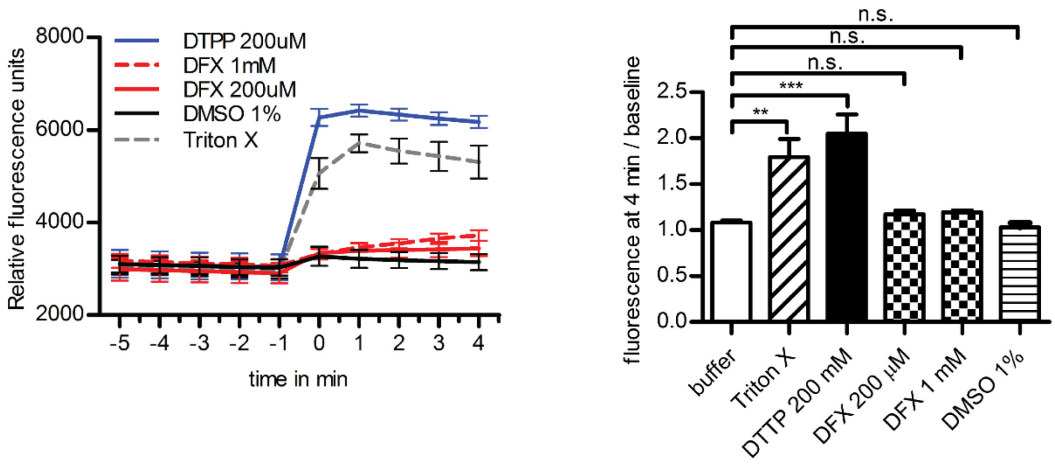

Figure 34: DFX did not increase calcein leakage from liposomes (500 ng/ml) resembling the inner mitochondrial membrane, even at a concentration of 1 mM. In contrast, DTPP and the detergent Triton-X (0.5%) both increased calcein release, indicating a change in membrane permeability. Right: Calcein fluorescence values after 4 minutes of drug addition, normalized to baseline measurements did not show significant increase after DFX. 1-way ANOVA, posthoc Dunnett's multiple comparison test (*** = $p < 0.0002$, ** = $p < 0.01$, n=3).

3.2.6 DFX is not taken up via endocytosis

Since DFX is circulating in the blood mainly bound to plasma proteins like albumin[130] and proteins enter the PT cell via endocytosis[32], it was investigated whether DFX enters the PT cells via endocytosis.

The cytoskeleton as a highway for cellular uptake was disturbed by the blocking of tubulin polymerization using Colchicine[181] (20 µM, 1 h prior to DFX), or by inhibiting actin formation using Cytochalasin D[182] (20 µM, 40 min prior to DFX). Receptor mediated endocytosis was reduced by the inhibition of HMG-CoA with Simvastatin[183] (10 µM, 24 h prior to DFX) and megalin/cubilin mediated endocytosis was blocked by RAP[184] (1 µM, 30 min prior to DFX). None of these attempts to block endocytosis were successful in stopping DFX-induced mitochondrial swelling (Figure 35), suggesting that this pathway is not important for uptake, at least for the free drug.

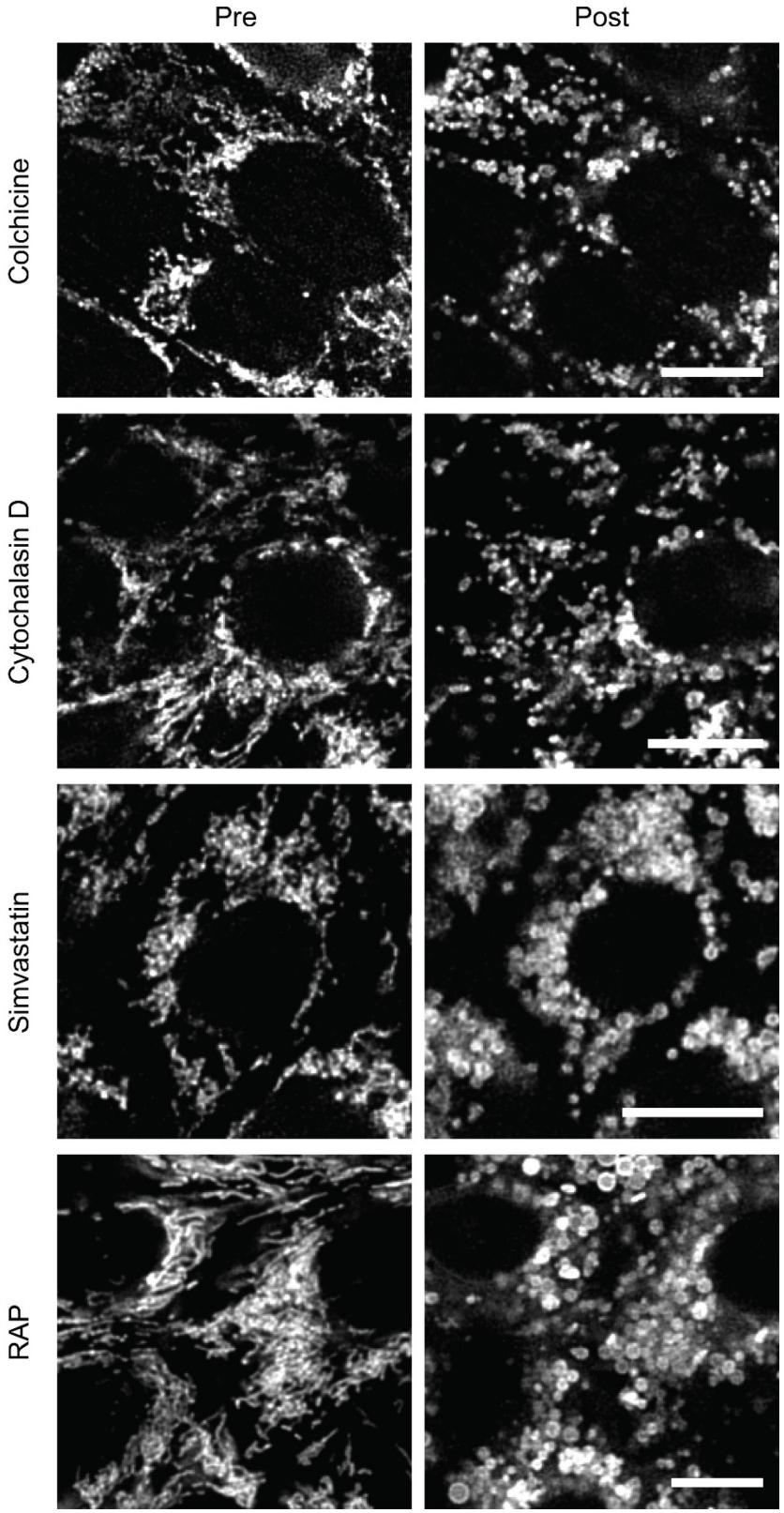

Figure 35: Inhibition of endocytosis did not prevent DFX-induced mitochondrial swelling. OK cells (stained with TMRM) were treated with different blockers before DFX was added. Tubulin polymerization was inhibited by Colchicine (20 µM, 1 h) and actin polymerization by Cytochalasin D (20 µM, 40 min). Receptor mediated endocytosis was reduced by a 24 h incubation with 10 µM Simvastatin prior to the experiment. RAP (1 µM, 30 min) was used to inhibit megalin/cubilin mediated endocytosis. Scale = 10 µm.

3.2.7 DFX induced swelling is preventable and rapidly reversible

The experiments so far suggested that DFX is highly toxic to mitochondria, which raises the question of how it can, in general, be relatively well tolerated in patients. In vivo DFX is highly (99%) bound to albumin in the bloodstream. When similar conditions were created in vitro by a short (5 min) pre-incubation with 200 µM albumin, no mitochondrial swelling in response to DFX was observed, suggesting that only the free drug causes toxicity (Figure 36 A). Indeed, the treatment with DFX and albumin markedly improved cell viability after 24 h, compared to the free drug alone (Figure 36 B).

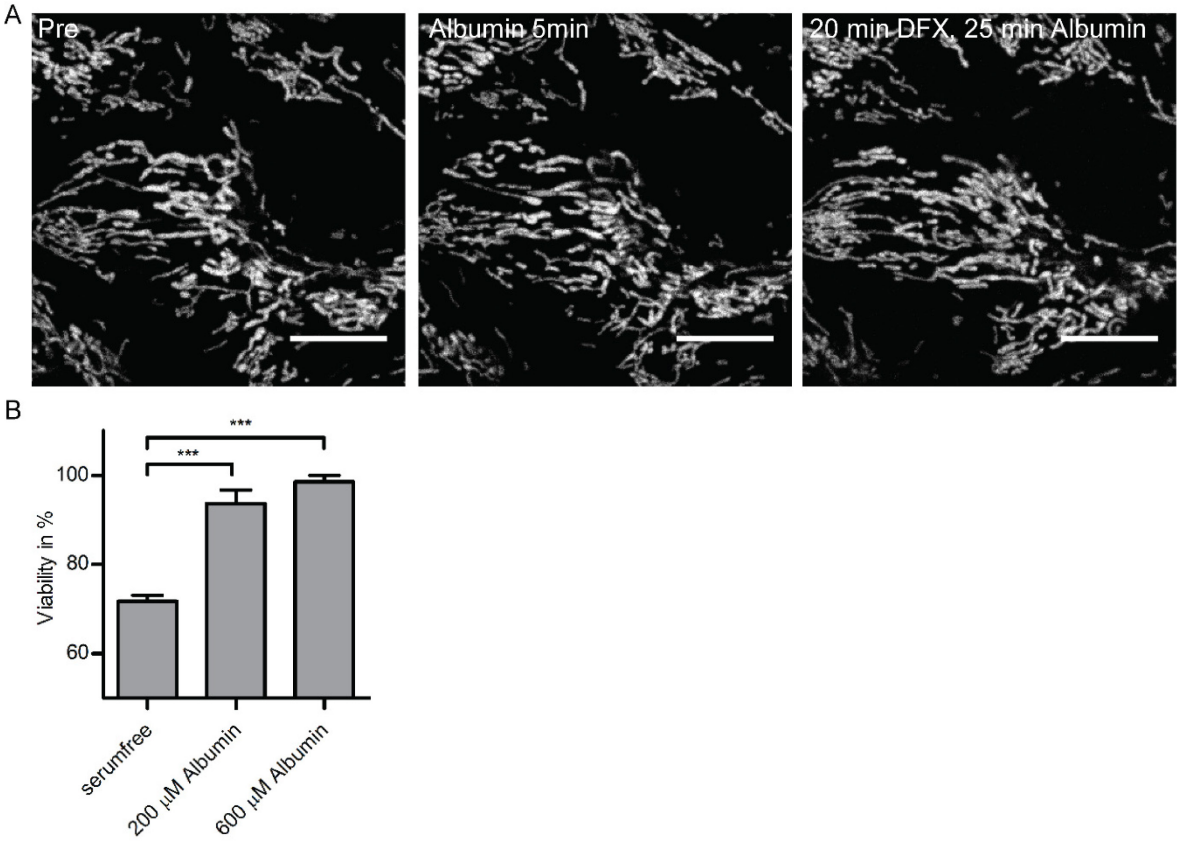

Figure 36: Albumin binding prevents DFX induced toxicity. (A) OK cell stained with TMRM and treated for 5 min with 200 µM albumin, before the addition of 200 µM DFX. No acute swelling of mitochondria was subsequently observed. Scale = 10 µm. (B) Albumin preserves cell viability after DFX (200 µM) treatment for 24 h. 1-way ANOVA, posthoc Dunnett's multiple comparison test (*** = $p < 0.0001$, n=3).

To confirm that only unbound DFX is toxic to PT cells, DFX was pre-bound to its target iron before it was added to OK cells. In the bound form DFX was not able to induce swelling of mitochondria (Figure 37).

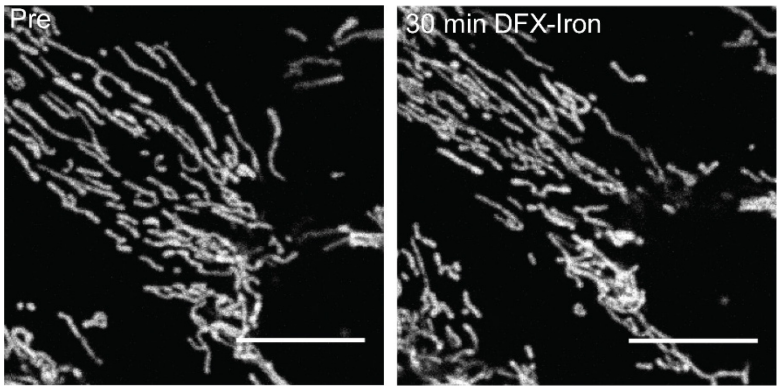

Figure 37: Addition of 200 µM DFX bound to 200 µM iron (III) to TMRM stained OK cells did not induce mitochondrial swelling. Scale = 10 µm.

Iron not only prevented DFX toxicity, but also reversed it. When iron (III) was added to OK cells, that had been treated with 200 µM DFX for 10 min, mitochondria reformed their original elongated shape 10 min after the addition of iron and depolarized mitochondria were observed to re-energize (Figure 38). These observations further confute the existence of mPTP opening, since such a catastrophic event would most likely not be so rapidly reversible.

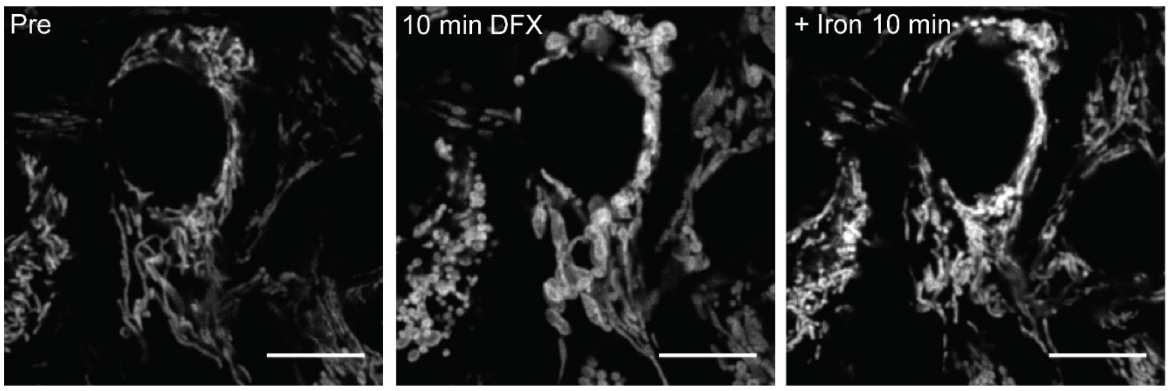

Figure 38: 10 min after DFX (200 µM) treatment, the addition of 200 µM iron (III) reverses mitochondrial swelling within 10 min.

3.2.8 Diclofenac induces a similar phenotype to DFX

DFX is manufactured from the NSAIDs salicylic acid and 4-hydrazinobenzoic acid. In older studies the NSAIDs Diclofenac and salicylic acid were both associated with mitochondrial swelling in kidney and liver, respectively[185, 186]. The building blocks of DFX, salicylic acid (10 mM) and 4-hydrazinobenzoic acid (500 µM), did not cause acute mitochondrial swelling in OK cells in vitro, even when used in higher concentrations than DFX (Figure 39). This is an indication that the complete drug is needed to cause mitochondrial toxicity.

Diclofenac, on the other hand, did cause acute mitochondrial swelling in OK cells while mitochondrial membrane potential was maintained (Figure 39), similar to the effect of DFX.

Both DFX and diclofenac are highly lipophilic, organic weak acids, which might be the common feature in the shared effect of mitochondrial toxicity. Moreover, the fact that a non-iron chelator can recreate the effect of DFX on mitochondria provides further evidence that it is an off target phenomenon.

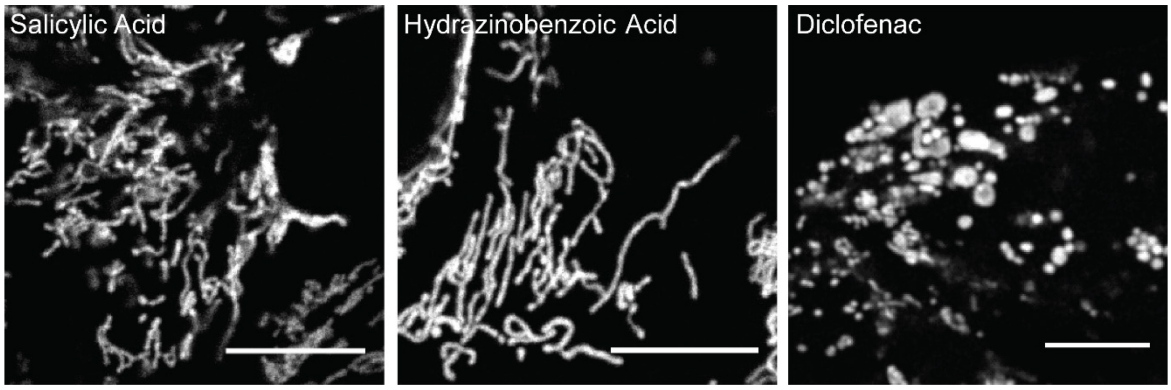

Figure 39: No mitochondrial swelling occurred in response to the starting materials of DFX synthesis, salicylic acid (10 mM, 140 min) or 4-hydrazinobenzoic acid (500 µM, 70 min). The NSAID diclofenac (500 µM, 64 min) on the other hand did induce mitochondrial swelling, whilst the mitochondria remained energized.

3.3 Effect of DFX on kidney cortex

Due to the limitations of an in vitro system, and due to our finding that albumin binding seems to play an important role in DFX mediated nephrotoxicity, the effects of the iron chelator were further evaluated in native kidney tissue and in an in vivo mouse study.

3.3.1 DFX induces mitochondrial swelling in cortical kidney slices

First, to investigate whether DFX causes acute mitochondrial toxicity in native kidney tubules, live imaging experiments were performed in freshly prepared slices of mouse kidney cortex tissue, where the drug could be applied under tightly controlled experimental conditions.

Observations of the cell model could be confirmed as acute mitochondrial swelling was detectable in response to 200 µM DFX (Figure 40). The swollen mitochondria remained polarized although the NAD(P)H signal decreased. Subsequent flickering of mitochondrial potential could also be observed in the slice model. The mitochondrial swelling occurred not only in the PT, but also in the distal tubule and the thick ascending loop of Henle.

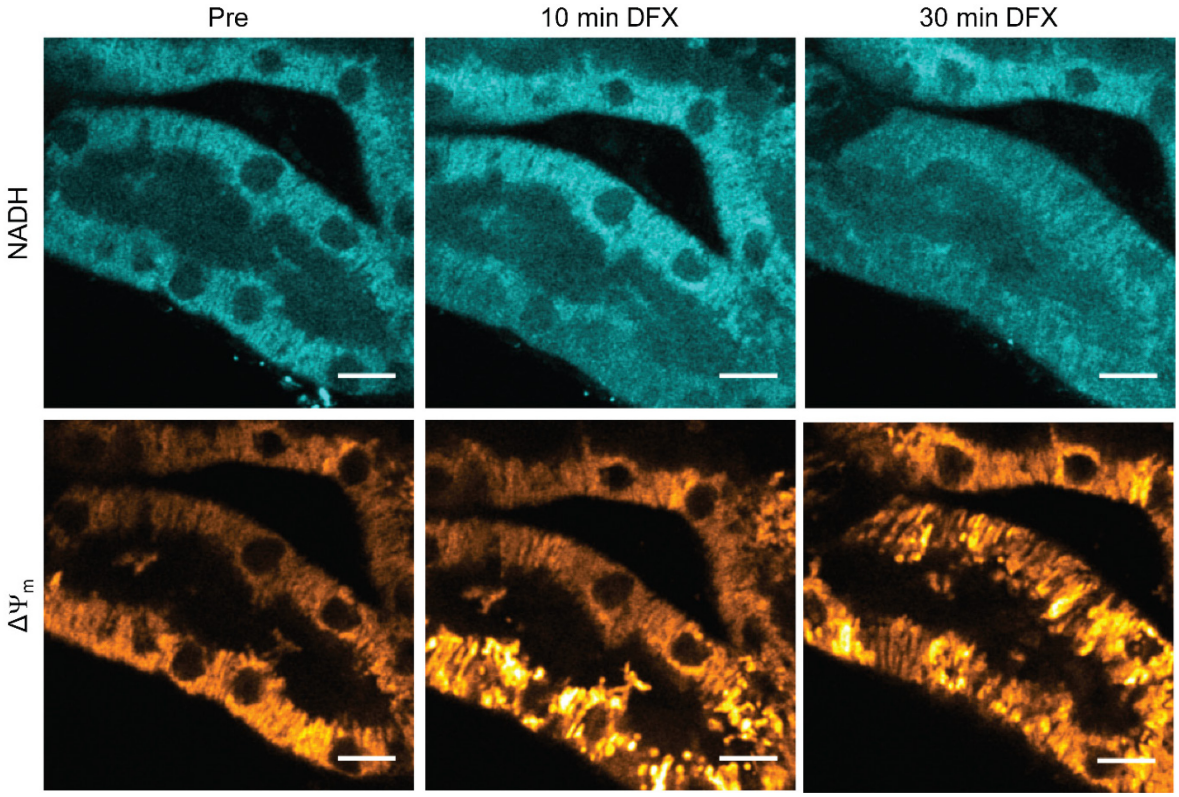

Figure 40: Live multiphoton imaging of cortical kidney slices stained with TMRM showed that 200 µM DFX induced a loss of NAD(P)H signal and rapid mitochondrial swelling without loss of mitochondrial membrane potential ($\Delta\Psi_m$). Scale = 10 µm.

After confirming that DFX induced mitochondrial swelling in kidney slices, the reversibility of toxicity was investigated. The addition of iron did, comparable to the results in OK cells, reverse the swelling within 10 min, after the slice had been treated with 200 µM DFX for 20 min (Figure 41 A). An explanation for the reversibility could be that iron either replenished

cellular iron level, or, alternatively bound free DFX. To distinguish between those two options, DFX exposed kidney slices were treated with copper, which also has an affinity to the chelator DFX. Like iron, copper also reversed the swelling of mitochondria post DFX (Figure 41 B). This further supports our in vitro findings that DFX toxicity is due to an off-target effect.

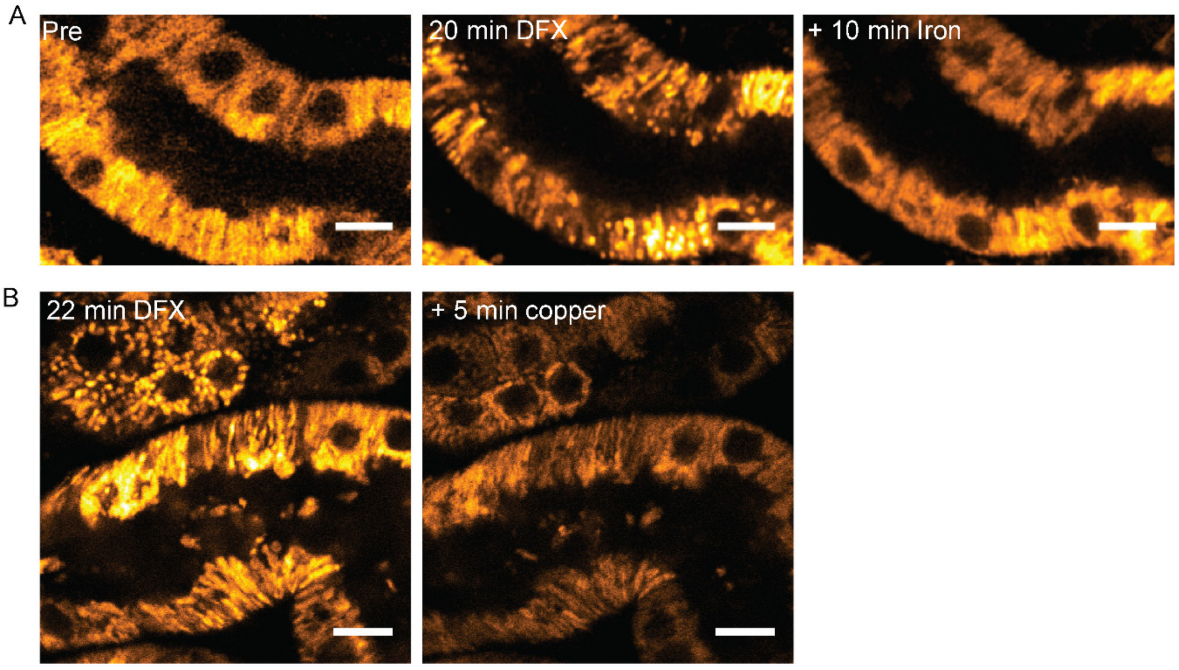

Figure 41: Addition of 200 µM iron (A) or 200 µM copper (B) post DFX reversed mitochondrial swelling in cortical kidney slices. Scale = 10 µm.

Removal of DFX after 30 min incubation had a similar effect as binding of the chelator by ions, since mitochondria regained normal structure as soon as 8 min after drug removal (Figure 42). This suggests that DFX is probably not tightly bound within the cell.

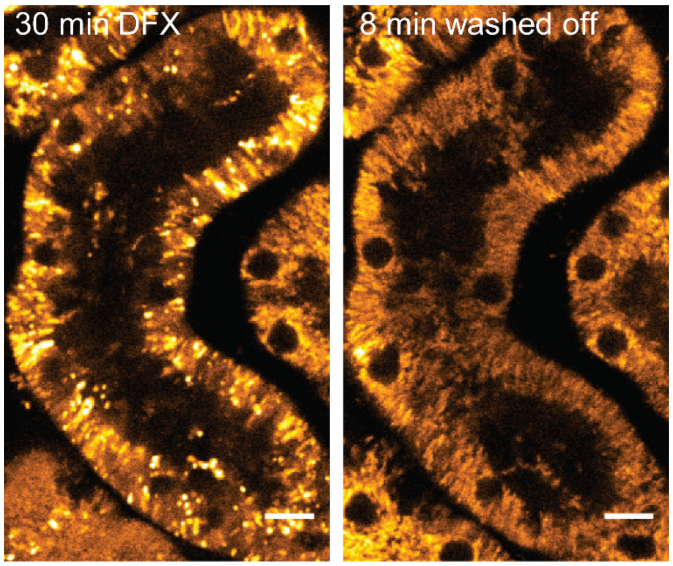

Figure 42: Washing off 200 µM DFX after 30 min also reversed the morphological changes of mitochondria in kidney slices. Scale = 10 µm.

3.3.2 DFX induces mitochondrial swelling in the proximal tubule in vivo

To investigate the effects of DFX in vivo, intravital multiphoton and electron microscopy were used. To model toxicity in humans, mice were given an intraperitoneal daily dose of 100 mg/kg bodyweight DFX for 10 days (similar dosing has been described to induce renal Fanconi syndrome in rats[187]).

Intravital multiphoton microscopy revealed that the damage of DFX is localized to the PT in the kidney. In the blue autofluorescence signal debris was detectable only in the lumen of PTs of DFX treated animals, and not in control treated mice, showing that DFX induced localized cell damage (Figure 43 A).

The mitochondrial TMRM signal was more heterogeneous in DFX mice, compared to control, indicating variations of the mitochondrial membrane potential. Furthermore, individual elongated mitochondria were no longer distinguishable, consistent with mitochondrial swelling (Figure 43 B).

To measure whether protein uptake was affected by DFX (the main criterion for Fanconi syndrome), fluorescently labelled albumin was injected intravenously during live imaging. In control animals, albumin was taken up homogenously across the brush border. In DFX treated animals, albumin was filtered normally, but the uptake of protein into the PT was irregular and protrusions of the apical PT membrane into the lumen were visible (Figure 43 C).

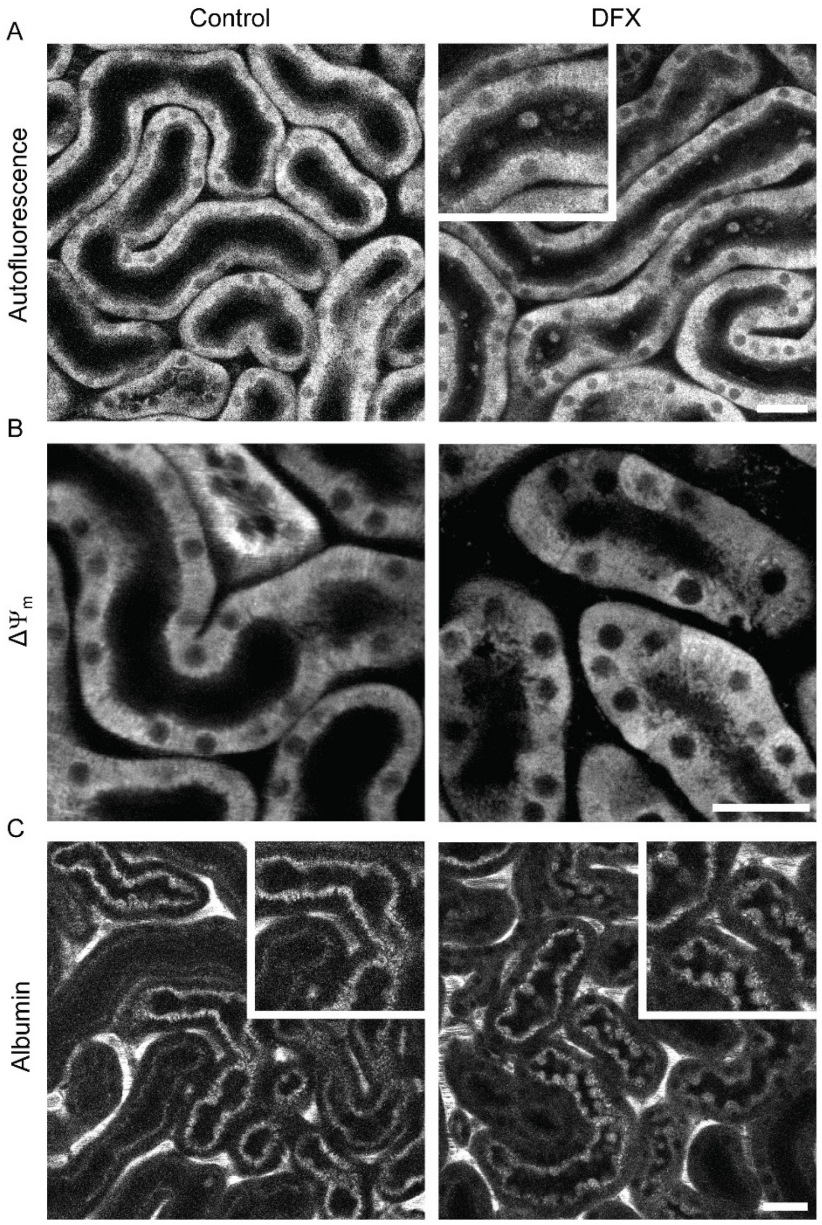

Figure 43: Intravital multiphoton microscopy of DFX treated (100 mg/kg bodyweight i.p., 10 days) mice. (A) Autofluorescence showed luminal cell debris from cell shedding only in DFX treated mice. Scale = 30 µm. (B) Mitochondrial energization, evaluated by TMRM staining, was heterogeneous in DFX animals. Moreover, the normal elongated morphology of mitochondria was no longer observed in DFX animals. Scale = 30 µm. (C) Fluorescently labelled albumin was injected intravenously to visualize protein uptake in the PT. Albumin was filtered in both control and DFX mice, but taken up heterogeneously in DFX animals, resulting in protrusions of the PT membrane into the tubular lumen. Scale = 30 µm. (Experiment performed by Claus Schuh)

To validate the findings that mitochondrial swelling occurs in vivo only in the PT, electron microscopy was performed on kidneys of control and DFX treated animals. Swollen mitochondria, with lower matrix density and cristae pressed towards the outer membrane, were detectable solely in the PT of DFX treated animals. Other tubular segments of DFX treated animals were not affected, and there were no signs of damage in any tubular segments in control mice (Figure 44).

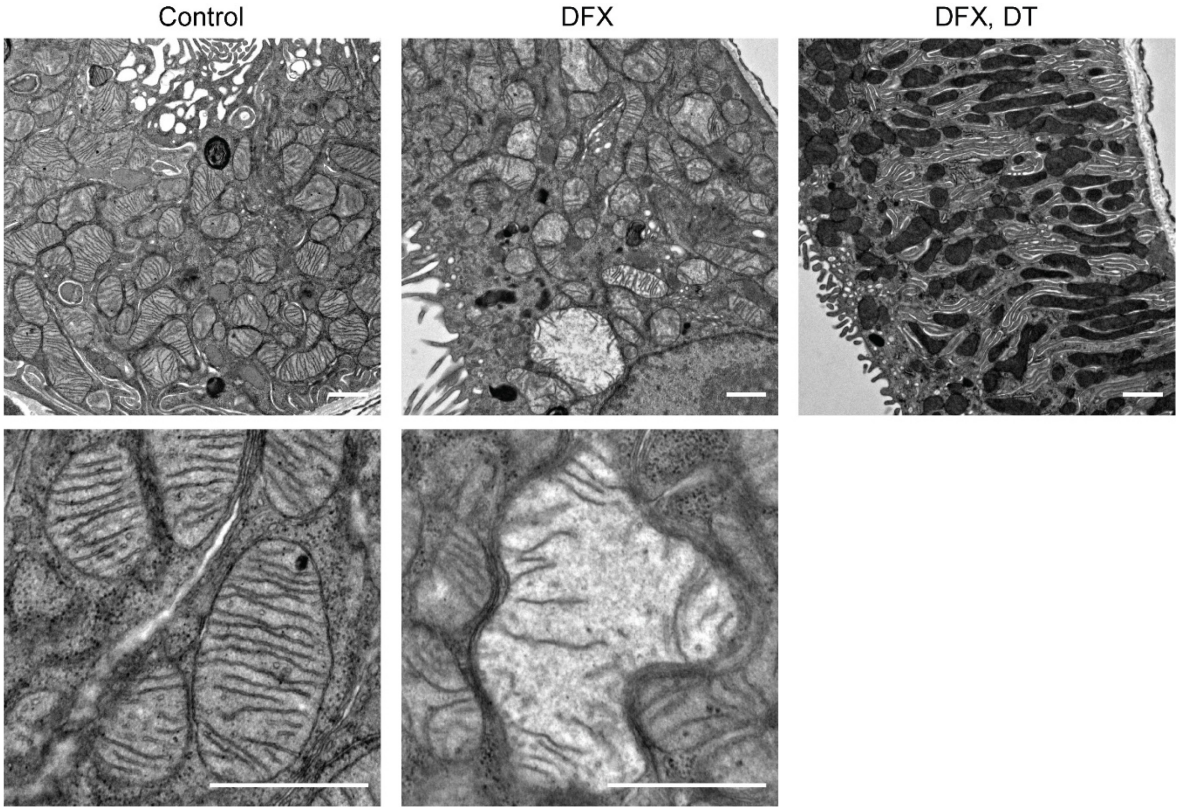

Figure 44: Electron microscopy images of kidneys from control and DFX treated mice. No signs of changes in mitochondrial morphology were observed in control and in the DT of DFX treated animals. In PTs of DFX treated mice swollen mitochondria with decreased matrix density and displaced inner membranes were detected. Scale = 1 µm. Images taken by Susan Ghazi.

4 DISCUSSION

4.1 Limitations of predicting nephrotoxicity of drugs

4.1.1 The problem of drug-induced nephrotoxicity is increasing

Drug toxicity limits the effectiveness of otherwise successful therapies, which is a fundamental problem in fighting diseases. Highly metabolic active organs that also have a great exposure to the blood stream including the circulating drugs/toxins are at high risk of developing toxicity. Liver and kidney are the most commonly affected organs in drug induced injury[188]. Both organs receive, with 20 % to 25 % each, a high amount of the cardiac output, although they only contribute to a low percentage of the whole body weight, resulting - compared to other parts of the body - in a relatively higher concentration of circulating drugs per cell[189]. Especially in the kidney where PT cells not only have to reabsorb solutes after primary filtration, but also have to ensure excretion of molecules, a fine balance can be easily disturbed leading to failure of the renal system and other systems such as acid base homeostasis[1]. Globally, the incidence of AKI has steadily increased, which, in part, is due to the increased number of prescriptions of nephrotoxic drugs[190]. Twenty percent of hospital-acquired AKI is induced by drugs or toxicants[11]. Since AKI is associated with an increased morbidity and mortality[2, 3], it would be beneficial to avoid these problems by developing drugs with decreased nephrotoxic potential. However, the prediction of nephrotoxicity during preclinical drug development is difficult, and the nephrotoxic potential of drugs in development is often underestimated[191, 192].

Nephrotoxicity is only detected late in drug development and accounts for 2 % of drug withdrawal in preclinical studies and 19 % during phase III[192]. One reason for the late detection of adverse effects is the lack of efficient and accurate biomarkers that translate well from preclinical testing to clinical studies[188]. In clinical trials, nephrotoxicity is evaluated by the measurement of blood urea nitrogen and creatinine, both markers that only deviate from normal values when 50 % of the GFR has been lost[193, 194]. Novel biomarkers that have been reported to work in patients, like KIM-1 and NGAL[193, 195], are already upregulated in cultures of rat PT cells, limiting their use for in vitro assays[196, 197]. Other end points that are used as a readout in toxicity testing are cell viability, lactate dehydrogenase (LDH) leakage, GSH depletion or ATP depletion. All of these markers show low sensitivity and high false rates[198]. There is a pressing need to improve the methods for detecting kidney injury already in the state of in vitro assessment of potential nephrotoxic drugs. The use of advances in technology, like metabolomics or high content imaging, could aid in achieving this goal[188]. The use of metabolomics as method for predicting nephrotoxicity is limited due to the elaborate data analysis needed. Imaging, on the other hand, is a relatively straightforward

method to track changes in cellular morphology and physiology, way before markers like cell viability drop[144].

4.1.2 Imaging as a tool for detecting toxicity

Live cell imaging therefore facilitates a general analysis of the intracellular changes enabling the identification of the target organelle of toxicity. Furthermore, mitochondrial dyes, for example, not only provide detailed structural information, but also allow tracking of the health of the organelle. The dye mainly used in this study, TMRM, effectively depicts the energization state of mitochondria via different intensities[199], which is a key marker for mitochondrial activity. Other functional fluorophores can aid to determine levels of oxidative stress with the measurement of lipid peroxidation (Bodipy 488/581[152]) or the levels of intracellular hydrogen peroxide (Premo a transfectable sensor[200]). Arguments that imaging itself causes damage due to laser induced photo-toxicity have to be considered[201]. The laser power used on the sample needed to be adjusted to ensure that no visible alterations - like cell shrinking or bleaching of the dye - occur in a control setting (important when a new dye is established for usage). Additional analysis using immunofluorescent staining of fixed cells, electron microscopy or biochemical assays, can be used to underline and confirm the results obtained from the live cell imaging. Nevertheless, despite these caveats, live cell imaging has the big advantage of showing results in an (almost) self-explanatory, convincing way that is quickly understood.

Although imaging is a powerful tool for investigating cellular changes and metabolism, some limitations can occur due to the model used. In vitro studies on proximal tubular cells are usually relatively straightforward, but performing intravital imaging can result in significant technical challenges[202]. Usage of multiphoton microscopy enables the investigation of the outer cortical region of the kidney in the living mouse, but the imaging depth is limited to around 100 µm[160]. Although mitochondria can't be resolved as clearly as with confocal life imaging of cells, an advantage of the in vivo studies is the possibility for uptake studies to be performed in the living animal by injection of fluorescently labelled molecules of interest, thus providing dual readouts of both transport and metabolism[160]. The gap between in vitro and intravital imaging can be closed by the use of multiphoton microscopy of fresh, cortical kidney slices[203]. Compared to the in vitro situation, cells in kidney slices are arranged in their tubular environment and variations between different segments of the nephron can be investigated. The slices remain metabolically active similar to the situation in the animal – unlike tubular cells in tissue culture that depend more on glycolysis than on oxidative phosphorylation[204, 205]. The disadvantage of the kidney slices is that drugs/solutions can only be applied via diffusion and not via the vasculature. Additionally, tubular cells in the slice are exposed to much higher oxygen concentrations than in vivo, limiting the strength

of the model[206]. For a better and more complete understanding of cellular mechanisms of drug induced nephrotoxicity it is therefore necessary not only to perform traditional cell death assays, but to combine different models (in vitro, kidney slice, in vivo) with imaging techniques such as confocal live imaging, multiphoton microscopy, immunofluorescence, and electron microscopy.

This study mainly used imaging techniques to investigate the mechanisms of drug toxicity induced by the iron chelator DFX. DFX is an important cause of drug induced renal Fanconi syndrome, but the mechanisms of the iron chelator causing this severe side effect were previously unknown[119, 187]. Since iron is a crucial cofactor in electron transport processes in the respiratory chain of the mitochondria[61], and mitochondria are thought to be one of the primary targets of nephrotoxins[95], it was hypothesized that DFX might cause Fanconi syndrome by chelating iron within the mitochondria and therefore altering mitochondrial function.

4.2 DFX causes mitochondrial damage by the induction of swelling

We were able to show in a cell model of the PT (OK cells), that DFX causes rapid (within minutes) mitochondrial swelling, without majorly affecting cell viability, which only decreased to 60 % after one day. Upon DFX treatment mitochondria formed transient protrusions (nanotunnels), before their motility was further decreased. Swollen mitochondria showed a destabilized mitochondrial membrane potential and gradually depolarized over a long period of time.

Therapeutic plasma concentrations of DFX in patients receiving a daily dosing of 20-30 mg/kg range from 100-200 µM[130]. When the rather poor end point of cell viability is used for the evaluation of toxicity[198], DFX (200 µM) only causes some degree of toxicity after one day. The more sensitive readout, live imaging of mitochondrial morphology, revealed that mitochondrial swelling actually occurs within minutes. There are several known causes for mitochondrial swelling: lipid peroxidation[207], opening of the mPTP[208, 209], excess water production[177, 210], opening of a channel[180], or changes in the mitochondrial membrane properties[179], which were all examined in this study. Photoirradiation can induce mitochondrial swelling by increasing levels of ROS, which causes the mPTP to open[211]. This can easily be controlled by minimizing the light exposure of the cells. Imaging under the same conditions without DFX treatment did not induce mitochondrial swelling. Furthermore, mitochondrial swelling was also detectable without prior illumination using

chemically fixed samples for immunofluorescent staining and for electron microscopy. The mitochondrial swelling was therefore a direct effect of DFX, which was previously unknown. The process of mitophagy, the selective degradation of mitochondria by autophagy, starts with the endoplasmic reticulum surrounding the mitochondria to enable the transport towards the lysosomes[212]. During live imaging a change of the endoplasmic reticulum was observed after mitochondria swelled due to DFX. Although this might be indicative of the first step of mitophagy induction, further experiments, such as LC-II staining, are required to confirm that this process is triggered by DFX.

The formation of nanotunnels upon DFX treatment matches the observation of reduced motility in the swollen mitochondria, as nanotunnels arise as a compensatory mechanism to promote mitochondrial communication in stress conditions[170]. They enable the transport of matrix and membrane proteins, and probably also smaller molecules, but are rather difficult to detect, since they are short-lived[213]. Upon DFX induced mitochondrial swelling, stress levels inside the organelle increase, which explains the higher vulnerability to rupture, that was visible by the destabilization of the mitochondrial membrane potential. The observed flickering in the fast-acquired movies, could potentially be explained by small ruptures in the mitochondria (depolarization), which might then be closed by reassembly of the membrane, thus explaining the repolarization. If DFX remains on the mitochondria, the swelling persists and eventually mitochondria will irreversibly rupture, as observed by electron microscopy.

To the best of our knowledge, a phenomenon like this hasn't been described before. It might be unique to DFX, or it might just not have been studied in such a detailed manner or be attributed erroneously to opening of the mPTP.

4.3 DFX is toxic due to an off-target effect

DFX toxicity could be explained by depletion of iron inside the mitochondria in PT cells[119]. However, other iron chelators are not known to cause Fanconi syndrome and even appear to be protective in acute kidney injury and ferroptosis[76, 214]. To clarify whether the toxicity of DFX is indeed due to its effect of chelating iron, or rather due to an off-target effect, the other clinically used iron chelators, DFA and DFP[127], were also tested in our experimental setting to assess their ability to cause mitochondrial swelling. Since both chelators did not induce any changes in mitochondrial morphology or function, we concluded that DFX toxicity is most likely not due to the effect of chelating iron. Although addition of DFX bound to iron did prevent the development of mitochondrial swelling – confirming a recent study[215] - further experiments with other ions like copper showed that this treatment can also prevent toxicity, implying that only the free, unbound DFX induces mitochondrial swelling. This

implies that although having the same target, namely iron, the three clinically used iron chelators are different in their toxicokinetics due to the difference in molecule properties.

4.4 Toxicity of DFX was probably underestimated due to a lack of induction of classical toxicological markers

4.4.1 DFX does not affect respiration

DFX did not acutely inhibit oxygen consumption in mitochondria of OK cells. The iron chelator induced a small acute increase of the oxygen consumption rate but did not alter the capacity for maximal respiration (stimulation of cytochrome c via TMPD/ascorbate). When respiration was stimulated by addition of TMPD/ascorbate, which donates electrons to cytochrome c, an immediate and generalized depolarization was observable in swollen mitochondria post DFX treatment. Furthermore, DFX was not able to restore oxygen consumption when complex III was inhibited.

Some mitochondrial toxins, such as fibrates and thiazolidinediones, undermine mitochondrial function by directly inhibiting the electron transport chain[216, 217] or by uncoupling the electron transport from ATP synthesis[218, 219]. In both cases, the mitochondrial membrane potential can be dissipated[150]. DFX neither inhibits respiration nor dissipates the mitochondrial membrane potential. We could also exclude that DFX acts as an electron donor to cytochrome c in a Fenton type reaction (which would elevate oxidative stress), since addition of DFX after blockage of complex III did neither restore nor increase respiration[220].

PT cells in culture are supposedly more dependent on glycolysis than on oxidative phosphorylation[205], wherefore measurements of oxygen consumption in these cells might be redundant. Nevertheless, OK cells exhibit enough oxidative phosphorylation, maybe due to their endocytic activity[162], to be detected by our sensitive method.

Although DFX is clearly a mitochondrial toxin, the iron chelator did not alter oxidative phosphorylation and therefore induces mitochondrial toxicity via a novel pathway.

4.4.2 Oxidative stress is not induced in response to DFX

DFX did not increase intracellular levels of hydrogen peroxide, nor did it induce lipid peroxidation. Therefore, treatment with the mitochondrial targeted antioxidant SS-31, which stabilizes the connection of cytochrome c and cardiolipin and is known to prevent mitochondrial depolarization during insults such as ischemia[166, 171], did not prevent DFX induced mitochondrial swelling or flickering. Moreover, in an in vitro assay, DFX inhibited the peroxidase activity of cytochrome c rather than enhancing it.

One way of mitochondrial toxins to harm the mitochondria is via induction of oxidative stress. Acetaminophen, doxorubicin and ethanol are examples for imposing oxidative stress via redox cycling or via glutathione depletion, cyp2E1-derived ROS generation or reactive metabolite formation[221-223]. Generated radicals can interfere with electron transport complexes and also induce lipid peroxidation[224]. Although fluctuations in mitochondrial membrane potential has been associated with bursts of oxidative stress[225], we could not find any evidence of induction of ROS after DFX induced mitochondrial damage.

Unexpectedly, we did find evidence of an inhibitory effect of DFX on cytochrome c peroxidase activity. Cytochrome c can act as a peroxidase in response to oxidative stress[172, 173]. The peroxidase activity of cytochrome c damages cardiolipin, which is essential in the organization of the mitochondrial membranes[226]. In its native state cytochrome c is tightly folded, and its peroxidase activity is low, since all coordination positions in its heme iron are occupied[166]. The peroxidase activity increases upon partial unfolding or when the Met80-Iron bond is weakened by interaction with cardiolipin, which we could confirm in our experimental setup[227, 228]. The mitochondrial targeted antioxidant SS-31 prevents cardiolipin from breaking the Met80-Fe coordination in cytochrome c, leading to a decreased peroxidase activity of cytochrome c, which explains the protective effect of SS-31in ischemia induced mitochondrial swelling[166]. Since cytochrome c has an iron core, we hypothesized that DFX might increase peroxidase activity of cytochrome c, but our data showed the opposite.

However, the results of the Amplex Red assay have to be interpreted carefully, since it is measured only with the pure protein and not in a cellular context, where cytochrome c is imbedded in the mitochondrial membrane and is linked to other proteins, which might explain the discrepancy between the oxygen consumption and in vitro assay results. Moreover, if DFX itself acts as a substrate for peroxidases, this could also confound the interpretation of the Amplex Red assay.

4.4.3 Opening of the mPTP cannot be used as an explanation for DFX induced mitochondrial swelling

Numerous studies have explained mitochondrial swelling in pathological states by the opening of the mPTP[208, 209, 229], including AKI due to ischemia-reperfusion injury[165, 230, 231]. However, the composition and the existence of the mPTP remains a topic of numerous discussions[79, 232, 233]. Many studies use cyclosporine A as an inhibitor of the opening of the mPTP, to prove involvement of the pore. However, mitochondrial swelling in response to DFX still occurred, when cyclosporine A was present. The usage of cyclosporine A as proof for mPTP opening has to be taken with caution, since the drug has pleiotropic effects and failed so far to be successful in clinical studies[234].

Studies on mitochondrial swelling are typically performed reading the absorbance of isolated mitochondria at 540 nm, a method that has several drawbacks[235]. First, changes in light absorbance may not always reflect changes in matrix volume. Second, mitochondria are damaged during the isolation process and it is therefore not guaranteed that the complex architecture of the organelle remains stable. Usually no control measurements are made to prove that the mitochondria are still energized. Finally, no information can be obtained about mitochondrial behaviour in their native environment[236].

Other assays of mPTP opening in intact cells include the measurement of matrix calcium, release of the dye calcein out of the mitochondria, and release of cytochrome c (also used as an indicator of induction of apoptosis). After DFX treatment, no mPTP opening specific phenomenon was observable, showing that DFX induced mitochondrial swelling is most likely mediated via a new, unknown pathway.

Before Haworth and Hunter described the mPTP in 1979[237], which was henceforth often used as reason for mitochondrial swelling, the abnormal production of water during oxidative phosphorylation was used as an explanation, since inhibitors of the respiratory chain could prevent the swelling[177, 210]. Since mitochondrial swelling post DFX occurs in the absence of depolarization, a plausible rationale could be the excess production of water that does not interfere with voltage gradients. However, inhibition of respiratory chain activity did not influence DFX induced mitochondrial swelling. Nevertheless, it remains possible that an acute increase in water content within the mitochondrial matrix could explain why mitochondria remain polarized when swollen and why they appear less dense in the electron microscopic study.

Opening of the mPTP is often used as a reason for mitochondrial swelling[208], without full experimental proof. It should be considered that more than one experiment has to be conducted to convincingly explain mitochondrial toxicity by opening of the mPTP.

4.4.4 DFX might affect mitochondrial membrane properties

A change in the properties of the inner mitochondrial membrane induced by DFX could facilitate the entry of water and electrolytes into the mitochondrial matrix, thus explaining acute swelling. However, when the permeability for potassium was changed by treatment with Valinomycin[180], a potassium ionophore, mitochondria did not remain polarized (unlike DFX). Similar observations were also made when OK cells were treated with DTPP, which integrates into the inner mitochondrial membrane and changes its properties[179]. Also, in an artificial liposome model resembling the features of the inner mitochondrial membrane, a direct effect of DFX on the membrane permeability was not observed. Nevertheless, an interaction with the bio-physical properties of the membrane could still be an explanation for DFX toxicity, since the chosen assay enabled us to only detect ruptures of the lipid

membrane, and not changes in fluidity, which would have to be measured using a lipid bilayer with single labelled lipids, allowing an analysis of fluidity. The change in fluidity might then allow the entry of water, without causing a depolarization of the voltage gradient.

4.4.5 NSAIDs might induce kidney toxicity via a similar pathway

The NSAID diclofenac, like DFX, induced mitochondrial swelling whilst the mitochondrial membrane potential was maintained, disproving the opening of the mPTP.
While mitochondrial swelling upon NSAIDs was described, it was previously explained by the opening of the mPTP[115, 116, 238]. However, as discussed above, studies often attribute mitochondrial swelling to mPTP opening with insufficient hard evidence. It might be that both drugs share a previously unknown mechanism of toxicity, which could be explained by biochemical similarities. Both drugs, for example, are lipophilic and weak acids which might preferentially lead to a mitochondrial accumulation. However, this will need to be further investigated in future studies.

4.5 DFX toxicity is localized in the PT due to its uptake mechanism

The hypothesis of DFX directly interfering with the mitochondrial membrane could also be the explanation of why DFX induced swelling is preventable and rapidly reversible. Only the unbound drug appears to integrate (or interact) with the inner membrane, since the addition of iron prevents or reverses the phenomenon. The interaction of DFX with the membrane is therefore presumably weaker than an actual binding of the chelator to its target iron. Binding of DFX to albumin or copper and even just washing off the drug rapidly leads to reversibility of mitochondrial swelling, additional proof of a weak interaction of DFX with the inner membrane.
One major question remaining from this study is how a drug, which induces such drastic adverse changes in mitochondrial morphology in vitro, does not cause generalized, instant damage to patients? Moreover, why is toxicity localized specifically to the PT? DFX induced swelling in other non-PT cell lines (COS-7 and mDCT). In addition, mitochondrial changes in the kidney slice were also observed in the distal tubule and the thick ascending loop of Henle. However, the specific localization of the damage to the PT was only detected in vivo. Since only the free drug causes toxicity in the cell model, the PT is presumably the specific site where DFX appears unbound. In the bloodstream, DFX is 99 % bound to albumin, preventing its acute toxic effect. Albumin is partially filtered by glomeruli[239, 240] and is taken up by the early PT via receptor mediated endocytosis[160, 241]. Either DFX enters the cell bound to albumin, where it is then dissociated (for example by acidification in the eno-lysosomal system[43]) or DFX is separated during filtration and occurs in low amounts as

unbound drug in the primary urine, where it can freely enter the cell (as blocking endocytosis in the OK cell model did not prevent toxicity of the free drug). The accumulation of DFX in the PT and little urinary excretion of the drug was already discovered in pharmacokinetic studies[119, 242]. Studies in intestinal Caco-2 cell monolayers suggested that DFX is most likely a substrate for the multidrug-resistance-associated protein (MRP2) or with a higher affinity for the breast cancer-resistant protein BCRP, which could be confirmed in purified membrane vesicles[130]. In contrast, no transport by MDR1 (P-glycoprotein) was observed. Furthermore, experiments in Xenopus laevis oocytes did not show an involvement of organic anion-transporting polypeptide 1 OATP1A2, liver-specific organic anion transporters OATP1B1 and OATP1B3 or the human organic cation transporter OCT1[130]. Whatever the uptake mechanism is, it is likely that over time the amount of free DFX increases in PT cells, leading to the specific dysfunction of these cells and therefore to a Fanconi syndrome.

4.6 Outstanding questions

The exact mechanism of how DFX induces mitochondrial toxicity could not be revealed, although a number of potential explanations for DFX induced mitochondrial swelling could be disproven. The question arises whether there is an unknown biomarker that is more sensitive to mitochondrial injury than currently used readouts, such as oxygen consumption and cytochrome c release.

It remains unclear whether DFX enters the PT cell bound to albumin or whether the chelator appears unbound in the urine enabling the drug to enter the PT cell freely. Further investigations on the effect of DFX on the inner mitochondrial membrane would also be helpful to determine whether DFX interacts with the MICOS complex[243], with lipids like cardiolipin or other proteins.

Not every patient taking DFX develops Fanconi syndrome, although there are several risk factors including age >65 years, pre-existing renal or comorbid conditions such as type 2 diabetes mellitus, medicinal drugs that depress renal functions (NSAIDs or cyclosporine), or rapid iron removal[244, 245]. Most strikingly are patients with a higher reduction of iron burden more likely to develop nephrotoxicity[246]. These patients might have higher levels of the free drug, which would correspond to the data obtained in our experiments.

Understanding mechanisms of drug induced toxicity is very important for several reasons. First of all, the discovery of the pathway of toxicity can give insight into pathological processes that are common in different organs. It can also help in understanding why putative treatments (for example mitochondrial targeted anti-oxidants[247]) are effective against some kidney insults but not others. Second, the study of toxicity can provide new

insights into basic physiological processes in cells, for example, how mitochondria swell in pathological states. Thirdly, and most importantly, gaining insight into the mechanisms of drug toxicity allows future drug design to avoid severe adverse effects.

In summary, we discovered that DFX-induced kidney injury is explained by a previously unknown off-target effect, leading to mitochondrial dysfunction without causing respiratory chain dysfunction, oxidative stress or opening of the mPTP. Due to the novelty of the mechanism of toxicity, and due to the lack of biomarkers predicting nephrotoxicity, DFX was released to the market despite these dramatic side effects, causing it to be ranked second on the list of drug associated patient deaths by the ISMP in 2009[117]. These findings highlight that drugs can have unexpected side effects and that imaging can be a very handy tool in revealing novel mechanisms of drug toxicity.

5 SUMMARY

Drug toxicity is a major cause of acquired kidney disease, but in most cases the mechanisms are unknown. The oral iron chelator Deferasirox (DFX) frequently causes renal Fanconi syndrome, a functional defect in the proximal tubule (PT), for previously unknown reasons. PT cells are densely packed with mitochondria, which require iron for normal metabolism. It has been postulated that DFX toxicity might occur due to the chelation of iron in mitochondria, but other clinically used iron chelators do not cause kidney injury.

Using live imaging in PT-derived cells and fresh kidney slices of mouse kidney cortex, we discovered that DFX induces rapid swelling of mitochondria, leading ultimately to rupture of the mitochondrial membrane. Swollen mitochondria remained polarized but were more vulnerable to laser induced damage and oxidative stress. The toxic effect of DFX is not due to iron chelation, since other iron chelators did not cause mitochondrial swelling. DFX-induced mitochondrial swelling occurs in the absence of respiratory chain inhibition and oxidative stress, is not explained by a change of inner mitochondrial membrane permeability (including opening of the transition pore) and is rapidly reversible. Using electron microscopy and intravital multiphoton microscopy, we observed that mice given DFX for 10 days showed evidence of mitochondrial swelling and dysfunction in vivo, exclusively in the PT, as well as impaired solute transport (consistent with Fanconi syndrome). DFX is mainly albumin bound in blood, and we found that only the free drug causes toxicity in vitro, which might explain why the drug is tolerated by patients. Furthermore, since albumin is actively taken up by the PT, this could also explain the localization of DFX toxicity to this nephron segment. The established nephrotoxin diclofenac produces a similar phenotype (mitochondrial swelling without depolarization), implying a common underlying mechanism of toxicity.

In summary, we found that DFX induces kidney disease due to a novel off-target effect on mitochondrial morphology.

6 ZUSAMMENFASSUNG

Akutes Nierenversagen wird zu einem grossen Teil von Xenobiotika verursacht, wobei die dahinterstehenden Ursachen oftmals nicht bekannt sind. Der orale Eisenchelator Deferasirox (DFX) führt, aus bisher ungeklärten Gründen, in vielen Fällen zu einer Dysfunktion des proximalen Tubulus (PT), dem sogenannten Fanconi Syndrom. Zellen des PT sind reich an Mitochondrien, für deren normalen Metabolismus Eisen essentiell ist. Bisher wurde vermutet, dass sich die Toxizität von DFX auf dessen Fähigkeit Eisen in Mitohcondrian zu binden gründet; jedoch zeigen andere in der Klinik verwendeten Eisenchelatoren keine Anzeichen dafür, nierenschädlich zu sein.

Wir konnten mit Hilfe von mikroskopischen Studien in lebenden Zellen des PT und in frischen Nierenschnitten des Cortexes der Mäuseniere zeigen, dass DFX zu einem schnellen Anschwellen und letztendlich zur Ruptur der Membran der Mitochondrien führt. Die geschwollenen Organellen behielten ihr Membranpotential, reagierten aber sensibler auf Laser-induzierten und oxidativen Stress. Da andere Eisenchelatoren nicht zum Anschwellen der Mitochondrien führten, konnten wir schlussfolgern, dass die Toxizität von DFX nicht auf dessen Fähigkeit, Eisen zu binden, beruht. Das von DFX verursachte Anschwellen der Mitochondrien trat auf, ohne dabei die oxidative Phosphorylierung zu beeinflussen. Ausserdem führte eine Behandlung mit DFX weder zur Induktion oxidativen Stresses, noch zur Veränderung der Permeabilität der mitochondrialen Membran. Der Effekt von DFX war ausserdem durch die Zugabe von Eisen leicht rückgängig zu machen.

In Mäusen, die zehn Tage mit DFX behandelt worden waren, konnte mit Hilfe von intravitaler und Elektronenmikroskopie exklusiv in Zellen des PT ein Anschwellen der Mitochondrien detektiert werden. Zudem war die Aufnahme von Molekülen im PT beeinträchtigt, übereinstimmend mit den Symptomen eines Fanconi Syndroms. Wir konnten in vitro zeigen, dass nur ungebundenes DFX toxisch ist. In der Zirkulation kommt DFX fast ausschliesslich gebunden an Albumin vor, was erklärt, warum DFX von Patienten zunächst gut toleriert wird. Da Albumin aktiv in die Zellen des PT aufgenommen wird, könnte es sein, dass dies die spezifische Lokalisation der Toxizität in den PT erklärt. Zudem konnten wir zeigen, dass Diclofenac, ein bekannterweise nierenschädigendes Medikament, einen ähnlichen Phänotyp (Schwellung der Mitochondrien ohne Depolarisation) in unserem Zellmodel des PT auslöste. Dies könnte ein Hinweis auf einen gemeinsamen, grundlegenden Mechanismus sein.

Zusammenfassend lässt sich sagen, dass DFX durch einen neuen off-target Effekt auf Mitochondrien zu Nierenschädigung führt.

7 ACKNOWLEDGEMENTS

First of all, I would like to thank Prof. Andrew Hall for giving me the opportunity to continue my work in the field of nephrotoxicology. Thanks for advice, guidance, thoughts and an open mind in trying to explain what the results of my experiment could mean.

Thanks to the members of my thesis committee, Dr. Sophie De Seigneux and Prof. Johannes Loffing, for giving input and challenging me with questions during the committee meetings.

This work would not have been possible without the great help of the imaging facility ZMB and its employees, that kept the microscopes in perfect condition and were happy to help whenever a question regarding anything imaging related came up. Special thanks also for sharing the tissue culture facility with me – pleasure to work there with Carmen.

In this elaborate project more than one person was involved with their mind and some people also with their hands. Thanks to the members of "my sub-group" Claus and Dominik, for submitting their thoughts into this project and for analyzing blinking mitochondria and performing intravital imaging. Thanks to Susan for helping out in spotting swollen mitochondria with the EM, although the machine refused to work when we had our samples. Milice, Brankov sine , thanks for sitting with me at the new MP system in the dark with some kidney slices. Liposomes would not have existed without the hands of Michael. Thank you for your help and for being curious about my project.

Thanks to Joana, Eilidh, Adam and Marcello, the rest of the Hall Lab crew, who were great in giving advice and supporting me during the time of my PhD – especially when experiments did not show the results that I expected.
Thanks also to the rest of the Institute of Anatomy for providing a nice working atmosphere and for sharing knowledge and equipment.

A special thanks to my personal support, my family. Thanks for being there for me Tina, Karen and Mum. I know I would not be where I am now without you.

At last I'd like to dedicate this work to you, Papa. I know you are not able to physically read this anymore, but I hope somehow you will get to know that I completed my PhD and I hope you are proud of me and send me one of your lovely smiles from up there.

8 PUBLICATIONS

E.M. Gottwald, et al. (2017) The iron chelator Deferasirox causes kidney disease via mitochondrial toxicity. Submitted to Kidney International

E.M. Gottwald, et al. (2017) The targeted anti-oxidant MitoQ causes mitochondrial swelling and depolarization in kidney tissue. Submitted to Physiology Reports

E.M. Gottwald, et al. (2017) The iron chelator Deferasirox causes kidney disease via mitochondrial dysfunction. American Society of Nephrology Annual Meeting, New Orleans, USA.

E.M. Gottwald, A.M. Hall (2015) The iron chelator Deferasirox induces nephrotoxicity via mitochondrial dysfunction. NCCR kidney.ch meeting, Murten

9 CURRICULUM VITAE

Name: Esther Maria Gottwald

Geburtsdatum: 12.05.1989

Nationalität: Deutsch

Ausbildung:

09/1999 - 06/2008:	Abitur am Gymnasium Eschenbach in der Oberpfalz
10/2008 - 07/2011:	B.Sc. Biomedizin, Julius-Maximilians-Universität Würzburg Thesis: In vitro Untersuchungen zur Nephrotoxizität neuer Polymyxin Antibiotika
10/2011 - 06/2013:	M.Sc. Biomedizin, Julius-Maximilians-Universität Würzburg Thesis: Methods for improved detection of kidney injury
11/2013 - 01/2017:	Doktoratsstudium an der Universität Zürich im Programm Integrative Molecular Medicine

10 REFERENCES

1. Bellomo R, Kellum JA, Ronco C. Acute kidney injury. *Lancet* 2012; **380:** 756-766.

2. Li PK, Burdmann EA, Mehta RL*, et al.* Acute kidney injury: global health alert. *Kidney Int* 2013; **83:** 372-376.

3. Murugan R, Kellum JA. Acute kidney injury: what's the prognosis? *Nat Rev Nephrol* 2011; **7:** 209-217.

4. Chertow GM, Levy EM, Hammermeister KE*, et al.* Independent association between acute renal failure and mortality following cardiac surgery. *Am J Med* 1998; **104:** 343-348.

5. de Mendonca A, Vincent JL, Suter PM*, et al.* Acute renal failure in the ICU: risk factors and outcome evaluated by the SOFA score. *Intensive Care Med* 2000; **26:** 915-921.

6. Vivino G, Antonelli M, Moro ML*, et al.* Risk factors for acute renal failure in trauma patients. *Intensive Care Med* 1998; **24:** 808-814.

7. Bellomo R, Ronco C, Kellum JA*, et al.* Acute renal failure - definition, outcome measures, animal models, fluid therapy and information technology needs: the Second International Consensus Conference of the Acute Dialysis Quality Initiative (ADQI) Group. *Crit Care* 2004; **8:** R204-212.

8. Hoste EA, Clermont G, Kersten A*, et al.* RIFLE criteria for acute kidney injury are associated with hospital mortality in critically ill patients: a cohort analysis. *Crit Care* 2006; **10:** R73.

9. Mehta RL, Cerda J, Burdmann EA*, et al.* International Society of Nephrology's 0by25 initiative for acute kidney injury (zero preventable deaths by 2025): a human rights case for nephrology. *Lancet* 2015; **385:** 2616-2643.

10. Liangos O, Wald R, O'Bell JW*, et al.* Epidemiology and outcomes of acute renal failure in hospitalized patients: a national survey. *Clin J Am Soc Nephrol* 2006; **1:** 43-51.

11. Naughton CA. Drug-induced nephrotoxicity. *Am Fam Physician* 2008; **78:** 743-750.

12. Perazella MA. Renal vulnerability to drug toxicity. *Clin J Am Soc Nephrol* 2009; **4:** 1275-1283.

13. Berne RM, Levy MN, Koeppen BM*, et al. Berne & Levy physiology*, 6th edn. Mosby/Elsevier: Philadelphia, PA, 2010.

14. Boogaard PJ, Mulder GJ, Nagelkerke JF. Isolated proximal tubular cells from rat kidney as an in vitro model for studies on nephrotoxicity. II. Alpha-methylglucose uptake as a sensitive parameter for mechanistic studies of acute toxicity by xenobiotics. *Toxicol Appl Pharmacol* 1989; **101:** 144-157.

15. Bertram JF, Douglas-Denton RN, Diouf B*, et al.* Human nephron number: implications for health and disease. *Pediatr Nephrol* 2011; **26:** 1529-1533.

16. McQueen CA. *Comprehensive toxicology*, 2nd edn. Elsevier: Amsterdam, 2010.

17. Kriz W, Bankir L. A standard nomenclature for structure of the kidney. The Renal Commission of the International Union of Physiological Sciences(IUPS). *Anat Embryol (Berl)* 1988; **178:** N1-8.

18. Suzuki T. *Zur Morphologie der Nierensekretion unter physiologischen und pathologischen Bedingungen*. G. Fischer: Jena, 1912.

19. Sjöstrand F. Über die Eigenfluoreszenz tierischer Gewebe mit besonderer Berücksichtigung der Säugetierniere. Stockholm, 1944.

20. American Physiological Society: Comprehensive physiology. In, S.l., Wiley-Blackwell, pp Online-Ressource

21. Zhuo JL, Li XC. Proximal nephron. *Compr Physiol* 2013; **3:** 1079-1123.

22. Feraille E, Doucet A. Sodium-potassium-adenosinetriphosphatase-dependent sodium transport in the kidney: hormonal control. *Physiol Rev* 2001; **81:** 345-418.

23. Avner ED, Sweeney WE, Jr., Nelson WJ. Abnormal sodium pump distribution during renal tubulogenesis in congenital murine polycystic kidney disease. *Proc Natl Acad Sci U S A* 1992; **89:** 7447-7451.

24. Molitoris BA, Dahl R, Geerdes A. Cytoskeleton disruption and apical redistribution of proximal tubule Na(+)-K(+)-ATPase during ischemia. *Am J Physiol* 1992; **263:** F488-495.

25. Gyory AZ, Kinne R. Energy source for transepithelial sodium transport in rat renal proximal tubules. *Pflugers Arch* 1971; **327:** 234-260.

26. Lee YJ, Lee YJ, Han HJ. Regulatory mechanisms of Na(+)/glucose cotransporters in renal proximal tubule cells. *Kidney Int Suppl* 2007**:** S27-35.

27. Wright EM. Renal Na(+)-glucose cotransporters. *Am J Physiol Renal Physiol* 2001; **280:** F10-18.

28. Wright EM, Loo DD, Hirayama BA. Biology of human sodium glucose transporters. *Physiol Rev* 2011; **91:** 733-794.

29. Custer M, Lotscher M, Biber J*, et al.* Expression of Na-P(i) cotransport in rat kidney: localization by RT-PCR and immunohistochemistry. *Am J Physiol* 1994; **266:** F767-774.

30. Segawa H, Kaneko I, Takahashi A*, et al.* Growth-related renal type II Na/Pi cotransporter. *J Biol Chem* 2002; **277:** 19665-19672.

31. Biber J, Hernando N, Forster I*, et al.* Regulation of phosphate transport in proximal tubules. *Pflugers Arch* 2009; **458:** 39-52.

32. Christensen EI, Gburek J. Protein reabsorption in renal proximal tubule-function and dysfunction in kidney pathophysiology. *Pediatr Nephrol* 2004; **19:** 714-721.

33. Christensen EI, Birn H. Megalin and cubilin: synergistic endocytic receptors in renal proximal tubule. *Am J Physiol Renal Physiol* 2001; **280:** F562-573.

34. Moestrup SK, Verroust PJ. Megalin- and cubilin-mediated endocytosis of protein-bound vitamins, lipids, and hormones in polarized epithelia. *Annu Rev Nutr* 2001; **21:** 407-428.

35. Kerjaschki D, Farquhar MG. The pathogenic antigen of Heymann nephritis is a membrane glycoprotein of the renal proximal tubule brush border. *Proc Natl Acad Sci U S A* 1982; **79:** 5557-5561.

36. Saito A, Pietromonaco S, Loo AK*, et al.* Complete cloning and sequencing of rat gp330/"megalin," a distinctive member of the low density lipoprotein receptor gene family. *Proc Natl Acad Sci U S A* 1994; **91:** 9725-9729.

37. Chatelet F, Brianti E, Ronco P*, et al.* Ultrastructural localization by monoclonal antibodies of brush border antigens expressed by glomeruli. I. Renal distribution. *Am J Pathol* 1986; **122:** 500-511.

38. Chatelet F, Brianti E, Ronco P*, et al.* Ultrastructural localization by monoclonal antibodies of brush border antigens expressed by glomeruli. II. Extrarenal distribution. *Am J Pathol* 1986; **122:** 512-519.

39. Sahali D, Mulliez N, Chatelet F*, et al.* Comparative immunochemistry and ontogeny of two closely related coated pit proteins. The 280-kd target of teratogenic antibodies and the 330-kd target of nephritogenic antibodies. *Am J Pathol* 1993; **142:** 1654-1667.

40. Yammani RR, Seetharam S, Seetharam B. Identification and characterization of two distinct ligand binding regions of cubilin. *J Biol Chem* 2001; **276:** 44777-44784.

41. Amsellem S, Gburek J, Hamard G*, et al.* Cubilin is essential for albumin reabsorption in the renal proximal tubule. *J Am Soc Nephrol* 2010; **21:** 1859-1867.

42. Gekle M, Mildenberger S, Freudinger R*, et al.* Kinetics of receptor-mediated endocytosis of albumin in cells derived from the proximal tubule of the kidney (opossum kidney cells): influence of Ca2+ and cAMP. *Pflugers Arch* 1995; **430:** 374-380.

43. Gekle M, Mildenberger S, Freudinger R*, et al.* Endosomal alkalinization reduces Jmax and Km of albumin receptor-mediated endocytosis in OK cells. *Am J Physiol* 1995; **268:** F899-906.

44. Morrissey KM, Stocker SL, Wittwer MB*, et al.* Renal transporters in drug development. *Annu Rev Pharmacol Toxicol* 2013; **53:** 503-529.

45. Moss DM, Neary M, Owen A. The role of drug transporters in the kidney: lessons from tenofovir. *Front Pharmacol* 2014; **5:** 248.

46. DeGorter MK, Xia CQ, Yang JJ*, et al.* Drug transporters in drug efficacy and toxicity. *Annu Rev Pharmacol Toxicol* 2012; **52:** 249-273.

47. Pagliarini DJ, Calvo SE, Chang B*, et al.* A mitochondrial protein compendium elucidates complex I disease biology. *Cell* 2008; **134:** 112-123.

48. Keenan TW, Awasthi YC, Crane FL. Cardiolipin from beef heart mitochondria: fatty acid positioning an molecular species distribution. *Biochem Biophys Res Commun* 1970; **40:** 1102-1109.

49. Waegemann K, Popov-Celeketic D, Neupert W*, et al.* Cooperation of TOM and TIM23 complexes during translocation of proteins into mitochondria. *J Mol Biol* 2015; **427:** 1075-1084.

50. Friedman JR, Mourier A, Yamada J*, et al.* MICOS coordinates with respiratory complexes and lipids to establish mitochondrial inner membrane architecture. *Elife* 2015; **4**.

51. Dyall SD, Brown MT, Johnson PJ. Ancient invasions: from endosymbionts to organelles. *Science* 2004; **304:** 253-257.

52. Boxma B, de Graaf RM, van der Staay GW*, et al.* An anaerobic mitochondrion that produces hydrogen. *Nature* 2005; **434:** 74-79.

53. Cox CJ, Foster PG, Hirt RP*, et al.* The archaebacterial origin of eukaryotes. *Proc Natl Acad Sci U S A* 2008; **105:** 20356-20361.

54. Martin WM, M. The origin of Mitochondria. *Nature Education* 2010; **3:** 58.

55. Duchen MR, Surin A, Jacobson J. Imaging mitochondrial function in intact cells. *Methods Enzymol* 2003; **361:** 353-389.

56. Schartl M, Arand M. *Biochemie und Molekularbiologie des Menschen*. Elsevier: München, 2009.

57. Hall JE, Guyton AC. *Guyton and Hall textbook of medical physiology*, 13th edition edn. Elsevier: Philadelphia, 2016.

58. Torti SV, Torti FM. Iron and cancer: more ore to be mined. *Nat Rev Cancer* 2013; **13:** 342-355.

59. Manz DH, Blanchette NL, Paul BT*, et al.* Iron and cancer: recent insights. *Ann N Y Acad Sci* 2016; **1368:** 149-161.

60. Richardson DR, Lane DJ, Becker EM*, et al.* Mitochondrial iron trafficking and the integration of iron metabolism between the mitochondrion and cytosol. *Proc Natl Acad Sci U S A* 2010; **107:** 10775-10782.

61. Rauen U, Springer A, Weisheit D*, et al.* Assessment of chelatable mitochondrial iron by using mitochondrion-selective fluorescent iron indicators with different iron-binding affinities. *Chembiochem* 2007; **8:** 341-352.

62. Paul BT, Manz DH, Torti FM*, et al.* Mitochondria and Iron: current questions. *Expert Rev Hematol* 2017; **10:** 65-79.

63. Padmalayam I, Hasham S, Saxena U*, et al.* Lipoic acid synthase (LASY): a novel role in inflammation, mitochondrial function, and insulin resistance. *Diabetes* 2009; **58:** 600-608.

64. Picciocchi A, Douce R, Alban C. Biochemical characterization of the Arabidopsis biotin synthase reaction. The importance of mitochondria in biotin synthesis. *Plant Physiol* 2001; **127:** 1224-1233.

65. Booker SJ, Grove TL. Mechanistic and functional versatility of radical SAM enzymes. *F1000 Biol Rep* 2010; **2:** 52.

66. Haag S, Sloan KE, Ranjan N*, et al.* NSUN3 and ABH1 modify the wobble position of mt-tRNAMet to expand codon recognition in mitochondrial translation. *EMBO J* 2016; **35:** 2104-2119.

67. Fu D, Jordan JJ, Samson LD. Human ALKBH7 is required for alkylation and oxidation-induced programmed necrosis. *Genes Dev* 2013; **27:** 1089-1100.

68. Dallman PR. Biochemical basis for the manifestations of iron deficiency. *Annu Rev Nutr* 1986; **6:** 13-40.

69. Klempa KL, Willis WT, Chengson R*, et al.* Iron deficiency decreases gluconeogenesis in isolated rat hepatocytes. *J Appl Physiol (1985)* 1989; **67:** 1868-1872.

70. Jarvis JH, Jacobs A. Morphological abnormalities in lymphocyte mitochondria associated with iron-deficiency anaemia. *J Clin Pathol* 1974; **27:** 973-979.

71. Dallman PR, Goodman JR. The effects of iron deficiency on the hepatocyte: a biochemical and ultrastructural study. *J Cell Biol* 1971; **48:** 79-90.

72. Walter PB, Knutson MD, Paler-Martinez A*, et al.* Iron deficiency and iron excess damage mitochondria and mitochondrial DNA in rats. *Proc Natl Acad Sci U S A* 2002; **99:** 2264-2269.

73. Dix TA, Aikens J. Mechanisms and biological relevance of lipid peroxidation initiation. *Chem Res Toxicol* 1993; **6:** 2-18.

74. Gao X, Campian JL, Qian M*, et al.* Mitochondrial DNA damage in iron overload. *J Biol Chem* 2009; **284:** 4767-4775.

75. Aguirre JD, Culotta VC. Battles with iron: manganese in oxidative stress protection. *J Biol Chem* 2012; **287:** 13541-13548.

76. Dixon SJ, Lemberg KM, Lamprecht MR*, et al.* Ferroptosis: an iron-dependent form of nonapoptotic cell death. *Cell* 2012; **149:** 1060-1072.

77. Rottenberg H, Hoek JB. The path from mitochondrial ROS to aging runs through the mitochondrial permeability transition pore. *Aging Cell* 2017; **16:** 943-955.

78. Bernardi P, Krauskopf A, Basso E*, et al.* The mitochondrial permeability transition from in vitro artifact to disease target. *FEBS J* 2006; **273:** 2077-2099.

79. Biasutto L, Azzolini M, Szabo I*, et al.* The mitochondrial permeability transition pore in AD 2016: An update. *Biochim Biophys Acta* 2016; **1863:** 2515-2530.

80. Zorov DB, Juhaszova M, Sollott SJ. Mitochondrial reactive oxygen species (ROS) and ROS-induced ROS release. *Physiol Rev* 2014; **94:** 909-950.

81. Huo H, Zhou Z, Qin J*, et al.* Erastin Disrupts Mitochondrial Permeability Transition Pore (mPTP) and Induces Apoptotic Death of Colorectal Cancer Cells. *PLoS One* 2016; **11:** e0154605.

82. Izzo V, Bravo-San Pedro JM, Sica V*, et al.* Mitochondrial Permeability Transition: New Findings and Persisting Uncertainties. *Trends Cell Biol* 2016; **26:** 655-667.

83. Vaseva AV, Marchenko ND, Ji K*, et al.* p53 opens the mitochondrial permeability transition pore to trigger necrosis. *Cell* 2012; **149:** 1536-1548.

84. Abderhalden E. Familiäre Cystindiathese. *Zeitschrift für physiologische Chemie* 1903; **38:** 557-561.

85. Lignac GOE. Über die Störung des Cystinstoffwechsels bei Kindern. *Deutsches Arch klin Med* 1924; **145**.

86. Fanconi G. Die nicht diabetischen Glykosurien und Hyperglykaemien des aelteren Kindes. *Jahrbuch fuer Kinderheilkunde* 1931; **133:** 257-300.

87. de Toni G. Remarks on the relationship between renal rickets (renal dwarfism) and renal diabetes. *Acta Pediatr* 1933; **16:** 479-484.

88. Debre R, Marie, J., Cleret Fet al. Rachitisme tardif coexistant avec une Nephrite chronique et une Glycosurie. *Archive de Medicine des Enfants* 1934; **37:** 597-606.

89. Fanconi G. <<*Der*>> *frühinfantile nephrotisch-glykosurische Zwergwuchs mit hypophosphatämischer Rachitis*. Karger: Berlin, 1936.

90. McCune DJ, Mason HH, Clarke HT. Intractable hypophosphatemic rickets with renal glycosuria and acidosis (The Fanconi Syndrome) Report of a case in which increased urinary organic acids were detected and identified, with a review of the literature. *Am J Dis Child* 1943; **65:** 81-146.

91. Hall AM, Bass P, Unwin RJ. Drug-induced renal Fanconi syndrome. *QJM* 2014; **107:** 261-269.

92. Scriver CR, Stanbury JB, Wyngaarden JB*, et al.* <<*The*>> *metabolic and molecular bases of inherited disease*, 7th edn. McGraw-Hill: New York, NY <etc.>, 1995.

93. Klootwijk ED, Reichold M, Unwin RJ*, et al.* Renal Fanconi syndrome: taking a proximal look at the nephron. *Nephrol Dial Transplant* 2015; **30:** 1456-1460.

94. Linkage of the gene for cystinosis to markers on the short arm of chromosome 17. The Cystinosis Collaborative Research Group. *Nat Genet* 1995; **10:** 246-248.

95. Assmann N, Dettmer K, Simbuerger JMB*, et al.* Renal Fanconi Syndrome Is Caused by a Mistargeting-Based Mitochondriopathy. *Cell Rep* 2016; **15:** 1423-1429.

96. Choudhury R, Diao A, Zhang F*, et al.* Lowe syndrome protein OCRL1 interacts with clathrin and regulates protein trafficking between endosomes and the trans-Golgi network. *Mol Biol Cell* 2005; **16:** 3467-3479.

97. Devuyst O, Thakker RV. Dent's disease. *Orphanet J Rare Dis* 2010; **5:** 28.

98. Nogawa K, Ishizaki A, Fukushima M*, et al.* Studies on the women with acquired Fanconi syndrome observed in the Ichi river basin polluted by cadmium. Is this Itai-itai disease? *Environ Res* 1975; **10:** 280-307.

99. Izzedine H, Launay-Vacher V, Isnard-Bagnis C*, et al.* Drug-induced Fanconi's syndrome. *Am J Kidney Dis* 2003; **41:** 292-309.

100. Launay-Vacher V, Izzedine H, Karie S*, et al.* Renal tubular drug transporters. *Nephron Physiol* 2006; **103:** p97-106.

101. Perazella MA, Moeckel GW. Nephrotoxicity from chemotherapeutic agents: clinical manifestations, pathobiology, and prevention/therapy. *Semin Nephrol* 2010; **30:** 570-581.

102. Montine TJ, Borch RF. Quiescent LLC-PK1 cells as a model for cis-diamminedichloroplatinum(II) nephrotoxicity and modulation by thiol rescue agents. *Cancer Res* 1988; **48:** 6017-6024.

103. Skinner R. Nephrotoxicity--what do we know and what don't we know? *J Pediatr Hematol Oncol* 2011; **33:** 128-134.

104. Wong CC, Botting NP, Orfila C*, et al.* Flavonoid conjugates interact with organic anion transporters (OATs) and attenuate cytotoxicity of adefovir mediated by organic anion transporter 1 (OAT1/SLC22A6). *Biochem Pharmacol* 2011; **81:** 942-949.

105. Ho ES, Lin DC, Mendel DB*, et al.* Cytotoxicity of antiviral nucleotides adefovir and cidofovir is induced by the expression of human renal organic anion transporter 1. *J Am Soc Nephrol* 2000; **11:** 383-393.

106. Hall AM. Update on tenofovir toxicity in the kidney. *Pediatr Nephrol* 2013; **28:** 1011-1023.

107. Hall AM, Hendry BM, Nitsch D*, et al.* Tenofovir-associated kidney toxicity in HIV-infected patients: a review of the evidence. *Am J Kidney Dis* 2011; **57:** 773-780.

108. Herlitz LC, Mohan S, Stokes MB*, et al.* Tenofovir nephrotoxicity: acute tubular necrosis with distinctive clinical, pathological, and mitochondrial abnormalities. *Kidney Int* 2010; **78:** 1171-1177.

109. Begg EJ, Barclay ML. Aminoglycosides--50 years on. *Br J Clin Pharmacol* 1995; **39:** 597-603.

110. Mendes CA, Cordeiro JA, Burdmann EA. Prevalence and risk factors for acute kidney injury associated with parenteral polymyxin B use. *Ann Pharmacother* 2009; **43:** 1948-1955.

111. Soares DS, Reis ADF, Silva Junior GBD*, et al.* Polymyxin-B and vancomycin-associated acute kidney injury in critically ill patients. *Pathog Glob Health* 2017; **111:** 137-142.

112. Aran JM, Dulon D, Hiel H*, et al.* [Ototoxicity of aminosides: recent results on uptake and clearance of gentamycin by sensory cells of the cochlea]. *Rev Laryngol Otol Rhinol (Bord)* 1993; **114:** 125-128.

113. Abdelraouf K, Chang KT, Yin T*, et al.* Uptake of polymyxin B into renal cells. *Antimicrob Agents Chemother* 2014; **58:** 4200-4202.

114. Jorgensen TG, Weis-Fogh US, Nielsen HH*, et al.* Salicylate- and aspirin-induced uncoupling of oxidative phosphorylation in mitochondria isolated from the mucosal membrane of the stomach. *Scand J Clin Lab Invest* 1976; **36:** 649-654.

115. Tatematsu Y, Hayashi H, Taguchi R*, et al.* Effect of N-Phenylanthranilic Acid Scaffold Nonsteroidal Anti-inflammatory Drugs on the Mitochondrial Permeability Transition. *Biol Pharm Bull* 2016; **39:** 278-284.

116. Uyemura SA, Santos AC, Mingatto FE*, et al.* Diclofenac sodium and mefenamic acid: potent inducers of the membrane permeability transition in renal cortex mitochondria. *Arch Biochem Biophys* 1997; **342:** 231-235.

117. Kontoghiorghes GJ. A record of 1320 suspect, deferasirox-related, patient deaths reported in 2009: insufficient toxicity testing, low efficacy and lack of transparency may endanger the lives of iron loaded patients. *Hemoglobin* 2011; **35:** 301-311.

118. Vichinsky E. Clinical application of deferasirox: practical patient management. *Am J Hematol* 2008; **83:** 398-402.

119. Diaz-Garcia JD, Gallegos-Villalobos A, Gonzalez-Espinoza L*, et al.* Deferasirox nephrotoxicity-the knowns and unknowns. *Nat Rev Nephrol* 2014; **10:** 574-586.

120. Hider RC, Zhou T. The design of orally active iron chelators. *Ann N Y Acad Sci* 2005; **1054:** 141-154.

121. Nick H, Acklin P, Lattmann R*, et al.* Development of tridentate iron chelators: from desferrithiocin to ICL670. *Curr Med Chem* 2003; **10:** 1065-1076.

122. Kushner JP, Porter JP, Olivieri NF. Secondary iron overload. *Hematology Am Soc Hematol Educ Program* 2001**:** 47-61.

123. Woehler F. The Treatment of Haemochromatosis with Desferrioxamine. *Acta Haematol* 1963; **30:** 65-87.

124. Brittenham GM, Griffith PM, Nienhuis AW*, et al.* Efficacy of deferoxamine in preventing complications of iron overload in patients with thalassemia major. *N Engl J Med* 1994; **331:** 567-573.

125. Naegeli HZ, H. Stoffwechselprodukte von Mikroorganismen - Ferrithiocin. *Helvetica Chimica Acta* 1980; **63:** 1400-1406.

126. Pfannkuch F, Bentley P, Schnebli HP. Future of oral iron chelator deferiprone (L1). *Lancet* 1993; **341:** 1480.

127. Mobarra N, Shanaki M, Ehteram H*, et al.* A Review on Iron Chelators in Treatment of Iron Overload Syndromes. *Int J Hematol Oncol Stem Cell Res* 2016; **10:** 239-247.

128. Olivieri NF, Brittenham GM, McLaren CE*, et al.* Long-term safety and effectiveness of iron-chelation therapy with deferiprone for thalassemia major. *N Engl J Med* 1998; **339:** 417-423.

129. Sergejew T, Forgiarini P, Schnebli HP. Chelator-induced iron excretion in iron-overloaded marmosets. *Br J Haematol* 2000; **110:** 985-992.

130. EMA. Scientific discussion of Exjade (Deferasirox). http://wwwemaeuropaeu/docs/en_GB/document_library/EPAR_-_Scientific_Discussion/human/000670/WC500033929pdf 2006.

131. Nisbet-Brown E, Olivieri NF, Giardina PJ, *et al.* Effectiveness and safety of ICL670 in iron-loaded patients with thalassaemia: a randomised, double-blind, placebo-controlled, dose-escalation trial. *Lancet* 2003; **361:** 1597-1602.

132. Piga A, Galanello R, Forni GL, *et al.* Randomized phase II trial of deferasirox (Exjade, ICL670), a once-daily, orally-administered iron chelator, in comparison to deferoxamine in thalassemia patients with transfusional iron overload. *Haematologica* 2006; **91:** 873-880.

133. Cappellini MD. Iron-chelating therapy with the new oral agent ICL670 (Exjade). *Best Pract Res Clin Haematol* 2005; **18:** 289-298.

134. Bollig C, Schell LK, Rucker G, *et al.* Deferasirox for managing iron overload in people with thalassaemia. *Cochrane Database Syst Rev* 2017; **8:** CD007476.

135. Dubourg L, Laurain C, Ranchin B, *et al.* Deferasirox-induced renal impairment in children: an increasing concern for pediatricians. *Pediatr Nephrol* 2012; **27:** 2115-2122.

136. Even-Or E, Becker-Cohen R, Miskin H. Deferasirox treatment may be associated with reversible renal Fanconi syndrome. *Am J Hematol* 2010; **85:** 132-134.

137. Grange S, Bertrand DM, Guerrot D, *et al.* Acute renal failure and Fanconi syndrome due to deferasirox. *Nephrol Dial Transplant* 2010; **25:** 2376-2378.

138. Wei HY, Yang CP, Cheng CH, *et al.* Fanconi syndrome in a patient with beta-thalassemia major after using deferasirox for 27 months. *Transfusion* 2011; **51:** 949-954.

139. Yacobovich J, Stark P, Barzilai-Birenbaum S, *et al.* Acquired proximal renal tubular dysfunction in beta-thalassemia patients treated with deferasirox. *J Pediatr Hematol Oncol* 2010; **32:** 564-567.

140. Rheault MN, Bechtel H, Neglia JP, *et al.* Reversible Fanconi syndrome in a pediatric patient on deferasirox. *Pediatr Blood Cancer* 2011; **56:** 674-676.

141. Adler M, Ramm S, Hafner M, *et al.* A Quantitative Approach to Screen for Nephrotoxic Compounds In Vitro. *J Am Soc Nephrol* 2016; **27:** 1015-1028.

142. Repetto G, del Peso A, Zurita JL. Neutral red uptake assay for the estimation of cell viability/cytotoxicity. *Nat Protoc* 2008; **3:** 1125-1131.

143. Korzeniewski C, Callewaert DM. An enzyme-release assay for natural cytotoxicity. *J Immunol Methods* 1983; **64:** 313-320.

144. Persson M, Hornberg JJ. Advances in Predictive Toxicology for Discovery Safety through High Content Screening. *Chem Res Toxicol* 2016; **29:** 1998-2007.

145. Stokes GG. On the Change of Refrangibility of Light. *Philosophical Transactions of the Royal Society of London* 1852; **142:** 463-562.

146. Jablonski AN, 839–840 (1933). Efficiency of anti-stokes fluorescence in dyes. *Nature* 1933; **131:** 839-840.

147. Wright SJ, Centonze VE, Stricker SA*, et al.* Introduction to confocal microscopy and three-dimensional reconstruction. *Methods Cell Biol* 1993; **38:** 1-45.

148. Hell SW, Wichmann J. Breaking the diffraction resolution limit by stimulated emission: stimulated-emission-depletion fluorescence microscopy. *Opt Lett* 1994; **19:** 780-782.

149. Rust MJ, Bates M, Zhuang X. Sub-diffraction-limit imaging by stochastic optical reconstruction microscopy (STORM). *Nat Methods* 2006; **3:** 793-795.

150. Dykens JA, Will Y. The significance of mitochondrial toxicity testing in drug development. *Drug Discov Today* 2007; **12:** 777-785.

151. Wierer S, Peter S, Elgass K*, et al.* Determination of the in vivo redox potential by one-wavelength spectro-microscopy of roGFP. *Anal Bioanal Chem* 2012; **403:** 737-744.

152. Drummen GP, van Liebergen LC, Op den Kamp JA*, et al.* C11-BODIPY(581/591), an oxidation-sensitive fluorescent lipid peroxidation probe: (micro)spectroscopic characterization and validation of methodology. *Free Radic Biol Med* 2002; **33:** 473-490.

153. Takahashi A, Camacho P, Lechleiter JD*, et al.* Measurement of intracellular calcium. *Physiol Rev* 1999; **79:** 1089-1125.

154. Trollinger DR, Cascio WE, Lemasters JJ. Selective loading of Rhod 2 into mitochondria shows mitochondrial Ca2+ transients during the contractile cycle in adult rabbit cardiac myocytes. *Biochem Biophys Res Commun* 1997; **236:** 738-742.

155. Gerencser AA, Adam-Vizi V. Mitochondrial Ca2+ dynamics reveals limited intramitochondrial Ca2+ diffusion. *Biophys J* 2005; **88:** 698-714.

156. Mayevsky A, Chance B. Oxidation-reduction states of NADH in vivo: from animals to clinical use. *Mitochondrion* 2007; **7:** 330-339.

157. Helmchen F, Denk W. Deep tissue two-photon microscopy. *Nat Methods* 2005; **2:** 932-940.

158. Goeppert-Mayer M. Über Elementarakte mit zwei Quantensprüngen (On elementary processes with two quantum steps). *Ann Phys* 1931; **9:** 273-294.

159. Xu C, Guild J, Webb W*, et al.* Determination of absolute two-photon excitation cross sections by in situ second-order autocorrelation. *Opt Lett* 1995; **20:** 2372.

160. Schuh CD, Haenni D, Craigie E*, et al.* Long wavelength multiphoton excitation is advantageous for intravital kidney imaging. *Kidney Int* 2016; **89:** 712-719.

161. Hall AM, Unwin RJ, Parker N*, et al.* Multiphoton imaging reveals differences in mitochondrial function between nephron segments. *J Am Soc Nephrol* 2009; **20:** 1293-1302.

162. Eshbach ML, Weisz OA. Receptor-Mediated Endocytosis in the Proximal Tubule. *Annu Rev Physiol* 2017; **79:** 425-448.

163. Ovesny M, Krizek P, Borkovec J*, et al.* ThunderSTORM: a comprehensive ImageJ plug-in for PALM and STORM data analysis and super-resolution imaging. *Bioinformatics* 2014; **30:** 2389-2390.

164. Firsov AM, Kotova EA, Orlov VN*, et al.* A mitochondria-targeted antioxidant can inhibit peroxidase activity of cytochrome c by detachment of the protein from liposomes. *FEBS Lett* 2016; **590:** 2836-2843.

165. Szeto HH, Liu S, Soong Y*, et al.* Mitochondria-targeted peptide accelerates ATP recovery and reduces ischemic kidney injury. *J Am Soc Nephrol* 2011; **22:** 1041-1052.

166. Birk AV, Liu S, Soong Y*, et al.* The mitochondrial-targeted compound SS-31 re-energizes ischemic mitochondria by interacting with cardiolipin. *J Am Soc Nephrol* 2013; **24:** 1250-1261.

167. Zhou M, Diwu Z, Panchuk-Voloshina N*, et al.* A stable nonfluorescent derivative of resorufin for the fluorometric determination of trace hydrogen peroxide: applications in detecting the activity of phagocyte NADPH oxidase and other oxidases. *Anal Biochem* 1997; **253:** 162-168.

168. Vladimirov YA, Proskurnina EV, Izmailov DY*, et al.* Cardiolipin activates cytochrome c peroxidase activity since it facilitates H(2)O(2) access to heme. *Biochemistry (Mosc)* 2006; **71:** 998-1005.

169. Birk AV, Chao WM, Liu S*, et al.* Disruption of cytochrome c heme coordination is responsible for mitochondrial injury during ischemia. *Biochim Biophys Acta* 2015; **1847:** 1075-1084.

170. Vincent AE, Turnbull DM, Eisner V*, et al.* Mitochondrial Nanotunnels. *Trends Cell Biol* 2017; **27:** 787-799.

171. Thomas DA, Stauffer C, Zhao K*, et al.* Mitochondrial targeting with antioxidant peptide SS-31 prevents mitochondrial depolarization, reduces islet cell apoptosis, increases islet cell yield, and improves posttransplantation function. *J Am Soc Nephrol* 2007; **18:** 213-222.

172. Radi R, Sims S, Cassina A*, et al.* Roles of catalase and cytochrome c in hydroperoxide-dependent lipid peroxidation and chemiluminescence in rat heart and kidney mitochondria. *Free Radic Biol Med* 1993; **15:** 653-659.

173. Radi R, Turrens JF, Freeman BA. Cytochrome c-catalyzed membrane lipid peroxidation by hydrogen peroxide. *Arch Biochem Biophys* 1991; **288:** 118-125.

174. Norman KG, Canter JA, Shi M*, et al.* Cyclosporine A suppresses keratinocyte cell death through MPTP inhibition in a model for skin cancer in organ transplant recipients. *Mitochondrion* 2010; **10:** 94-101.

175. Quintanilla RA, Jin YN, von Bernhardi R*, et al.* Mitochondrial permeability transition pore induces mitochondria injury in Huntington disease. *Mol Neurodegener* 2013; **8:** 45.

176. Kluck RM, Bossy-Wetzel E, Green DR*, et al.* The release of cytochrome c from mitochondria: a primary site for Bcl-2 regulation of apoptosis. *Science* 1997; **275:** 1132-1136.

177. Lehninger AL. Water uptake and extrusion by mitochondria in relation to oxidative phosphorylation. *Physiol Rev* 1962; **42:** 467-517.

178. Tauskela JS. MitoQ--a mitochondria-targeted antioxidant. *IDrugs* 2007; **10:** 399-412.

179. Kalinovich AV, Mattsson CL, Youssef MR*, et al.* Mitochondria-targeted dodecyltriphenylphosphonium (C12TPP) combats high-fat-diet-induced obesity in mice. *Int J Obes (Lond)* 2016; **40:** 1864-1874.

180. Lofrumento DD, La Piana G, Abbrescia DI*, et al.* Valinomycin induced energy-dependent mitochondrial swelling, cytochrome c release, cytosolic NADH/cytochrome c oxidation and apoptosis. *Apoptosis* 2011; **16:** 1004-1013.

181. Piasek A, Thyberg J. Effects of colchicine on endocytosis and cellular inactivation of horseradish peroxidase in cultured chondrocytes. *J Cell Biol* 1979; **81:** 426-437.

182. Decorti G, Malusa N, Furlan G*, et al.* Endocytosis of gentamicin in a proximal tubular renal cell line. *Life Sci* 1999; **65:** 1115-1124.

183. Verhulst A, D'Haese PC, De Broe ME. Inhibitors of HMG-CoA reductase reduce receptor-mediated endocytosis in human kidney proximal tubular cells. *J Am Soc Nephrol* 2004; **15:** 2249-2257.

184. Hall AM, Campanella M, Loesch A*, et al.* Albumin uptake in OK cells exposed to rotenone: a model for studying the effects of mitochondrial dysfunction on endocytosis in the proximal tubule? *Nephron Physiol* 2010; **115:** p9-p19.

185. Masubuchi Y, Nakayama S, Horie T. Role of mitochondrial permeability transition in diclofenac-induced hepatocyte injury in rats. *Hepatology* 2002; **35:** 544-551.

186. Yoshida Y, Singh I, Darby CP. Effect of salicylic acid and calcium on mitochondrial functions. *Acta Neurol Scand* 1992; **85:** 191-196.

187. Sanchez-Gonzalez PD, Lopez-Hernandez FJ, Morales AI*, et al.* Effects of deferasirox on renal function and renal epithelial cell death. *Toxicol Lett* 2011; **203:** 154-161.

188. Beger RD, Sun J, Schnackenberg LK. Metabolomics approaches for discovering biomarkers of drug-induced hepatotoxicity and nephrotoxicity. *Toxicol Appl Pharmacol* 2010; **243:** 154-166.

189. Casarett LJ, Doull J, Klaassen CD. *Casarett and Doull's toxicology the basic science of poisons*, 7th edn. McGraw-Hill: New York, 2008.

190. Lameire NH, Bagga A, Cruz D*, et al.* Acute kidney injury: an increasing global concern. *Lancet* 2013; **382:** 170-179.

191. Szeto CC, Chow KM. Nephrotoxicity related to new therapeutic compounds. *Ren Fail* 2005; **27:** 329-333.

192. Redfern J, Menzies M, Briffa T*, et al.* Impact of medical consultation frequency on modifiable risk factors and medications at 12 months after acute coronary syndrome in the CHOICE randomised controlled trial. *Int J Cardiol* 2010; **145:** 481-486.

193. Vaidya VS, Ramirez V, Ichimura T*, et al.* Urinary kidney injury molecule-1: a sensitive quantitative biomarker for early detection of kidney tubular injury. *Am J Physiol Renal Physiol* 2006; **290:** F517-529.

194. Bellomo R. Acute renal failure. *Semin Respir Crit Care Med* 2011; **32:** 639-650.

195. Shemin D, Dworkin LD. Neutrophil gelatinase-associated lipocalin (NGAL) as a biomarker for early acute kidney injury. *Crit Care Clin* 2011; **27:** 379-389.

196. Weiland C, Ahr HJ, Vohr HW*, et al.* Characterization of primary rat proximal tubular cells by gene expression analysis. *Toxicol In Vitro* 2007; **21:** 466-491.

197. Kusaba T, Lalli M, Kramann R*, et al.* Differentiated kidney epithelial cells repair injured proximal tubule. *Proc Natl Acad Sci U S A* 2014; **111:** 1527-1532.

198. Lin Z, Will Y. Evaluation of drugs with specific organ toxicities in organ-specific cell lines. *Toxicol Sci* 2012; **126:** 114-127.

199. Johnson LV, Walsh ML, Chen LB. Localization of mitochondria in living cells with rhodamine 123. *Proc Natl Acad Sci U S A* 1980; **77:** 990-994.

200. Collins JA, Wood ST, Nelson KJ*, et al.* Oxidative Stress Promotes Peroxiredoxin Hyperoxidation and Attenuates Pro-survival Signaling in Aging Chondrocytes. *J Biol Chem* 2016; **291:** 6641-6654.

201. Hoebe RA, Van Oven CH, Gadella TW, Jr.*, et al.* Controlled light-exposure microscopy reduces photobleaching and phototoxicity in fluorescence live-cell imaging. *Nat Biotechnol* 2007; **25:** 249-253.

202. Molitoris BA, Sandoval RM. Intravital multiphoton microscopy of dynamic renal processes. *Am J Physiol Renal Physiol* 2005; **288:** F1084-1089.

203. Forster RP. Use of Thin Kidney Slices and Isolated Renal Tubules for Direct Study of Cellular Transport Kinetics. *Science* 1948; **108:** 65-67.

204. Mudge GH. Studies on potassium accumulation by rabbit kidney slices; effect of metabolic activity. *Am J Physiol* 1951; **165:** 113-127.

205. Kondoh H. Cellular life span and the Warburg effect. *Exp Cell Res* 2008; **314:** 1923-1928.

206. Crawford C, Kennedy-Lydon T, Sprott C*, et al.* An intact kidney slice model to investigate vasa recta properties and function in situ. *Nephron Physiol* 2012; **120:** p17-31.

207. Fortney SR, Lynn WS, Jr. Role of Ascorbate and Cysteine on Swelling and Lipid Peroxidation in Rat Liver Mitochondria. *Arch Biochem Biophys* 1964; **104:** 241-247.

208. Kinnally KW, Peixoto PM, Ryu SY*, et al.* Is mPTP the gatekeeper for necrosis, apoptosis, or both? *Biochim Biophys Acta* 2011; **1813:** 616-622.

209. Kwong JQ, Molkentin JD. Physiological and pathological roles of the mitochondrial permeability transition pore in the heart. *Cell Metab* 2015; **21:** 206-214.

210. Mitchell P. Chemiosmotic coupling in oxidative and photosynthetic phosphorylation. *Biol Rev Camb Philos Soc* 1966; **41:** 445-502.

211. Peng TI, Jou MJ. Mitochondrial swelling and generation of reactive oxygen species induced by photoirradiation are heterogeneously distributed. *Ann N Y Acad Sci* 2004; **1011:** 112-122.

212. Tolkovsky AM, Xue L, Fletcher GC*, et al.* Mitochondrial disappearance from cells: a clue to the role of autophagy in programmed cell death and disease? *Biochimie* 2002; **84:** 233-240.

213. Bowes T, Gupta RS. Novel mitochondrial extensions provide evidence for a link between microtubule-directed movement and mitochondrial fission. *Biochem Biophys Res Commun* 2008; **376:** 40-45.

214. Baliga R, Zhang Z, Baliga M*, et al.* In vitro and in vivo evidence suggesting a role for iron in cisplatin-induced nephrotoxicity. *Kidney Int* 1998; **53:** 394-401.

215. Martin-Sanchez D, Gallegos-Villalobos A, Fontecha-Barriuso M*, et al.* Deferasirox-induced iron depletion promotes BclxL downregulation and death of proximal tubular cells. *Sci Rep* 2017; **7:** 41510.

216. Brunmair B, Lest A, Staniek K*, et al.* Fenofibrate impairs rat mitochondrial function by inhibition of respiratory complex I. *J Pharmacol Exp Ther* 2004; **311:** 109-114.

217. Brunmair B, Staniek K, Gras F*, et al.* Thiazolidinediones, like metformin, inhibit respiratory complex I: a common mechanism contributing to their antidiabetic actions? *Diabetes* 2004; **53:** 1052-1059.

218. Nulton-Persson AC, Szweda LI, Sadek HA. Inhibition of cardiac mitochondrial respiration by salicylic acid and acetylsalicylate. *J Cardiovasc Pharmacol* 2004; **44:** 591-595.

219. Krause MM, Brand MD, Krauss S*, et al.* Nonsteroidal antiinflammatory drugs and a selective cyclooxygenase 2 inhibitor uncouple mitochondria in intact cells. *Arthritis Rheum* 2003; **48:** 1438-1444.

220. Thomas C, Mackey MM, Diaz AA*, et al.* Hydroxyl radical is produced via the Fenton reaction in submitochondrial particles under oxidative stress: implications for diseases associated with iron accumulation. *Redox Rep* 2009; **14:** 102-108.

221. Hinson JA, Reid AB, McCullough SS*, et al.* Acetaminophen-induced hepatotoxicity: role of metabolic activation, reactive oxygen/nitrogen species, and mitochondrial permeability transition. *Drug Metab Rev* 2004; **36:** 805-822.

222. Wallace KB. Doxorubicin-induced cardiac mitochondrionopathy. *Pharmacol Toxicol* 2003; **93:** 105-115.

223. Zhao P, Slattery JT. Effects of ethanol dose and ethanol withdrawal on rat liver mitochondrial glutathione: implication of potentiated acetaminophen toxicity in alcoholics. *Drug Metab Dispos* 2002; **30:** 1413-1417.

224. Ott M, Gogvadze V, Orrenius S*, et al.* Mitochondria, oxidative stress and cell death. *Apoptosis* 2007; **12:** 913-922.

225. Wang W, Fang H, Groom L*, et al.* Superoxide flashes in single mitochondria. *Cell* 2008; **134:** 279-290.

226. Schlame M, Ren M. The role of cardiolipin in the structural organization of mitochondrial membranes. *Biochim Biophys Acta* 2009; **1788:** 2080-2083.

227. Vladimirov YA, Proskurnina EV, Izmailov DY*, et al.* Mechanism of activation of cytochrome C peroxidase activity by cardiolipin. *Biochemistry (Mosc)* 2006; **71:** 989-997.

228. Belikova NA, Vladimirov YA, Osipov AN*, et al.* Peroxidase activity and structural transitions of cytochrome c bound to cardiolipin-containing membranes. *Biochemistry* 2006; **45:** 4998-5009.

229. Rao VK, Carlson EA, Yan SS. Mitochondrial permeability transition pore is a potential drug target for neurodegeneration. *Biochim Biophys Acta* 2014; **1842:** 1267-1272.

230. Tabara LC, Poveda J, Martin-Cleary C*, et al.* Mitochondria-targeted therapies for acute kidney injury. *Expert Rev Mol Med* 2014; **16:** e13.

231. Feldkamp T, Park JS, Pasupulati R*, et al.* Regulation of the mitochondrial permeability transition in kidney proximal tubules and its alteration during hypoxia-reoxygenation. *Am J Physiol Renal Physiol* 2009; **297:** F1632-1646.

232. Siemen D, Ziemer M. What is the nature of the mitochondrial permeability transition pore and what is it not? *IUBMB Life* 2013; **65:** 255-262.

233. Juhaszova M, Wang S, Zorov DB*, et al.* The identity and regulation of the mitochondrial permeability transition pore: where the known meets the unknown. *Ann N Y Acad Sci* 2008; **1123:** 197-212.

234. Cung TT, Morel O, Cayla G*, et al.* Cyclosporine before PCI in Patients with Acute Myocardial Infarction. *N Engl J Med* 2015; **373:** 1021-1031.

235. Tedeschi H, Harris DL. Some observations on the photometric estimation of mitochondrial volume. *Biochim Biophys Acta* 1958; **28:** 392-402.

236. Kaasik A, Safiulina D, Zharkovsky A*, et al.* Regulation of mitochondrial matrix volume. *Am J Physiol Cell Physiol* 2007; **292:** C157-163.

237. Haworth RA, Hunter DR. The Ca2+-induced membrane transition in mitochondria. II. Nature of the Ca2+ trigger site. *Arch Biochem Biophys* 1979; **195:** 460-467.

238. Chakraborty H, Chakraborty PK, Raha S*, et al.* Interaction of piroxicam with mitochondrial membrane and cytochrome c. *Biochim Biophys Acta* 2007; **1768:** 1138-1146.

239. Russo LM, Sandoval RM, McKee M*, et al.* The normal kidney filters nephrotic levels of albumin retrieved by proximal tubule cells: retrieval is disrupted in nephrotic states. *Kidney Int* 2007; **71:** 504-513.

240. Sandoval RM, Molitoris BA. Quantifying glomerular permeability of fluorescent macromolecules using 2-photon microscopy in Munich Wistar rats. *J Vis Exp* 2013.

241. Tenten V, Menzel S, Kunter U*, et al.* Albumin is recycled from the primary urine by tubular transcytosis. *J Am Soc Nephrol* 2013; **24:** 1966-1980.

242. Bruin GJ, Faller T, Wiegand H*, et al.* Pharmacokinetics, distribution, metabolism, and excretion of deferasirox and its iron complex in rats. *Drug Metab Dispos* 2008; **36:** 2523-2538.

243. Kozjak-Pavlovic V. The MICOS complex of human mitochondria. *Cell Tissue Res* 2017; **367:** 83-93.

244. Lee JW, Kang HJ, Choi JY*, et al.* Pharmacogenetic study of deferasirox, an iron chelating agent. *PLoS One* 2013; **8:** e64114.

245. Allon M, Lawson L, Eckman JR*, et al.* Effects of nonsteroidal antiinflammatory drugs on renal function in sickle cell anemia. *Kidney Int* 1988; **34:** 500-506.

246. N. Gattermann NZ, E. Angelucci, G. Drelichman, J. Siegel, E. Glimm and D. Alberti. Impact on Iron Removal of Dose Reduction for Non-Progressive Serum Creatinine Increases during Treatment with the Once-Daily, Oral Iron Chelator Deferasirox (Exjade®, ICL670). *Blood* 2006; **108:** 3824.

247. Dare AJ, Bolton EA, Pettigrew GJ*, et al.* Protection against renal ischemia-reperfusion injury in vivo by the mitochondria targeted antioxidant MitoQ. *Redox Biol* 2015; **5:** 163-168.